

# An Oscillating Ion Trap

A thesis submitted for the degree of  
*Diplom Physiker (Master of Science)*

Tim Lindner

AG Schmidt-Kaler

Johannes Gutenberg-Universität Mainz



2011

1. Reviewer: Prof. Dr. Ferdinand Schmidt-Kaler

2. Reviewer: Prof. Dr. Jochen Walz

Für Elisa



## Abstract

Coupled systems of macroscopic and atomic objects are interesting subjects of study. Understanding such coupled systems allows one to illuminate the boundary between the macroscopic, classical, world and the microscopic, quantum mechanical, world. The demonstration of the quantum nature of macroscopic mechanical objects has the potential not only to reach a new level of measuring precision, but also for a greater understanding of physics.

The experiment described in this thesis aims to establish the basis for coupling an ion and a micro oscillator. Based on the idea of Frank Ziesel to combine an ion trap with a membrane, we set up an oscillating ion trap. This thesis describes the development of the so called membrane trap, starting from the simulation of the trap to a complete experimental setup. The focus of this work lies on the characterization of the system, consisting of an ion and a membrane, but we will also discuss possible future measurements. The essential feature of the oscillating ion trap is the implementation of a Paul trap in a specially prepared membrane, which provides the required geometrical structure for a micro ion trap. For finding the proper conditions for a stable ion trap, we used numerical simulations to analyze the potentials and trajectories. Based on these simulations, the design of the trap holes was created, as well as the configuration of the electrical components. Following a design by Frank Ziesel, the ultra-high vacuum setup for the membrane trap was assembled. Furthermore, the imaging optics were set up and the focusing of the laser beams through the trap holes were optimized. For the analysis of the mechanical properties of the membrane, a specially designed Michelson interferometer was developed and fabricated. The theoretically expected resonance frequencies and quality factors of the

membrane were then compared to the obtained results using the interferometer. Additionally, a preliminary theoretical analysis of future measurements was performed and their experimental implementation was prepared.

The work introduced in this thesis enables a variety of directions for future research. One example is a cryogenic setup for the oscillating ion trap, which could allow the cooling of the membrane to the ground state, making it possible to reach the strong coupling regime of an ion and the membrane.

## Zusammenfassung

Die Erforschung der Kopplung von makroskopischen und atomaren Objekten ist Gegenstand aktueller Forschungen und von großem Interesse, denn solche Systeme ermöglichen eine Untersuchung der Verbindung zwischen der makroskopischen, klassischen Welt und der mikroskopischen, quantenmechanischen Welt. Solche makroskopischen mechanischen Objekte, die sich dabei trotzdem nach Gesetzen der Quantenwelt verhalten, könnten sowohl zum Erreichen neuer Messgenauigkeiten führen, als auch unser Verständnis der Physik erweitern.

Das in dieser Diplomarbeit vorgestellte Experiment soll den Grundstein legen für die Kopplung von einem Ion und einem Mikro-Oszillator. Basierend auf der Idee Frank Ziesels, eine Ionenfalle mit einer Membran zu verbinden, haben wir eine schwingende Ionenfalle aufgebaut. Diese Diplomarbeit beschreibt die Entwicklung dieser Membranfalle, beginnend bei Simulationen der Falle, bis hin zum kompletten Experiment. Den Schwerpunkt der Arbeit stellt die grundlegende Charakterisierung des Systems aus Ion und Membranfalle dar, doch werden auch zukünftige Möglichkeiten diskutiert, die das Experiment bietet. Die schwingende Ionenfalle besteht aus einer speziell entworfenen Membran, die die geometrische Struktur einer Mikro-Ionenfalle mit einem mechanischen Oszillator verbindet. Um die nötigen Voraussetzungen für eine funktionierende Ionenfalle zu schaffen, wurde diese zunächst numerisch simuliert und die Potentiale sowie Trajektorien analysiert. Auf diesen Simulationen basierend, wurde das Design der Fallenlöcher erstellt und die elektrischen Bauteile der Membranfalle angepasst. Ein Ultrahoch-Vakuum-Aufbau wurde nach einem Design von Frank Ziesel konstruiert und die Membranfalle darin integriert. Desweiteren wurde die Abbildungsoptik für die EMCCD-Kamera aufgebaut und die Fokussierung der Laser durch die

Fallenlöcher optimiert. Um die mechanischen Eigenschaften der Membran zu untersuchen, wurde ein spezielles Michelson Interferometer entworfen. Damit wurden die Resonanzfrequenzen und Qualitätsfaktoren der Membran bestimmt und diese anschließend mit den theoretischen Werten verglichen. Zusätzlich wurden vorbereitende theoretische Analysen für zukünftige Messungen durchgeführt und deren Umsetzung im Experiment geplant.

Für die Zukunft der Membranfalle gibt es viele Möglichkeiten. So wäre es zum Beispiel eine Möglichkeit einen kryogenen Aufbau zu entwerfen, der das Kühlen der Membran in den Grundzustand ermöglicht und eine starke Kopplung zwischen Ion und Membran realisierbar macht.

## **Danksagung**

### Acknowledgements

Diese Arbeit ist nicht in einer Einzelleistung entstanden, sondern wurde erst durch die Unterstützung meiner Arbeitsgruppe möglich. Hier möchte ich meinen Dank an alle diejenigen aussprechen, die zum Gelingen dieser Arbeit beigetragen haben. An erster Stelle danke ich Ferdinand Schmidt-Kaler, der mir die Durchführung dieser Diplomarbeit ermöglicht hat und immer mit gutem Rat zur Seite stand. Insbesondere möchte ich meinen Dank für die schnellen und hilfreichen Korrekturen dieser Arbeit aussprechen.

Bedanken möchte ich mich bei dem Team von Herrn Doktor Jürgen Weiß vom Max-Planck-Institut für Festkörperforschung in Stuttgart für die Bearbeitung der Membranen.

Besonderer Dank gilt meinem Betreuer Frank Ziesel, der nicht nur einen bedeutenden Beitrag zu dieser Arbeit geleistet hat, mir stets bei jeder Frage helfend zur Seite stand und für mich das ein oder andere Wochenende geopfert hat, sondern auch in meiner Zeit mit Krücken nicht davor zurückgeschreckt ist als Doktorand das Tablett eines Diplomanden zu tragen. Ich hätte mir keinen besseren Betreuer vorstellen können.

Meinen Bürokollegen möchte ich nicht nur für die verständnisfördernden Diskussionen danken, sondern auch für die lustige und angenehme Zeit abseits der Physik.

Außerdem danke ich natürlich der gesamten Arbeitsgruppe. Die freundliche Atmosphäre und große Hilfsbereitschaft innerhalb der Gruppe hat diese Arbeit sehr erleichtert und ich bereue es, nicht öfter bei dem wöchentlichen Sportprogramm teilnehmen gekonnt zu haben.

Ganz besonders danke ich meiner Familie, die mich besonders in den schwierigeren Zeit stets unterstützt hat und mir mein Studium überhaupt erst ermöglicht hat.

Elisa, dir danke ich für das viele Verständnis und die Unterstützung besonders während den stressigen Phasen, du hast es immer geschafft selbst diese zu versüßen.



# Contents

<b>1</b>	<b>Introduction</b>	<b>1</b>
<b>2</b>	<b>Theoretical Foundation</b>	<b>5</b>
2.1	The ion - a two level system approach . . . . .	7
2.1.1	State-sensitive detection of the ion via fluorescence read out . . . . .	9
2.2	The ion oscillating in a harmonic potential . . . . .	11
2.2.1	Trapping ions in a ring Paul trap . . . . .	11
2.2.2	The Hamiltonian of an ion in a harmonic potential . . . . .	16
2.2.3	Doppler cooling of an ion in a harmonic potential . . . . .	17
2.3	Light-Ion interactions . . . . .	19
2.3.1	Coherent dynamics: Rabi oscillations . . . . .	21
2.3.2	Lamb-Dicke regime . . . . .	22
2.3.3	Spectroscopy of the motional sidebands . . . . .	22
2.4	Vibrations of a membrane . . . . .	24
2.4.1	Vibrations of a classical membrane . . . . .	24
2.4.2	The membrane as quantum mechanical oscillator . . . . .	28
2.4.3	Measuring vibrations with a Michelson interferometer . . . . .	29
2.5	Interactions in the combined system of ion and membrane . . . . .	31
2.6	Interactions with the environment . . . . .	34
2.6.1	Interactions of the ion with the environment . . . . .	34
2.6.2	Interactions of the membrane with the environment . . . . .	36
<b>3</b>	<b>Experimental Setup</b>	<b>37</b>
3.1	The membrane trap . . . . .	38
3.1.1	Preparation of a membrane as ion trap . . . . .	38
3.1.2	Placing the ion trap in an ultra-high vacuum system . . . . .	39
3.1.3	Setup of the ultra-high vacuum system . . . . .	41
3.1.4	The laser system of the membrane ion trap . . . . .	42
3.1.5	Apparatus for the detection of an ion . . . . .	43
3.1.6	The complete setup of the oscillating ion trap . . . . .	44
3.2	The interferometer for vibration measurement . . . . .	46
3.2.1	The setup of the interferometer . . . . .	46
3.2.2	Implementing a stabilization circuit . . . . .	48

## CONTENTS

---

<b>4</b>	<b>Numerical Simulations and Experimental Results</b>	<b>51</b>
4.1	Simulating the membrane ion trap . . . . .	52
4.1.1	Simulations of the ponderomotive potential . . . . .	53
4.1.2	Simulations of the trajectory of the ion . . . . .	56
4.2	Preliminary measurements to test the interferometer . . . . .	64
4.3	Measurements of vibrational modes of the membrane . . . . .	65
4.3.1	First attempts with a damaged membrane . . . . .	65
4.3.2	The hypertensive version of the final membrane . . . . .	67
4.3.3	The final version of the membrane . . . . .	69
4.4	Reference measurements in a cryogenic ion trap . . . . .	74
4.5	Current state of the membrane ion trap and future measurements . . . . .	76
4.5.1	Beyond the Lamb Dicke regime . . . . .	79
4.5.2	Alternative detection methods . . . . .	82
<b>5</b>	<b>Discussion</b>	<b>85</b>
<b>A</b>	<b>Appendix</b>	<b>87</b>
A.1	The Stabilization circuit . . . . .	87
A.2	Characterization of the stabilization circuit . . . . .	89
A.3	Characterization of the dynamic behavior of an amplifier . . . . .	90
	<b>References</b>	<b>91</b>

# List of Figures

2.1	The ion - a two level system . . . . .	7
2.2	Energy levels of Calcium . . . . .	8
2.3	Zeeman splitting of the ground state . . . . .	9
2.4	A typical histogram . . . . .	10
2.5	The ion trapped in a harmonic potential . . . . .	11
2.6	Drawing of a ring Paul trap . . . . .	12
2.7	Stability diagrams of the Mathieu equation (2.15) . . . . .	14
2.8	Lowest stability zone of a ring Paul trap . . . . .	15
2.9	The ion interacting with laser beams . . . . .	19
2.10	Zeeman substructure of the spectroscopy transition . . . . .	23
2.11	Vibrations of a membrane . . . . .	24
2.12	Scheme for the stretched plane membrane . . . . .	25
2.13	The first three normal modes of a rectangular membrane . . . . .	29
2.14	Scheme of a Michelson interferometer . . . . .	30
2.15	Coupling of an ion to a membrane . . . . .	31
2.16	Interactions with the environment . . . . .	34
3.1	Schematic arrangement of the holes on the membrane . . . . .	38
3.2	A picture of the final membrane . . . . .	39
3.3	Magnification of the holes in the membrane . . . . .	40
3.4	Drawing of the mount . . . . .	40
3.5	Top view of the chamber . . . . .	41
3.6	Schematic drawing of the laser setup . . . . .	43
3.7	Schematics of the detection apparatus . . . . .	44
3.8	Setup of the membrane trap including the interferometer . . . . .	45
3.9	Schematic drawing of the Michelson interferometer . . . . .	46
3.10	The interferometer design . . . . .	47
3.11	Schematic drawing of the stabilization circuit . . . . .	48
4.1	Simulation model for the membrane trap . . . . .	52
4.2	Simulated potentials of the membrane trap . . . . .	53
4.3	Decoupling of the three modes of the ion . . . . .	54
4.4	Simulated trajectories of the ion . . . . .	56

## LIST OF FIGURES

---

4.5	Stability diagrams of the membrane trap . . . . .	57
4.6	Trajectories for each dimension plotted against time . . . . .	58
4.7	Frequency analysis of the trajectories . . . . .	59
4.8	Stability diagrams of the vibrating membrane trap . . . . .	61
4.9	Trajectory in $z$ -direction for a vibrating membrane . . . . .	62
4.10	Frequency analysis of the trajectory of the ion in a vibrating membrane	63
4.11	Measurement of the amplitude of a vibrating mirror . . . . .	64
4.12	Magnification of the damaged membrane . . . . .	65
4.13	Resonance frequency of the damaged membrane . . . . .	66
4.14	Ring-down measurement of the damaged membrane . . . . .	67
4.15	Resonance frequency spectrum of the hypertensive membrane . . . . .	68
4.16	Resonance spectra from two different positions on the membrane . . . . .	69
4.17	Resonance spectrum of the final version of the membrane . . . . .	70
4.18	Resonance spectra of the final version and the hypertensive version of the membrane . . . . .	70
4.19	A ring-down measurement at $f_{res} = 21.888$ kHz . . . . .	72
4.20	Sideband spectrum of the cryogenic microtrap . . . . .	74
4.21	Rabi oscillations in the cryogenic microtrap . . . . .	75
4.22	Fluorescence of the neutral atom beam detected via an infrared camera .	76
4.23	Fluorescence of the neutral atom beam detected at the trapping region via the EMCCD camera . . . . .	77
4.24	Matrix elements for different Lamb Dicke parameters $\eta$ . . . . .	80
4.25	Simulation of sideband spectra . . . . .	81
4.26	Simulations of Rabi oscillations for a thermal probability distribution . .	82
4.27	Background free detection schemes . . . . .	83
A.1	The stabilization circuit diagram . . . . .	88
A.2	Photo diode signal without stabilization . . . . .	89
A.3	Photo diode signal with stabilization . . . . .	89
A.4	Amplification of the piezo amplifier . . . . .	90

# List of Tables

4.1	Trap parameters . . . . .	55
4.2	Comparison of trap frequencies . . . . .	60
4.3	Quality factors of the final version of the membrane . . . . .	71
4.4	Theoretical vibration frequencies . . . . .	73
4.5	Lamb Dicke parameters for the trap and membrane frequencies . . . . .	78



# 1

## Introduction

At the beginning of the 20th century the formulation of the quantum theory provided the foundation to understand physics on a novel microscopic level – a quantum level. Since then, many theories were confirmed in experiments and quantum physics affected almost every field of science. With the development of novel and better techniques to observe and manipulate particles at atomic and sub-atomic scales, the exploration of the quantum world continues.

As nowadays the macroscopic world is well understood and evidence from an increasing number of experiments supports the quantum theory and hence our understanding of the microscopic world, the next step is to investigate the connection between both worlds. Therefore, it is necessary to find a way to couple macroscopic and microscopic objects and study their interactions. The goal is to illuminate the boundary between our macroscopic world, governed by classical physics, and the microscopic realm, governed by quantum mechanics. The demonstration of the quantum nature of macroscopic mechanical objects has the potential to open up new perspectives on the research of the limits of quantum-based measurements. This may lead to the development of novel techniques techniques to control quantum states. The investigation of macroscopic quantum coherence might influence the quantum world in every field, e.g., quantum simulation, quantum information protocols.

For more than a decade, the coupling of microscopic and macroscopic objects has been a regularly discussed theoretical idea [Law 1994, Law 1995, Bose 1999, Meiser 2006, Genes 2008, Ian 2008]. But only recently, it has become possible to observe it in experimental setups. A variety of different approaches has been considered in this con-

## 1. INTRODUCTION

---

text, many of them utilizing the well-established properties of mechanical oscillators. The advantages of such systems are not only the variety of existing theoretical coupling schemes, which make it possible to examine quantum behavior in ordinary bits of matter, but also the possibility to establish the oscillators as probes of quantum and mesoscopic forces.

One approach that has contributed much activity lately is the so-called optomechanics approach that has resulted in significant research efforts lately [Kippenberg 2008, Anetsberger 2009, Marquardt 2009, Regal 2011]. Its main idea is to use a micro- or nanomechanical oscillator as one of the two mirrors of a cavity. Many interesting discoveries have already been made, including the cooling of a mechanical oscillator to or near to its ground state. [Teufel 2011a, Rivière 2011]

Based on the promising discoveries in the field of optomechanics, the coupling of atoms to mechanical oscillators has made great progress. By adding a Bose-Einstein-condensate to the system of cavity and oscillator, the vast experience with ultra-cold atoms in cavities and optical lattices could be combined with mesoscopic objects, e.g., cantilevers and membranes. Recent experiments have already provided encouraging first results and should be investigated further. [Treutlein 2007, Hammerer 2009, Hammerer 2010, Hunger 2010, Wallquist 2010, Hunger 2011].

Another method is the utilization of superconducting circuits, which can be described as electromagnetic cavities, with high-quality-factor mechanical oscillators [Craighead 2000]. Recently it was accomplished to reach the strong-coupling regime with such a setup. Following the definition known from cavity quantum electro dynamics, in the strong-coupling regime the interaction between two systems is faster than the dissipation of energy from either system [Teufel 2011b].

In this thesis we present a system consisting of a macroscopic mechanical oscillator, i.e., a Silicon membrane, and an ion. Ions provide an ideal system to study quantum mechanics in an isolated environment, thereby reducing undesirable interactions with the outside world. An elaborate toolbox to prepare, control and manipulate ions exists. Our experience with microtraps permits preparation and detection of desired states, such as the ground state, and enables the creation of non-classical states, e.g., superpositions and entangled states [Leibfried 2003, Häffner 2008, Poschinger 2010b, Poschinger 2010a]. In

---

a recent experiment the coupling of an ion to the smallest know oscillator, a second ion, was already achieved [Brown 2010].

The membrane provides the required geometrical structures for a micro ion trap and the well characterized properties of a mechanical oscillator. Our first attempt is to use the ion as a high-sensitive probe to analyze the vibrations of the membrane and examine the interaction between membrane and ion. Additionally, the presented setup allows the investigation of non-classical states. Although a cooling of the membrane via interaction with the ion is not possible in this setup, the thermal state of the membrane already provides many interesting possibilities to explore the connection of classical and quantum mechanical properties.

In a future setup the investigation of a ground state cooled membrane opens new perspectives for further coupling schemes. In a cryogenic setup the membrane could be cooled to a quantized state and the interaction with an ion in the ground state could be observed, for example the coherent exchange of energy between the two systems.

### **Organization of the chapters:**

The **second chapter** provides the theoretical foundation. The Hamilton operator of the system of the membrane and the ion is derived and we analyze the different terms in detail. In this chapter, we study the required mechanisms to trap and control the ion via electrical potentials and electromagnetic fields, respectively. We analyze the possible coupling of a membrane and an ion, and their respective dissipation channels. Furthermore, we discuss the measurement of the vibrational modes of the membrane using an interferometer.

In the **third chapter** the experimental setup is described. The first part of this chapter describes the setup of the membrane ion trap, including the membrane itself, its placement inside a vacuum chamber and the necessary tools, such as the laser system and the imaging optics. The second part covers the interferometer, which was especially designed for this setup, and the stabilization circuit used to reduce noise signals.

The **fourth chapter** covers the obtained results. First, we discuss the simulations of the potentials and the resulting trajectories, analyze different trap sizes, in our case different

## 1. INTRODUCTION

---

hole sizes, and examine a vibrating trap situation. Then we describe the characterization of the stabilization circuit and the results of the measurements of the vibrational modes of different membranes, as well as the measurements of the quality-factor. After that we show some example sideband spectroscopy measurements obtained in a different trap to compare them to the expected results in the membrane trap. Finally we present the first successful steps towards trapping an ion in the membrane trap and give an outlook on future measurements.

The **fifth chapter** summarizes the current state of the membrane trap and discusses a future approach to achieve a membrane-ion coupling at cryogenic temperatures, as well as a variety of further research possibilities.

# 2

## Theoretical Foundation

### Contents

---

<b>2.1</b>	<b>The ion - a two level system approach . . . . .</b>	<b>7</b>
2.1.1	State-sensitive detection of the ion via fluorescence read out . . . . .	9
<b>2.2</b>	<b>The ion oscillating in a harmonic potential . . . . .</b>	<b>11</b>
2.2.1	Trapping ions in a ring Paul trap . . . . .	11
2.2.2	The Hamiltonian of an ion in a harmonic potential . . . . .	16
2.2.3	Doppler cooling of an ion in a harmonic potential . . . . .	17
<b>2.3</b>	<b>Light-Ion interactions . . . . .</b>	<b>19</b>
2.3.1	Coherent dynamics: Rabi oscillations . . . . .	21
2.3.2	Lamb-Dicke regime . . . . .	22
2.3.3	Spectroscopy of the motional sidebands . . . . .	22
<b>2.4</b>	<b>Vibrations of a membrane . . . . .</b>	<b>24</b>
2.4.1	Vibrations of a classical membrane . . . . .	24
2.4.2	The membrane as quantum mechanical oscillator . . . . .	28
2.4.3	Measuring vibrations with a Michelson interferometer . . . . .	29
<b>2.5</b>	<b>Interactions in the combined system of ion and membrane . . . . .</b>	<b>31</b>
<b>2.6</b>	<b>Interactions with the environment . . . . .</b>	<b>34</b>
2.6.1	Interactions of the ion with the environment . . . . .	34
2.6.2	Interactions of the membrane with the environment . . . . .	36

---

In this thesis the coupling of an ion to a mechanical oscillator, in our case a membrane, is discussed. We start by defining the Hamilton operator for the system of membrane

## 2. THEORETICAL FOUNDATION

---

and ion including all interactions and then go on by taking a closer look at the separate terms.

The system consists on the one hand of the ion, which interacts with the trapping potential, the laser beams, and the environment and on the other hand of the membrane, which is characterized by its eigenfrequencies and the corresponding quality factor and is influenced by the environment, as well. At last we have to consider the interactions between membrane and ion.

The Hamilton operator of the whole system can be written as

$$\begin{aligned} H_{system} = & H_{ion} + H_{pot} + H_{laser-ion} \\ & + H_{mem} + H_{mem-ion} \\ & + H_{ion-world} + H_{mem-world} \end{aligned} \quad (2.1)$$

where  $H_{ion}$  describes the ions internal structure using a two level approximation and its behavior in the harmonic trap potential is described by  $H_{pot}$ . The interaction of the ion with the applied laser beams is formulated by  $H_{laser-ion}$ .  $H_{mem}$  defines the membrane vibrations in a quantum mechanical approach and the interaction between the ion and the membrane is described by  $H_{mem-ion}$ . The last two terms  $H_{ion-world}$  and  $H_{mem-world}$  describe the interaction of the ion and the membrane with the environment, respectively. These terms lead to dissipation.

In the following sections, we analyze the different Hamilton operators in detail.

## 2.1 The ion - a two level system approach

---

At first, we take a closer look at the ion. In the experiments presented in this thesis, we work with Calcium ions ( $^{40}\text{Ca}^+$ ). For the membrane trap, there are three important properties to account for choosing the right element. First of all, we need to ionize an atom beam. Secondly, the energy level structure needs to be accessible for existing laser systems and thirdly, a fast decaying state for Doppler cooling and internal state detection, as well as a metastable state for spectroscopy are required. Calcium has proven to be a good choice for experiments in ion traps and fulfills these requirements. Isotope selective photo ionization of Calcium is possible, for all relevant transitions there are affordable lasers available and we will see that the the internal structure of  $^{40}\text{Ca}^+$  provides the necessary states.

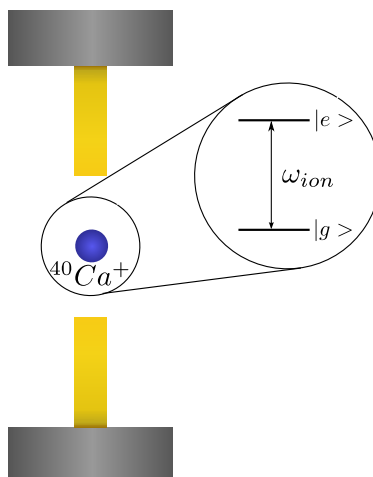


**Figure 2.1: The ion - a two level system** - The ion is well approximated by a two level system approach, although its actual internal structure is more complicated. The overview pictures at the beginning of each section show a cut through the membrane hole, which represents the geometry of a ring Paul trap.

Figure 2.2 shows the internal structure of the ionized  $^{40}\text{Ca}^+$ , produced via photo ionization<sup>1</sup>. The relevant energy levels, transitions, and lifetimes are displayed. There are the fast decaying P-levels and the metastable D-Levels. The  $4^2P_{1/2}$  state is used for

---

<sup>1</sup>Photo ionization is described in detail elsewhere: [Gulde 2001].

## 2. THEORETICAL FOUNDATION

Doppler cooling and internal state detection, the  $3^2D_{5/2}$  level is used for spectroscopy.

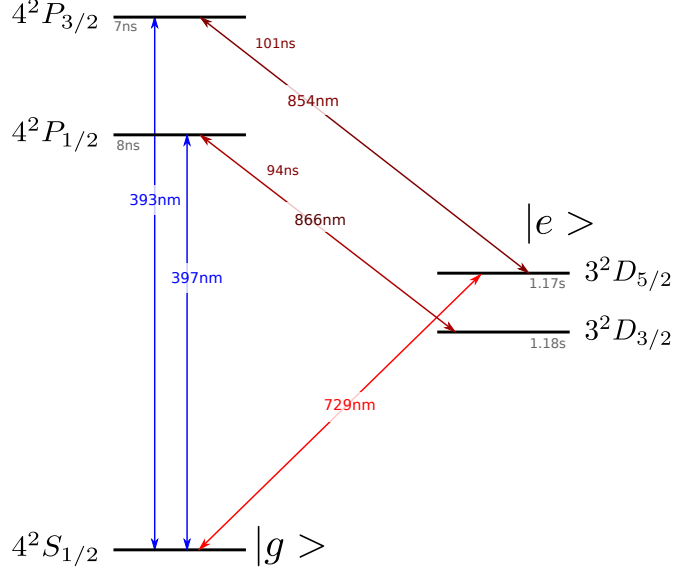


**Figure 2.2: Energy levels of Calcium** - A scheme of the internal structure of a  $^{40}\text{Ca}^+$  ion. The fast decaying  $4^2S_{1/2} - 4^2P_{1/2}$  transition is used for detection via fluorescence read out and Doppler cooling. The transition  $4^2S_{1/2} - 3^2D_{5/2}$  (represented by  $|g\rangle$  and  $|e\rangle$ , respectively) is important for sideband spectroscopy. All transitions are accessible with common laser systems.

Despite the complicated internal structure of the ion, a good approximation is the approach to describe the ion as a two level system. Therefore we start by choosing two arbitrary states  $|g\rangle$  and  $|e\rangle$  with respective energies  $E_g$  and  $E_e$ . In the case of the  $^{40}\text{Ca}^+$  ion,  $|g\rangle$  represents the  $4^2S_{1/2}$  state and  $|e\rangle$  the  $3^2D_{5/2}$  state. The Hamiltonian is then defined by:

$$H_{ion} = \frac{\hbar\omega_{ion}}{2} (|e\rangle\langle e| - |g\rangle\langle g|) \quad (2.2)$$

with

$$\omega_{ion} = (E_e - E_g) / \hbar \quad (2.3)$$

In the presence of an quantizing external magnetic field  $B$ , an energy splitting of the  $m_J$  sublevels occurs, the so called Zeeman splitting. This effect is described by the

following Hamilton operator

$$H_Z = \mu_B g_J \sum_{m_J} m_J B |Jm_J\rangle \langle Jm_J| \quad (2.4)$$

where  $\mu_B$  is the Bohr magneton and  $g_J$  are the Landé factors. In figure 2.3 an example for the  $S_{1/2}$  state is shown.

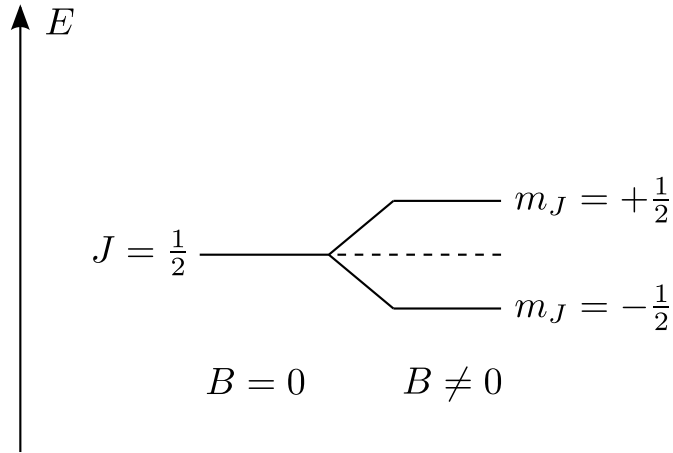


Figure 2.3: Zeeman splitting of the ground state - description

### 2.1.1 State-sensitive detection of the ion via fluorescence read out

The state-sensitive detection of the  $^{40}\text{Ca}^+$  ion is possible via fluorescence read out on the fast decaying  $4^2S_{1/2} - 4^2P_{1/2}$  transition. By applying laser beams at 854 nm and 866 nm we keep the ion from occupying the metastable  $3^2D_j$  states, hence it is only available for the fast decaying  $4^2S_{1/2} - 4^2P_{1/2}$  and  $4^2S_{1/2} - 4^2P_{3/2}$  transitions. If we drive the transition at 397 nm, we can detect the emission of fluorescence light via the EMCCD camera. Turning off the laser at 866 nm, we allow the ion to occupy the metastable  $3^2D_{5/2}$  state, making it unavailable for the fluorescence transition for the lifetime of the metastable state. Additionally, it is possible to drive the  $4^2S_{1/2} - 3^2D_{5/2}$  transition at 729 nm, in combination with the laser at 866 nm turned on or off, to directly control, if the ion is in a bright or dark state.

The discrimination of a bright and dark state of the ion is detected via the difference of the count rate for light at 397 nm. The short lifetime of the  $4^2P_{1/2}$  state ( $\tau = 8$  ns)

## 2. THEORETICAL FOUNDATION

---

implicates a high scattering rate of  $\Gamma \approx 2\pi \cdot 20$  MHz. When the ion is in a dark state the count rate is decreased, but remaining stray light from the laser at 397 nm is still detected. A threshold is defined to distinguish between the count rates for bright and dark state. The threshold is calculated from the mean value of the count rate of the bright ion  $\bar{b}$  and the dark ion  $\bar{d}$  for a constant period of time (typically 5 ms):

$$\sigma = \sqrt{\bar{b}\bar{d}} \quad (2.5)$$

Figure 2.4 shows an example for a typical histogram.

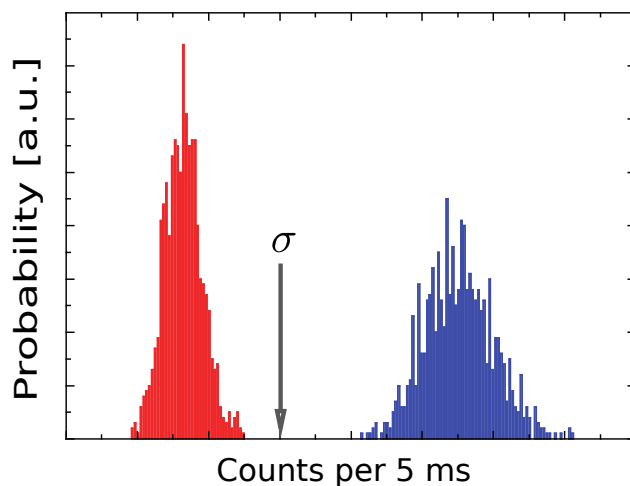


**Figure 2.4: A typical histogram** - The histogram for typical count rates shows the “dark counts” colored red, the “bright counts” colored blue, and the threshold  $\sigma$  is marked by the arrow.

## 2.2 The ion oscillating in a harmonic potential

In this section, the trapping of the ion in a harmonic potential is described. We start by discussing the trapping mechanism of a Paul trap, then we go on to describe the Hamiltonian for an ion oscillating in a harmonic potential and the influence on its behavior. At the end of this section, we will see that it is possible to cool the confined ion with only one laser beam and therefore discuss the Doppler cooling mechanism.

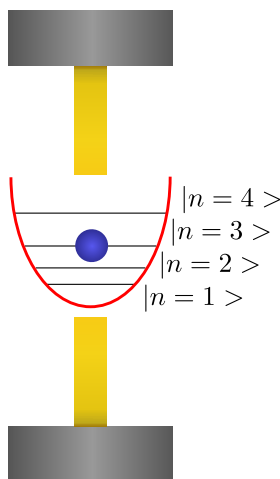


**Figure 2.5: The ion trapped in a harmonic potential** - In a harmonic potential the ion occupies quantized vibrational states.

### 2.2.1 Trapping ions in a ring Paul trap

In the last sixty years, a huge development at the field of single particle traps occurred. Charged particles can be trapped using the Coulomb force, e.g., in Penning [Dehmelt 1968] or Paul [Paul 1990] traps. The trapping of single particles is the first step towards understanding and researching quantum mechanical effects.

In 1953, Wolfgang Paul discovered that ions can be mass-selected using radio-frequency fields [Paul 1953]. Based on Paul's research, Dehmelt realized in 1967 that this mechanism could be utilized to trap single charged particles [Dehmelt 1967]. In modern

## 2. THEORETICAL FOUNDATION

---

quantum information experiments, this trapping mechanism proved itself as a fine instrument, because of the good isolation from the environment, if put into an ultra high vacuum, and the great accessibility, which is necessary for manipulation via laser beams.

There are different designs of Paul traps, which utilize the same trapping mechanism but have different advantages depending on their geometrical structure, e.g., surface traps, linear traps, ring traps. In this thesis we use a ring Paul trap since its necessary geometrical structure agrees well with the membrane geometry. In figure 2.6 a schematic drawing of a ring Paul trap is shown.

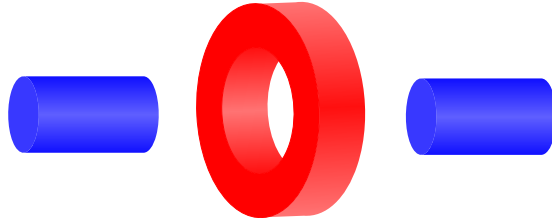


**Figure 2.6: Drawing of a ring Paul trap** - The r.f. electrode is colored red and the dc electrodes are colored blue.

The main concept of trapping charged particles in the center of a Paul trap is to use an alternating electrical field which creates a ponderomotive potential. It is necessary to use an alternating field. Since the Laplace equation  $\Delta\Phi = 0$  for the general electric quadrupole potential in the trapping region  $\Phi(x, y, z)$

$$\Phi(x, y, z) = \Phi_0 (\alpha_x x^2 + \alpha_y y^2 + \alpha_z z^2) \quad (2.6)$$

demands that the coefficients  $\alpha_i$  solve the following equation:

$$\sum \alpha_i = 0 \quad , \quad i = x, y, z \quad (2.7)$$

So while it is possible to have two positive coefficients creating a confining potential, one is always negative which creates a repulsive force pushing the ion out of the center. In the case of the static field, the ion would escape in the unstable direction.

The solution is to alternate the field<sup>1</sup> and take advantage of the inertia of mass. Chang-

---

<sup>1</sup>In the case of ion traps the order of the field is in the radio frequency range - that is why it is often called the r.f.-field.

## 2.2 The ion oscillating in a harmonic potential

---

ing between the trapping state in two dimensions and non-trapping state in one dimension, and vice versa, is accomplished by applying a time-dependent potential  $\Phi_0(t)$ :

$$\Phi_0(t) = U_{dc} + V_{rf} \cos(\Omega_{rf} t) \quad (2.8)$$

with  $U_{dc}$  being an applied dc voltage and  $V_{rf}$  being the amplitude of a r.f.-field with the driving frequency  $\Omega_{rf}$ .

The resulting potential is described by the following equation:

$$\begin{aligned} \Phi(x, y, z, t) = & U_{dc} \left( \alpha_x^{(dc)} (x - x')^2 + \alpha_y^{(dc)} (y - y')^2 + \alpha_z^{(dc)} (z - z')^2 \right) \\ & + V_{rf} \cos(\Omega_{rf} t) \left( \alpha_x^{(rf)} x^2 + \alpha_y^{(rf)} y^2 + \alpha_z^{(rf)} z^2 \right) \end{aligned} \quad (2.9)$$

A static potential created by the dc voltage  $U_{dc}$  is superimposed with a time-dependent potential induced by the r.f. voltage  $V_{rf} \cos(\Omega_{rf} t)$ . The fact that the two minima of the static and periodic potential may have slightly different positions is taken into account with the displacement vectors  $(x', y', z')$ .

Averaged over time, we would expect the time-dependent part of the potential to cancel itself out, resulting in no effective force. This turns out to be true for a homogeneous field, but in the case of the quadrupole field, which is an inhomogeneous field, a small average force is left which acts in the direction of the smallest field amplitude, in our case the center. Averaged over time we end up with a so called ponderomotive potential or pseudopotential  $\phi_{pond}$ :

$$\phi_{pond} = \frac{Z^2 e^2 |\vec{E}|^2}{4m\Omega_{rf}^2} \quad (2.10)$$

where  $Z$  is the atomic number,  $e$  is the electrical charge,  $\vec{E}$  for the electrical field,  $m$  for the mass and  $\Omega_{rf}$  for the angular oscillation frequency of the r.f.-field.

If an ion with mass  $m$  and charge  $Q = Z \cdot |e|$  enters the range of the electrical field, the following equations of motion describe the movement of the ion:

$$\ddot{u}_i + \frac{2Q}{m} \left( \alpha_i^{(dc)} U_{dc} + \alpha_i^{(rf)} V_{rf} \cos(\Omega_{rf} t) \right) u_i = 0 \quad (2.11)$$

## 2. THEORETICAL FOUNDATION

Substituting the following non-dimensional variables:

$$a_i = -\frac{8\alpha_i^{(dc)}QU_{dc}}{m\Omega_{rf}^2} \quad (2.12)$$

$$q_i = \frac{4\alpha_i^{(rf)}QV_{rf}}{m\Omega_{rf}^2} \quad (2.13)$$

$$\tau = \frac{\Omega_{rf}t}{2} \quad (2.14)$$

we obtain the form of the Mathieu differential equations:

$$\frac{d^2u_i}{d\tau^2} + (a_i - 2q_i \cos(2\tau))u_i = 0 \quad (2.15)$$

Depending on the values of  $a_i$  and  $q_i$  there are stable and instable solutions for a constant ratio of mass and charge  $m/e$ . For instable solutions the vibration of the particle increases exponentially until it leaves the trapping region. For stable solutions the particle stays in a small region around the trap center. Superimposing the stable solutions for all three dimensions, we get the stability diagram shown in figure 2.7.

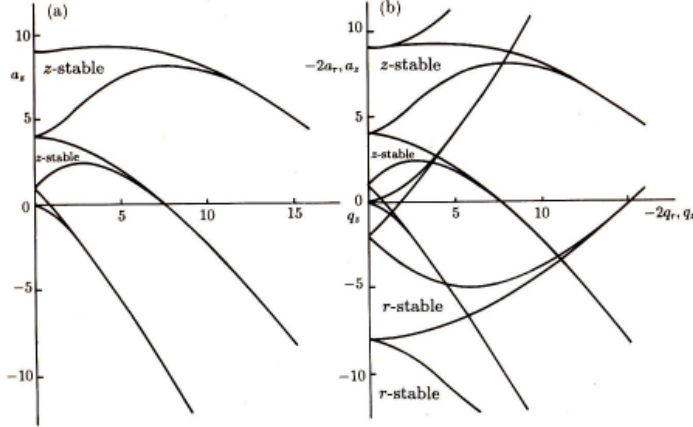


**Figure 2.7: Stability diagrams of the Mathieu equation (2.15)** - The stability parameters  $a$  and  $q$  are plotted against each other. The left plot shows the  $z$ -stability region, the right plot shows the superimposed  $z$ - and  $r$ -stability zones for a ring trap. [Ghosh 1995]

For the in  $z$ -direction rotationally invariant ring Paul trap, we obtain the following

## 2.2 The ion oscillating in a harmonic potential

---

relations of the stability parameters:

$$a_x = a_y = -a_z/2 \quad (2.16)$$

$$q_x = q_y = -q_z/2 \quad (2.17)$$

If the condition  $a_i \ll q_i \ll 1$  is fulfilled, stable solutions exist and can be approximated by

$$u(t) \approx A \cos(\omega_i t) \left[ 1 + \frac{q_i}{2} \cos(\Omega_r f t) \right] \quad (2.18)$$

where  $\omega_i$  is defined by

$$\omega_i = \beta_i \frac{\Omega_r f}{2} \quad \text{and} \quad \beta_i = \sqrt{a_i + \frac{q_i^2}{2}} \quad (2.19)$$

The lowest stability zone of a ring Paul trap is shown in figure 2.8.

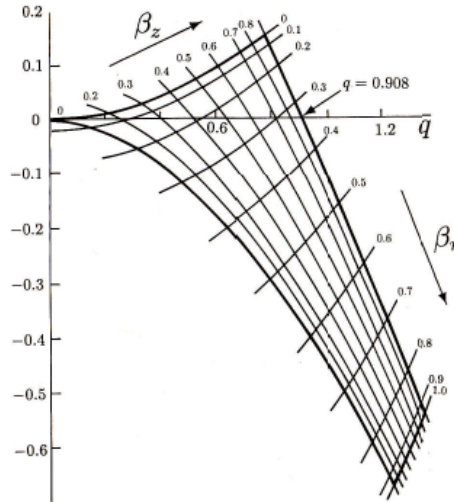


**Figure 2.8: Lowest stability zone of a ring Paul trap** - The stability parameters  $a$  versus  $q$  for the lowest stability zone in detail. Regions, where  $\beta < 1$ , are considered to be stable. [Ghosh 1995]

We see from equation 2.18 that the motion of the confined particle can be divided in a harmonic motion with frequency  $\omega_i$ , and a faster amplitude modulated motion induced by the frequency of the r.f.-field. The first one is called *secular motion* and the later

## 2. THEORETICAL FOUNDATION

---

is called *micromotion*. The secular motion is linked to the harmonic pseudo potential and if the particle is cooled to a limit where its kinetic energy is comparable to  $\hbar\omega$ , it is well described by a quantized harmonic oscillator with energy levels corresponding to the vibrational quanta. For a full description please refer to the literature, e.g., [Ghosh 1995, Wineland 1997].

The fast driven micromotion induces unwanted heating effects which can lead to unstable trapping condition, up to the loss of the ion and need to be minimized. In our case we can use the existing dc electrodes to move the ion in the node of the harmonic potential, thereby minimizing the micromotion.

In the common Paul trap designs, trap depths of a few hundred meV can be achieved, therefore it is possible to trap particles out of an thermal atomic beam<sup>1</sup>.

In section 4.1, the simulations of the potentials and trajectories for the membrane trap are based on these theoretical foundations.

### 2.2.2 The Hamiltonian of an ion in a harmonic potential

Now that we understand the trapping mechanism of a Paul trap, we take a closer look at the ion confined in such a harmonic potential. The Hamiltonian for the harmonic potential along one dimension takes the following form:

$$H_{pot} = \frac{p^2}{2m} + \frac{1}{2}m\omega_{pot}^2x^2 \quad (2.20)$$

Substituting the operators  $x$  and  $p$  with the creation and annihilation operators  $a^\dagger$  and  $a$ :

$$x = \sqrt{\frac{\hbar}{2m\omega_{pot}}} (a + a^\dagger), \quad p = i\sqrt{\frac{\hbar m\omega_{pot}}{2}} (a^\dagger - a) \quad (2.21)$$

we end up with the following expression for the Hamiltonian of the harmonic potential:

$$H_{pot} = \hbar\omega_{pot} \left( a^\dagger a + \frac{1}{2} \right) \quad (2.22)$$

---

<sup>1</sup>The most probable kinetic energy of a thermal atomic beam lies in the range of 0.05 eV.

## 2.2 The ion oscillating in a harmonic potential

---

This is the expression for the quantum mechanical harmonic oscillator with energy eigenstates  $|n\rangle$ , where these so-called Fock states represent phonons. All the relations known from the harmonic oscillator are also valid here, e.g.:

$$H_{pot} |n\rangle = \hbar\omega_{pot} \left( n + \frac{1}{2} \right) |n\rangle \quad (2.23)$$

### 2.2.3 Doppler cooling of an ion in a harmonic potential

The laser cooling of atoms, ions, or molecules with laser forces is one of the revolutionary methods developed in the 21<sup>st</sup> century. Many quantum mechanical experiments were only possible because of the development of this technique. Here we give just a brief introduction to Doppler cooling and discuss the special case of an ion in a harmonic potential. For further information about laser cooling please refer to the literature [[Hänsch 1975](#), [Wineland 1978](#), [Wineland 1979](#), [Vuletić 2000](#)].

#### Basic principles of Doppler cooling

Let us consider a particle moving in  $+x$ -direction with velocity  $v_x$  interacting with a counter-propagating laser beam with Intensity  $I$  and its frequency  $\nu_L$  tuned close to a transition of the particle:

$$\nu_L = \frac{c}{\lambda} = \nu_0 + \delta \quad \text{with} \quad \delta \ll \nu_0 \quad (2.24)$$

In the rest frame of the particle, the particle sees the Doppler-shifted frequency of the laser:

$$\nu'_L = \nu_L \left( 1 + \frac{v_x}{c} \right) \xrightarrow{v_x \ll c} \nu_0 + \delta + \frac{v_x}{c} \nu_0 \quad (2.25)$$

If we tune the laser to  $\delta = -\frac{v_x}{c} \nu_0$ , we find the laser in resonance with the particles moving in the  $+x$ -direction  $\nu'_L = \nu_0$ , but not with those moving in different directions. In this case, only the particles moving towards the laser beam absorbs a photon with frequency  $\nu'$  and then re-emits another photon with frequency  $\nu_0$  by spontaneous emission in a random direction. In a basic picture, the spontaneous emission in a random direction averages to zero, resulting in a net frictional force in the  $-x$ -direction, decelerating the particle, therefore cooling it.

## 2. THEORETICAL FOUNDATION

---

The frictional force  $F_x$  is given by the momentum change per absorption-emission cycle multiplied by the net rate of such cycles [Lett 1989]:

$$F_x = -\hbar k \times R(I, \Delta) \quad (2.26)$$

where  $\Delta = 2\pi\delta$  is the detuning in angular frequency units and  $k = 2\pi/\lambda$  is the wave vector. The net rate  $R(I, \Delta)$  is equal to the absorption rate minus the stimulated emission rate:

$$R(I, \Delta) = \frac{\gamma}{2} \left( \frac{I/I_s}{1 + I/I_s + [2(\Delta + kv_x)/\gamma]^2} \right) \quad (2.27)$$

where  $\gamma = 1/\tau$  is the natural linewidth and  $I_s$  is the saturation intensity of the transition.

In the case of the ion oscillating in a harmonic potential, we only need one laser beam in contrast to neutral atoms, where two laser beams are necessary for each dimension. Because of its charge, the ion is trapped in the potential and it is sufficient to cool it in only one direction, thereby cooling the other dimensions via energy exchange. In the case of the  $^{40}\text{Ca}^+$  ion the  $4^2S_{1/2} - 4^2P_{1/2}$  transition is used for Doppler cooling.

## 2.3 Light-Ion interactions

After understanding the trapping mechanism, the next step is to look at the possible ways to manipulate the ion using laser beams. The light-ion interaction can be approximated by a two-level system in the presence of a light wave, if the laser frequency is close to resonance of only one internal transition of the ion. We start by deriving the interaction Hamiltonian in a semiclassical approach and then we take a closer look at the dynamic behavior of the ion, i.e., the concept of Rabi oscillations.

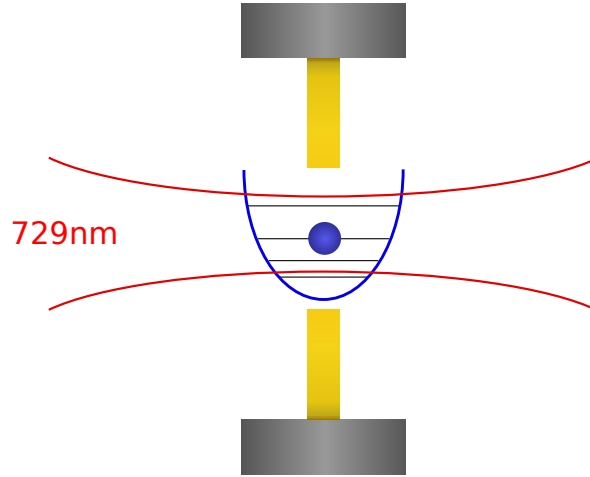


**Figure 2.9: The ion interacting with laser beams** - Trapped in a harmonic potential the ion is interacting with laser beams.

At first, we need to derive the formula for the light-ion interaction Hamilton operator. The light field can be described as an electrical field with frequency  $\omega_L$  propagating in direction  $x$ :

$$\vec{E}(x, t) = \vec{E}_0 \cdot \exp[i(\omega_L t - k_L x + \Phi)] + H.c. \quad (2.28)$$

where  $\vec{E}_0 = E_0 \vec{e}$  represents the amplitude and polarization of the laser beam. The laser-ion interaction Hamiltonian of equation (2.1) is derived via a semi-classical approach, which assumes that the interaction with the light field can be expressed as the induced

## 2. THEORETICAL FOUNDATION

---

energy shift of the atomic dipole  $\vec{d}_{ge} = e \langle g | x | e \rangle$  of the  $|g\rangle \leftrightarrow |e\rangle$  transition<sup>1</sup>:

$$H_{int} = \vec{d}_{ge} \vec{E}(x, t) \sigma_+ + H.c. \quad (2.29)$$

with the abbreviations  $\sigma_+$  and  $\sigma_-$  analogue to the notation of the creation and annihilation operators of the harmonic oscillator

$$\sigma_+ = |e\rangle \langle g| \quad \sigma_- = |g\rangle \langle e| \quad (2.30)$$

with

$$\sigma_+^\dagger = \sigma_-$$

Introduced as the coupling strength of the ion and the light field, the so-called resonant *Rabi frequency* is defined as

$$\Omega_0 := \frac{2\vec{E}_0 \cdot \vec{d}_{ge}}{\hbar} \quad (2.31)$$

Now the interaction Hamilton operator expands to

$$H_{int} = \frac{\hbar\Omega_0}{2} \left\{ e^{i(\omega_L t - k_L x + \Phi)} + e^{-i(\omega_L t - k_L x + \Phi)} \right\} \sigma_+ + H.c. \quad (2.32)$$

In the case of the ion trap, the harmonic frequency  $\omega_{pot}$  (in the order of MHz) is much smaller than the frequencies of the laser beam  $\omega_L$  and the atomic transition  $\omega_{ion}$  (in the order of THz). Under these circumstances we can neglect the rapidly oscillating terms including  $\omega_{ion} + \omega_L$ , making a *Rotating Wave Approximation*. It is useful to transform to an interaction picture via  $H_{INT} = U^\dagger H_{int} U$  with  $U = e^{-\frac{i}{\hbar} H_0 t}$ , resulting in the simplified expression for the interaction Hamiltonian [[Leibfried 2003](#)]:

$$H_{INT} = \frac{\hbar\Omega_0}{2} e^{-i\delta t} e^{i\Phi} \exp \left\{ i\eta \left( a e^{-i\omega_{pot} t} + a^\dagger e^{i\omega_{pot} t} \right) \right\} \sigma_+ + H.c. \quad (2.33)$$

where the detuning is given by  $\delta = \omega_L - \omega_{ion}$ .

The position operator  $x$  was substituted in the usual way (see eq. (2.21)) with the creation and annihilation operators and we introduced the Lamb-Dicke parameter  $\eta$  as

$$\eta = k_L \cos \theta \sqrt{\frac{\hbar}{2m\nu}} \quad (2.34)$$

---

<sup>1</sup>The diagonal dipole matrix elements vanish because the dipole interaction is an odd parity operator and the atomic states have either odd or even parities. Additionally, the matrix element must take only real values, which implies  $d_{eg} = d_{ge}$ .

where  $\theta$  is the angle between the k-vector of the laser field and the oscillation axis. We will discuss the Lamb-Dicke Parameter and its implications at further extend in section 2.3.2.

We see from equation (2.33) that the interaction Hamiltonian couples the internal states of the ion with the external vibration modes. It is useful to introduce a notation similar to the dressed-states of the Jaynes-Cummings model:

$$|g\rangle \otimes |n\rangle \equiv |g, n\rangle \quad \text{and} \quad |e\rangle \otimes |n\rangle \equiv |e, n\rangle \quad (2.35)$$

### 2.3.1 Coherent dynamics: Rabi oscillations

Since we are particularly interested in resonant transitions, we assume  $\delta = (l-m) \cdot \omega_{pot} = s \cdot \omega_{pot}$  where  $l$ ,  $m$  and  $s$  are integers. If we expand the exponent in equation (2.33) in  $\eta$ , it will result in terms containing a combination of the ions raising and lowering operators  $\sigma_{\pm}$  and the multiple of the annihilation and creation operators  $n \cdot a$  and  $m \cdot a^{\dagger}$ , respectively, rotating with a frequency  $\delta$ . Resulting in a coupling of the manifold of states  $|g, n\rangle$  and  $|e, n+s\rangle$  with a coupling strength, the so called Rabi frequency  $\Omega_{n, n+s}$  given by [Wineland 1979]:

$$\begin{aligned} \Omega_{n, n+s} &= \Omega_{n+s, n} = \Omega_0 \cdot \left| \langle n+s | e^{i\eta(a+a^{\dagger})} | n \rangle \right| \\ &= \Omega_0 e^{-\eta^2/2} \eta^{|s|} \sqrt{\frac{(n_{<})!}{(n_{>})!}} L_{n_{<}}^{|s|}(\eta^2) \end{aligned} \quad (2.36)$$

where  $n_{<}$  ( $n_{>}$ ) is the lesser (greater) of  $n$  and  $n+s$ ,  $\eta$  is the Lamb Dicke paramter, and  $L_{n_{<}}^{|s|}(\eta^2)$  is the generalized Laguerre polynomial

$$L_{n_{<}}^{|s|}(\eta^2) = \sum_{m=0}^{n_{<}} (-1)^m \binom{n_{<} + |s|}{n_{<} - m} \frac{\eta^{2m}}{m!} \quad (2.37)$$

The transitions  $|g, n\rangle$  and  $|e, n+s\rangle$  are often called blue (red) sideband transition for  $s > 0$  ( $s < 0$ ) and the  $|g, n\rangle \leftrightarrow |e, n\rangle$  - transition is a so called carrier transition. The occupation probability for one of two coupled states, for example on a blue sideband transition between  $|g, n\rangle$  and  $|e, n+1\rangle$ , can be driven by applying a laser beam with the detuning  $\delta = +\omega_{pot}$ , resulting in so called Rabi oscillations on the blue sideband. In an ideal case, the occupation probability is oscillating between 0 and 1 with the Rabi

## 2. THEORETICAL FOUNDATION

---

frequency  $\Omega_{n,n+1}$ . Up to this point, we made no approximations for the Lamb-Dicke parameter  $\eta$ .

### 2.3.2 Lamb-Dicke regime

Assuming the extension of the ion's wave function is much smaller than the wavelength, the ion is confined to the Lamb-Dicke regime where  $\eta\sqrt{n} \ll 1$  must hold for all times. The interaction Hamilton operator simplifies in the Lamb-Dicke regime to

$$H_{LDR} = \frac{\hbar\Omega_0}{2} e^{-i\delta t} e^{i\Phi} \left\{ 1 + i\eta \left( a e^{-i\omega_{pot}t} + a^\dagger e^{i\omega_{pot}t} \right) \right\} \sigma_+ + H.c. \quad (2.38)$$

In the Lamb-Dicke regime there are only three resonances:

The first one is the carrier resonance. On a carrier transition the states  $|g, n\rangle$  and  $|e, n\rangle$  are coupled and oscillate with the frequency  $\Omega_0$ . The motional state remains unchanged.

The transition  $|g, n\rangle \leftrightarrow |e, n+1\rangle$  resonant for  $\delta = +\omega_{pot}$  is called the blue sideband and oscillates with Rabi frequency  $\Omega_{n,n+1} \approx \Omega_0\eta\sqrt{n+1}$ .

The resonant part for  $\delta = -\omega_{pot}$  is the so called red sideband and drives transitions of the type  $|g, n\rangle \leftrightarrow |e, n-1\rangle$  with Rabi frequency  $\Omega_{n,n-1} \approx \Omega_0\eta\sqrt{n}$ .

The respective Hamiltonians take the following forms:

$$H_{car} = \frac{\hbar\Omega_0}{2} (\sigma_+ e^{i\Phi} + \sigma_- e^{-i\Phi}) \quad (2.39)$$

$$H_{bsb} = \frac{\hbar\Omega_0}{2} \eta (a^\dagger \sigma_+ e^{i\Phi} + a \sigma_- e^{-i\Phi}) \quad (2.40)$$

$$H_{rsb} = \frac{\hbar\Omega_0}{2} \eta (a \sigma_+ e^{i\Phi} + a^\dagger \sigma_- e^{-i\Phi}) \quad (2.41)$$

### 2.3.3 Spectroscopy of the motional sidebands

For resolved sideband spectroscopy we make use of the quadrupole transition  $4^2S_{1/2} - 3^2D_{5/2}$ . The ion is prepared in the internal ground state  $4^2S_{1/2}$  and the frequency of an applied laser beam at 729 nm is scanned in discrete steps. For each measuring point, typically consisting of a few hundred individual measurements with fixed frequency, the laser beam is applied for a fixed duration, resulting in a probability that the ion has been

excited to the metastable state. In the Lamb-Dicke regime the motional sidebands are resolved and with this simple method we are able to measure the motional frequencies of the ion.

A calculation for a spectrum “outside of the Lamb-Dicke regime” is described in section 4.5.1.

The different available transitions, including the Zeeman substructure, are shown in figure 2.10. The different subtransitions can be accessed experimentally by inserting the laser beam in different angles to the magnetic field and with different polarizations. Only the sublevels with a projection on the  $k$ -vector of the spectroscopy laser can be observed, hence only the red transitions are observable in the membrane trap.

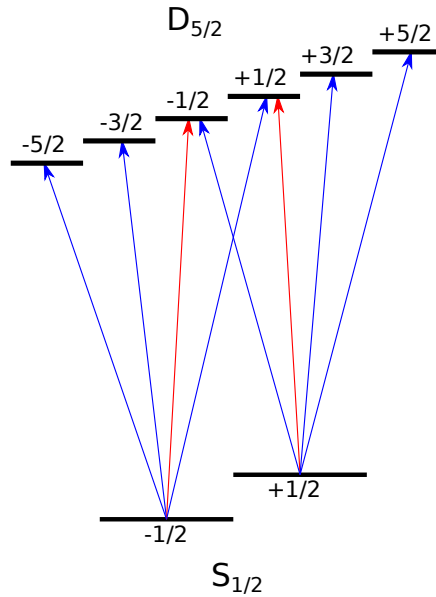


**Figure 2.10: Zeeman substructure of the spectroscopy transition** - The allowed subtransitions between the  $S_{1/2}$ -state and  $D_{5/2}$ -state which is used for sideband spectroscopy. The transitions, which can be observed in the membrane trap, are colored red.

## 2. THEORETICAL FOUNDATION

---

### 2.4 Vibrations of a membrane

---

In this section, we discuss how the membrane is characterized by its eigenfrequencies and the respective quality factor and how the Hamilton operator for the membrane vibrations can be expressed. We have to distinguish between the classical approach, when the membrane is in a thermal regime, and the quantum mechanical approach, when the membrane oscillations become quantized. At the end of this section, we give a short introduction to the Michelson interferometer and how it can be used to measure vibrations.

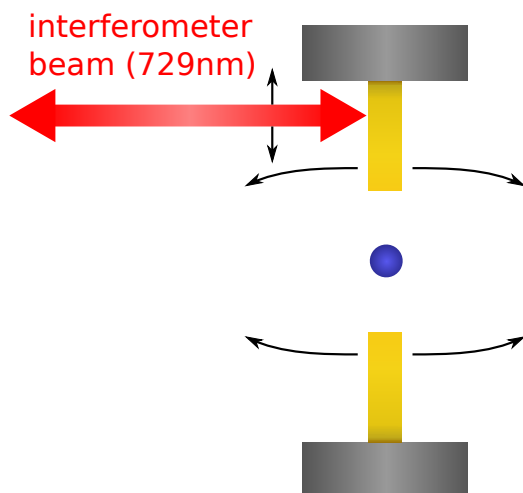


**Figure 2.11: Vibrations of a membrane** - The vibrations of the membrane are measured using an interferometer or the ion.

#### 2.4.1 Vibrations of a classical membrane

Consider a homogeneous oscillating membrane, stretched in a plane of negligible thickness by a uniform tension  $T$  and having a mass  $\rho$  per unit area. Furthermore, the equilibrium position of the membrane is the  $xy$  plane and the vibration displacement perpendicular to this plane will be given by  $z(x, y, t)$ .

In figure 2.12 we see a schematic drawing of a stretched plane membrane.

If the side  $dx$  ( $dy$ ) is vibrating, a force  $Tdy$  ( $Tdx$ ) is acting on the side, which tends

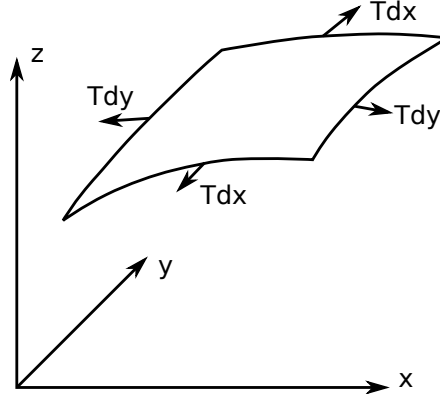


**Figure 2.12: Scheme for the stretched plane membrane** - On the vibrating membrane in  $z$ -direction acting forces in  $x$ - and  $y$ -direction induced by the tension  $T$ .

to restore the element to its equilibrium position. That means the force  $Tdy$  along an element of length  $dx$  produces a force [Pain 2005]:

$$Tdy \frac{\partial^2 z}{\partial x^2} dx \quad (2.42)$$

and another force  $Tdx$  acting on an element of length  $dy$  produces a force

$$Tdx \frac{\partial^2 z}{\partial y^2} dy. \quad (2.43)$$

Using Newton's law we find that the sum of these restoring forces acting in  $z$ -direction is equal to the mass of the element  $\rho dx dy$  multiplied by its perpendicular acceleration in direction of the  $z$ -axis

$$Tdy \frac{\partial^2 z}{\partial x^2} dx + Tdx \frac{\partial^2 z}{\partial y^2} dy = \rho dx dy \frac{\partial^2 z}{\partial t^2} \quad (2.44)$$

Simplifying equation (2.44), we end up with the *wave equation* in two dimensions

$$\frac{\partial^2 z}{\partial x^2} + \frac{\partial^2 z}{\partial y^2} = \frac{\rho}{T} \frac{\partial^2 z}{\partial t^2} = \frac{1}{c^2} \frac{\partial^2 z}{\partial t^2} \quad (2.45)$$

where

$$c^2 = \frac{T}{\rho} \quad (2.46)$$

## 2. THEORETICAL FOUNDATION

---

Now we need to define the initial conditions. The membrane is fixed at its edges, hence the displacement is given by

$$z(x_0, y_0, t) = 0 \quad \forall t \quad (2.47)$$

where  $x_0$  and  $y_0$  are points on the edge of the membrane. Additionally, we define the following initial conditions

$$z(x, y, 0) := f(x, y) \quad (2.48)$$

$$\frac{\partial z}{\partial t}(x, y, 0) := g(x, y) \quad (2.49)$$

For the general solution, we make an ansatz where we separate the position and time coordinates

$$z(x, y, t) = u(x, y)v(t) \quad (2.50)$$

Inserting our ansatz into the wave equation (2.45), we find the following expression

$$\frac{\Delta u(x, y)}{u(x, y)} = \frac{1}{c^2} \frac{\ddot{v}(t)}{v(t)} =: -\lambda \quad (2.51)$$

The equation  $\frac{\Delta u(x, y)}{u(x, y)} = -\lambda$  can be expanded to a form equivalent to the so called *Helmholtz equation*

$$\Delta u(x, y) + \lambda u(x, y) = 0 \quad (2.52)$$

and the time dependent part of the equation can be expressed as

$$\ddot{v}(t) + \omega^2 v(t) = 0 \quad \text{where} \quad \omega := c\sqrt{\lambda} \quad (2.53)$$

The time dependent equation (2.53) is solved using the characteristic polynomial and the solution is given by

$$v(t) = c \cos(\omega t) + \tilde{c} \sin(\omega t) \quad c, \tilde{c} \in \mathbb{R} \quad (2.54)$$

Without defining the form of the membrane more precisely, an exact solution for  $u(x, y)$  can not be found. But it can be shown, that  $u(x, y)$  can be expressed in the following form

$$u(x, y) = \sum_{n=1}^{\infty} c_n u_n(x, y) \quad c_n \in \mathbb{R} \quad (2.55)$$

Hence the general solution of the two dimensional wave equation is given by

$$z(x, y, t) = \sum_{n=1}^{\infty} u_n(x, y) (a_n \cos(\omega_n t) + b_n \sin(\omega_n t)) \quad (2.56)$$

where the coefficients  $a_n$  and  $b_n$  are defined by the initial conditions

$$a_n = \frac{1}{\|u_n\|^2} \int f(x, y) u_n(x, y) dV \quad (2.57)$$

$$b_n = \frac{1}{\omega_n \|v_n\|^2} \int g(x, y) u_n(x, y) dV \quad (2.58)$$

and  $\omega_n = c\sqrt{\lambda_n}$ .

### The rectangular membrane

Now we analyze the special case of a rectangular membrane that is fixed at the edges and in an equilibrium position:

$$0 < x < a, \quad 0 < y < b$$

$$z(x, 0, t) = 0 \quad z(x, b, t) = 0 \quad 0 \leq x \leq a \quad \forall t \quad (2.59)$$

$$z(0, y, t) = 0 \quad z(a, y, t) = 0 \quad 0 \leq y \leq a \quad \forall t \quad (2.60)$$

Using the ansatz  $u(x, y) = X(x)Y(y)$  the space dependent wave equation expands to

$$\frac{X''(x)}{X(x)} = - \left( \frac{Y''(y)}{Y(y)} + \lambda \right) =: -\nu \quad (2.61)$$

The left side of this equation simplifies to the eigenvalue problem

$$X''(x) + \nu X(x) = 0 \quad (2.62)$$

with

$$X(0) = X(a) = 0$$

Solving the eigenvalue problem gives us the eigenvalues  $\nu_n = \frac{\pi^2 n^2}{a^2}$  and the respective eigenvectors  $X_n(x) = \sin\left(\frac{\pi n x}{a}\right)$ , where  $n$  is an integer. Considering the just found solutions for the eigenvalues  $\nu_n$ , the eigenvalue problem for  $Y(y)$  expands to

$$Y''(y) + \underbrace{(\lambda - \nu_n)}_{=: \chi_m} Y(y) = 0 \quad (2.63)$$

## 2. THEORETICAL FOUNDATION

---

with

$$Y(0) = Y(b) = 0$$

For this problem we find the eigenvalues  $\chi_m = \frac{\pi^2 m^2}{b^2}$  with the respective eigenvectors  $Y_m(y) = \sin\left(\frac{\pi m y}{b}\right)$ , where  $m$  is an integer.

Combining both solutions, we end up with the following eigenvalues and eigenvectors for our special case of a rectangular membrane

$$\lambda_{nm} = \frac{\pi^2 n^2}{a^2} + \frac{\pi^2 m^2}{b^2} \quad \text{and} \quad u_{nm}(x, y) = \sin\left(\frac{\pi n x}{a}\right) \sin\left(\frac{\pi m y}{b}\right) \quad (2.64)$$

Finally, adding the solution for the time dependent wave equation (see eq. (2.54)) the universal solution for the oscillation of the rectangular membrane is given by the superposition of all solutions

$$z_{nm}(x, y, t) = (a_{nm} \cos(\omega_{nm} t) + b_{nm} \sin(\omega_{nm} t)) \sin\left(\frac{\pi n x}{a}\right) \sin\left(\frac{\pi m y}{b}\right) \quad (2.65)$$

$$z(x, y, t) = \sum_{n=1}^{\infty} \sum_{m=1}^{\infty} (a_{nm} \cos(\omega_{nm} t) + b_{nm} \sin(\omega_{nm} t)) \sin\left(\frac{\pi n x}{a}\right) \sin\left(\frac{\pi m y}{b}\right) \quad (2.66)$$

where  $n, m \in \mathbb{N}$  and  $\omega_{nm} = c\sqrt{\lambda_{nm}} = \pi c \sqrt{\left(\frac{n}{a}\right)^2 + \left(\frac{m}{b}\right)^2}$  are the eigenfrequencies for the different modes of the membrane characterized by  $n, m$ . Hence the frequency of the fundamental mode is

$$\omega_{11} = \pi c \sqrt{\left(\frac{1}{a}\right)^2 + \left(\frac{1}{b}\right)^2} \quad (2.67)$$

In figure 2.13 examples for different normal modes are displayed. The first index gives the number of antinodes in  $x$ -direction and the second index gives the number of antinodes in  $y$ -direction.

### 2.4.2 The membrane as quantum mechanical oscillator

When the membrane is cooled to very low temperatures, its motion becomes quantized and therefore a quantum mechanical description is necessary. The quantized vibrational modes of the membrane can be described by the model of the quantum mechanical

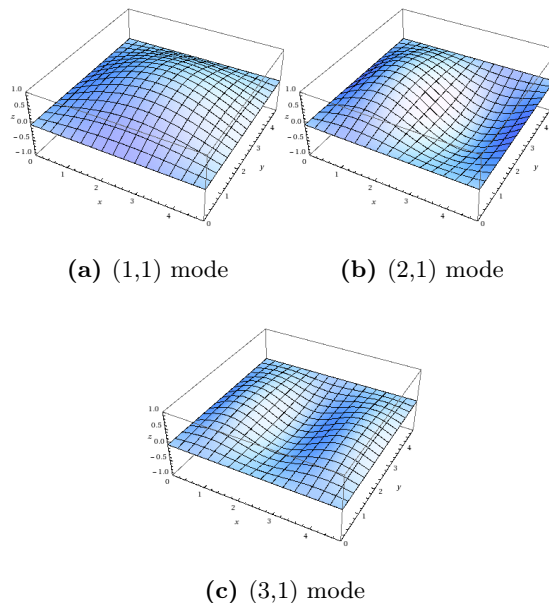


**Figure 2.13:** The first three normal modes of a rectangular membrane

harmonic oscillator. A quantum mechanical derivation of the harmonic oscillator can be found in the common literature, e.g., [Cohen-Tannoudji 2007].

The Hamilton operator for the quantum mechanical oscillator is then given by

$$H_{mem} = \sum_{n,m} \hbar\omega_{nm} b_{nm}^\dagger b_{nm} \quad (2.68)$$

where  $b_{nm}$  and  $b_{nm}^\dagger$  are the lowering and raising operators for the fundamental mode  $z_{nm}$  with frequency  $\omega_{nm} = \pi c \sqrt{\left(\frac{n}{a}\right)^2 + \left(\frac{m}{b}\right)^2}$ .

### 2.4.3 Measuring vibrations with a Michelson interferometer

Finally, we will discuss how to measure the vibrations of a membrane. For this thesis, a special design Michelson interferometer was developed and setup (see section 3.2). In this section, the measuring of vibrations with a Michelson interferometer will be briefly introduced.

The scheme of a typical Michelson interferometer, as it is also used in this thesis, is shown in figure 2.14.

## 2. THEORETICAL FOUNDATION

---

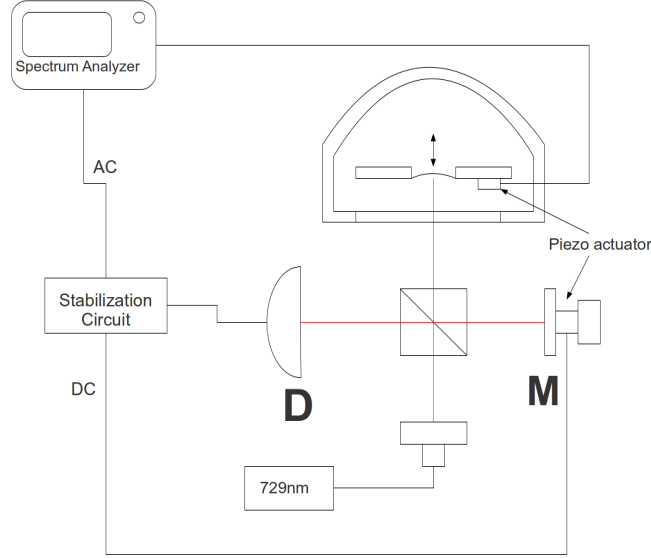


**Figure 2.14: Scheme of a Michelson interferometer** - The schematics of a typical Michelson interferometer, where the membrane acts as a vibrating mirror. The output signal of the photo diode is observed via a spectrum analyzer or oscilloscope and fed to the stabilization circuit, which controls the compensation mirror via a piezo actuator.

An incident laser beam is split at a beam splitter cube, and send towards a reference mirror and the vibrating object, i.e., the membrane. The vibration of the membrane changes the length of one of the interferometer arms, hence changes the interfering signal detected at a photo diode. For sinusoidal vibrations of the membrane, the detected signal takes the following form [Dobosz 1998]:

$$V(t) = V \cos(\phi_0 + \phi_m \cos(\omega t + \phi_s)) \quad (2.69)$$

where  $V$  is the Voltage amplitude,  $\phi_0$  is the initial phase of the signal, which depends on the initial optical path difference,  $\omega$  is the angular frequency,  $\phi_s$  is the vibration zero phase and  $\phi_m = 2\pi d/\lambda$  is the modulation phase amplitude, where  $d$  is the amplitude of the vibrating object and  $\lambda$  the wavelength of light.

The displacement of the membrane corresponding to the distance between two adjacent fringes of the same kind, e.g., intensity minima or maxima, is given by  $l = \lambda/2$ .

The resonance frequency can be measured by scanning the excitation frequency with a spectrum analyzer and observing the feedback of the photo diode.

## 2.5 Interactions in the combined system of ion and membrane

---

In this chapter we study the interactions in the coupled system of ion motion along the  $z$  axis and the fundamental modes of the membrane. We start by deriving an expression for the Hamiltonian for the coupling of the combined system and discuss ways to reach the coupling.

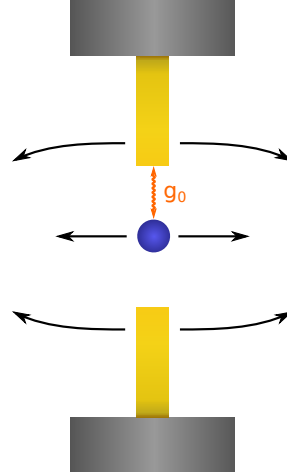


**Figure 2.15: Coupling of an ion to a membrane** - The coupling of the ion to the membrane is expressed by the coupling strength  $g_0$ .

At first we need to find an expression to describe the coupling of the ion and the membrane. The coupling is caused by the Coulomb interaction between ion and the charge distribution on the membrane induced by the applied r.f.-voltage. In the previous sections we learned that the ion motion in a harmonic potential is well described by a quantum mechanical harmonic oscillator and we found an expression for the membrane equivalent to the harmonic oscillator. Hence the coupling of the two systems simplifies to coupling two harmonic oscillators. The coupling term of such a system has the following form [Tian 2004]:

$$H_{mem-ion} = i\frac{\hbar}{2}g_0 \sum_i \left( b_{nm}^\dagger a + H.c. \right) \quad (2.70)$$

## 2. THEORETICAL FOUNDATION

---

where  $g_0$  is the coupling constant,  $b_{nm}(b_{nm}^\dagger)$  and  $a(a^\dagger)$  are the annihilation and creation operators of the fundamental mode  $z_{nm}$  with eigenfrequency  $\omega_{nm}$  and the motion of the ion, respectively, as defined in the previous sections.

The coupling constant  $g_0$  is given as

$$g_0 = \omega_{ion} z_{nm} \sqrt{\frac{m_{ion}}{m_{mem}}} \quad (2.71)$$

where  $\omega_{ion}$  is the frequency of the ion parallel to the membrane motion, in our case the axial frequency.  $z_{nm}$  is the eigenfunction of the  $n$ th,  $m$ th vibrational mode of the membrane at the position of the trap center and the respective masses of the ion and the membrane are  $m_{ion}$  and  $m_{mem}$ .

That means that the coupling between ion and membrane is proportional to the frequency of the ion and the vibrations of the membrane, while reduced by the mass ratio  $m_{ion}/m_{mem}$ .

For a single ion with  $m_{ion} \approx 10^{-23}$  g and a Silicon membrane with  $m_{mem} \approx 10^{-4}$  g, we obtain a mass ratio of  $\sqrt{\frac{m_{ion}}{m_{mem}}} \approx 10^{-10}$ , resulting in a strong reduction of the coupling rate. The trap frequencies are limited by the experimentally achievable curvature of the harmonic potential, usually in the range of a few MHz. Next, the coupling constant  $g_0$  scales with the eigenfunction of the  $n$ th,  $m$ th vibrational mode of the membrane at the position of the trap center, which primarily depends on the material properties of the membrane. For the membrane used in our experiments, we found resonance frequencies in the range of 20 to 100 kHz.

Overall, the coupling constant  $g_0$  is typically in the regime of  $g_0/2\pi \approx 10^1 - 10^3$  1/s.

### Reaching the strong coupling regime

In order to reach the strong coupling regime, the coupling constant  $g_0$  needs to be much larger than the rate of decoherence. The rate of decoherence scales with the main dissipation factors of the ion - membrane system, i.e., the mechanical and electrical noise. We will discuss these factors in detail in section 2.6.

For now, the simple picture that the mechanical noise decreases with the temperature of the membrane and that the ion is well isolated from the environment due to the ultra-high vacuum setup, while the key decoherence factor, i.e., the heating rate of the ion, can be minimized sufficiently, allowing to accomplish decoherence times of a few hundred ms, is sufficient for further discussions.

## 2.5 Interactions in the combined system of ion and membrane

---

As mentioned above, the coupling constant  $g_0$  needs to be much larger than the dissipation factors. A rather obvious way to improve the coupling constant is to increase the number of ions. The coupling constant scales with  $\sqrt{N}$  where  $N$  is the number of ions in the trap. The collectively enhanced coupling is then  $g_N = \sqrt{N}g_0$  simply derived from equation (2.71) by substituting  $m_{ion}$  with the mass of  $N$  ions  $N \cdot m_{ion}$ . The disadvantage of this method is that we lose the excellent motional control achievable for a single ion.

Instead of increasing the number of ions, a different approach is to work with lighter ions, since the trap frequency scales with  $1/m_{ion}$  and the coupling constant only with  $\omega_{pot}\sqrt{m_{ion}}$  resulting in a higher coupling strength. Unfortunately, the achievable increase in coupling strength is rather small.

Another way to increase the coupling constant is to increase the curvature of the trapping potential, resulting in higher trap frequencies and therefore higher values for  $g_0$ . This can be achieved by smaller traps or higher applied voltages. This method is limited by the possible compensation, which must be applied by electrodes not mounted on the oscillator.

Increasing the coupling strength on the side of the mechanical oscillator can be achieved by using smaller, lighter oscillators, such as nanotubes, or by using thinner and smaller membranes with more holes to reduce the mass. Decreasing the mass of the oscillator can increase the coupling strength in two orders of magnitude compared to massive oscillators as a Silicon membrane.

The coupling of an ion to the smallest available oscillator, another ion, was recently achieved [Brown 2010]. In this experiment the motional frequencies of two ions in one potential well can be brought into or out of resonance with each other, enabling a tunable interaction.

Another approach to reach strong coupling, which is independent from the mass ratio, was described recently and can be found in reference [Hammerer 2009]. By using a configuration which realizes a coupled oscillator dynamics linear in the displacement of atom and membrane, they found a theoretical solution of the coupling strength, which is independent from the mass ratio. If this could be proven in experiment, it would give rise to a whole new range of coupling schemes.

## 2. THEORETICAL FOUNDATION

---

### 2.6 Interactions with the environment

---

In this section we study the influences of the environment on the interactions of the ion and the membrane, as well as, how to minimize them. Then the results found in this section for the dissipation rates of both coupling partners can be put into context with the coupling constant described in the previous section.

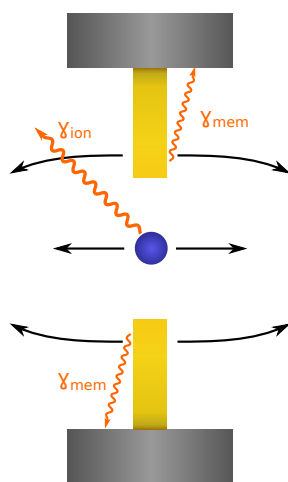


**Figure 2.16: Interactions with the environment** - The relevant interactions of the ion and the membrane with the environment are summarized in  $\gamma_{ion}$  and  $\gamma_{mem}$ , respectively.

#### 2.6.1 Interactions of the ion with the environment

Trapped ions are one of the best controllable quantum mechanical systems and are well isolated due to no direct contact with the environment. In particular, ion motion can be controlled on the single quantum level and high coherence times can be achieved.

In our experiment we are interested in the axial phonon number, which is the one coupling to the membrane. The main dissipation factor is the heating rate due to electric field fluctuations. Anharmonicities in the trap result in small fluctuating voltages, hence small drifts of the potential, leading to a heating rate. For our system with an ion of charge  $q$  and mass  $m$  trapped in a harmonic potential well subject to a fluctuating

electric field drive  $\epsilon(t)$ , the Hamiltonian can be expressed by

$$H(t) = H_{pot} + q\epsilon(t)m \quad (2.72)$$

From first-order perturbation theory, the rate of transition from the ground state of the well ( $|n = 0\rangle$ ) to the first excited state ( $|n = 1\rangle$ ) can be derived

$$\Gamma_{0\leftarrow 1} = \frac{q^2}{4m\hbar\omega_{pot}} S_E(\omega_{pot}) \quad (2.73)$$

with

$$S_E(\omega_{pot}) = 2 \int_{-\infty}^{\infty} d\tau e^{i\omega_{pot}\tau} \langle \epsilon(t)\epsilon(t + \tau) \rangle \quad (2.74)$$

where  $S_E(\omega_{pot})$  is the spectral energy density of electric field fluctuations.

The heating rate, given by the rate of change of the average thermal occupation number, can be approximated by the transition rate in eq. (2.73) [Turchette 2000]:

$$\dot{n} = \Gamma_{0\leftarrow 1} = \frac{q^2}{4m\hbar\omega S_E(\omega)} \quad (2.75)$$

where  $\omega$  is the frequency of the mode to be considered, in our case the axial mode.

Other effects are induced, e.g., by micromotion or by arbitrary magnetic fields, but are not influencing the temperature.

The high frequent micromotion influences the fluorescence during detection, but it is possible to minimize the micromotion by compensating with static electrical fields.

Arbitrary magnetic fields disturb the spectroscopy, due to shifting Zeeman levels, but can be minimized via a shielding with high magnetic permeability or by applying compensating magnetic fields.

All these effects are very small in the case of the ion trap.

So in our case the relevant decoherence rate  $\gamma_{dec}$  is induced only by effects influencing the axial vibrational mode of the ion.

Typically coherence lifetimes of entangled states are in the range of several seconds, so the decoherence rate is not the limiting factor in the combined system of ion and mechanical oscillator.

## 2. THEORETICAL FOUNDATION

---

### 2.6.2 Interactions of the membrane with the environment

The interactions of the membrane with the environment are magnitudes higher compared to the ion's interactions. Although the membrane is also placed in an ultra-high vacuum, it is in direct contact with the outside world via the connection of the mount. This means the membrane is connected to a whole damping system consisting of mount, vacuum chamber, and experiment table.

The damping mechanisms influencing the membrane motion are characterized by the quality factor. The quality factor for an oscillating system is given by the ratio of the stored energy and the energy dissipated per cycle and can be expressed as

$$Q = \frac{f_0}{\Delta f} = \pi \frac{f_0}{\delta} \quad (2.76)$$

where  $f_0$  is the resonance frequency,  $\Delta f$  is the bandwidth and  $\delta = 1/T_{decay}$  is the logarithmic decrement.

For typical mechanical oscillators quality factors in the order of  $10^4$ – $10^7$  can be achieved.

The decoherence of a mechanical oscillator is typically fast despite high quality factors. The coupling of the membrane to the environment introduces a dependence on the temperature  $T$  of the bath. The resulting decoherence rate is given as

$$\gamma_{mem,dec} = \frac{k_B T}{\hbar Q} \quad (2.77)$$

So not only are high quality factors important to reach small decoherence rates, but also low temperatures. The high decoherence rate of the mechanical oscillator is the key limiting factor in the system of membrane and ion and it is necessary to find ways to minimize this decoherence rate in order to reach the strong coupling limit, where  $g_0 > (\gamma_{ion,dec}, \gamma_{mem,dec})$ .

# 3

## Experimental Setup

### Contents

---

<b>3.1</b>	<b>The membrane trap . . . . .</b>	<b>38</b>
3.1.1	Preparation of a membrane as ion trap . . . . .	38
3.1.2	Placing the ion trap in an ultra-high vacuum system . . . . .	39
3.1.3	Setup of the ultra-high vacuum system . . . . .	41
3.1.4	The laser system of the membrane ion trap . . . . .	42
3.1.5	Apparatus for the detection of an ion . . . . .	43
3.1.6	The complete setup of the oscillating ion trap . . . . .	44
<b>3.2</b>	<b>The interferometer for vibration measurement . . . . .</b>	<b>46</b>
3.2.1	The setup of the interferometer . . . . .	46
3.2.2	Implementing a stabilization circuit . . . . .	48

---

In this chapter the experimental setup of the membrane trap and all the essential components is described. At first, the membrane trap itself is discussed in detail, starting with a description of the membrane used for the experiments in this thesis and the fabrication process for an oscillating ion trap. Then we take a closer look at the ultra-high vacuum setup surrounding the membrane and providing access for the elaborate laser system, which will be described afterwards. The first section of this chapter ends with the description of the imaging optics used for detection.

Next, the interferometer for vibration measurements, specially designed for this setup, is described and at the end we study the stabilization circuit, implemented for the noise reduction of the interferometer.

### 3. EXPERIMENTAL SETUP

---

#### 3.1 The membrane trap

---

For the construction of an oscillating ion trap two main requirements need to be fulfilled. The necessary structure of an ion trap must be provided, but also allowing the oscillation of the trap itself. In this section we show how to implement the structure of a ring ion trap in a membrane. Our setup allows the trapping of the ion using holes in a gold coated membrane, which is placed inside a ultra-high vacuum setup providing the necessary isolation from environment, as well as allowing the access to the ion of the required laser system and detection apparatus.

##### 3.1.1 Preparation of a membrane as ion trap

In the experiments described in this thesis, a *single crystal (100) Silicon membrane*<sup>1</sup> is prepared as an ion trap. High-quality Si wafers of (100) orientation are readily available in a wide range of diameter and thickness. Starting with a  $380\ \mu\text{m}$  thick  $10 \times 10\ \text{mm}$  Si wafer, a  $4.8 \times 4.8\ \text{mm}$  window is etched to a thickness of  $2.0\ \mu\text{m}$ . The tension of the membrane is inflicted by the connection to the frame, which is fixated in a specially designed mount (see below).

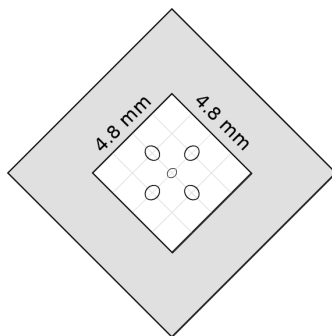


**Figure 3.1: Schematic arrangement of the holes on the membrane** - The center hole size is  $110 \times 100\ \mu\text{m}$  and the size of the four outer holes is  $165 \times 150\ \mu\text{m}$ , which are positioned on half the distance between center hole and frame to maximize coupling to the (1,2)-,(2,1)-vibrational modes.

For preparing the membrane as an ion trap, five different holes are cut into the Si

---

<sup>1</sup>purchased at <http://www.norcada.com>, part number: SM10480N

### 3.1 The membrane trap

---

membrane at the Max Planck institute for solid state research<sup>1</sup>, providing the geometry of a ring Paul trap. The center hole size is  $110 \times 100 \mu\text{m}$  and four holes of equal size ( $165 \times 150 \mu\text{m}$ ) are symmetrically arranged around the center hole (see fig. 3.1). Every hole acts as an individual ion trap, giving us the possibility to trap ions at different positions on the membrane, and therefore to probe different modes of vibration.

Next, both sides of the membrane are coated with 10 nm Chromium and 100 nm gold. The coating is applied to achieve a clean surface and a high reflectivity of the membrane. The coating also provides good electric contact and prevents reactions with water and other vacuum disturbing elements.

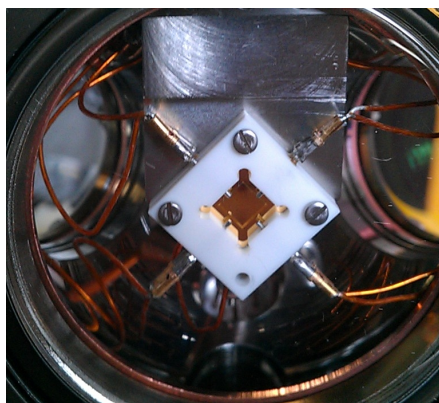


**Figure 3.2: A picture of the final membrane** - The final membrane readily installed in the vacuum chamber. The  $4.8 \times 4.8 \text{ mm}$  window and the edges of the frame are visible, as well as the compensation electrodes of the top layer.

A picture of the final membrane is displayed in figure 3.2 and a magnification of the membrane showing three of the five holes is displayed in figure 3.3.

Now that the membrane is prepared as an oscillating ion trap, it is placed inside an ultra-high vacuum setup to create the necessary environment.

#### 3.1.2 Placing the ion trap in an ultra-high vacuum system

The membrane ion trap needs to be placed inside an ultra-high vacuum chamber to isolate it from the environment. For mounting the ion inside a vacuum chamber a

---

<sup>1</sup><http://www.fkf.mpg.de>

### 3. EXPERIMENTAL SETUP

---

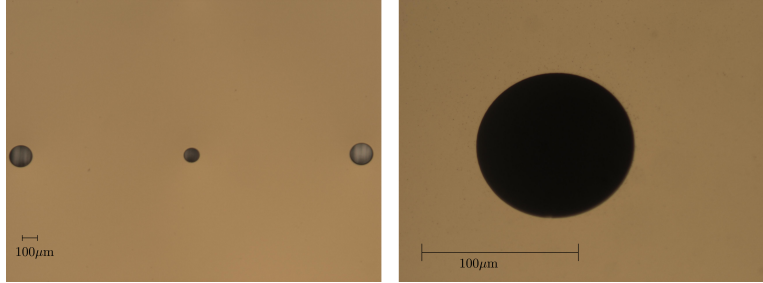


**Figure 3.3: Magnification of the holes in the membrane** - The left picture shows a magnified picture of the holes on the membrane taken with a microscope. Two more holes, not visible in this picture, are arranged above and below the center hole at the same distance as the two outer holes visible in this picture. The right side shows the magnified center hole.

frame for the membrane was constructed, that can be connected to a mount inside the vacuum chamber.

The frame consists of two Marcor ceramic pieces, especially designed to provide optimal optical access to the membrane and electrically isolating it from the rest of the chamber. The membrane is fixated between the two Marcor pieces, one corner of the membrane is glued to the first Marcor piece to avoid any further movement during the installment inside the vacuum chamber, then the second Marcor piece is placed on top of the membrane. To position the frame with the membrane in the center of the front viewport of the vacuum chamber, the Marcor pieces are screwed to a mount, that is attached to the top of the chamber.

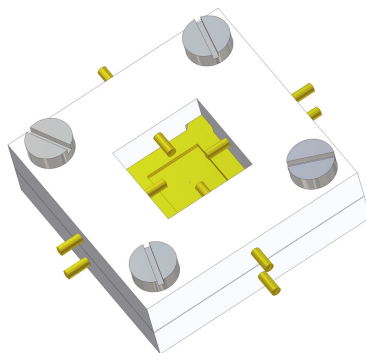


**Figure 3.4: Drawing of the mount** - The membrane is fixated between two pieces of Marcor ceramics. The Marcor pieces also provide symmetrically arranged feed-throughs for the compensation electrodes.

Each of the two Marcor pieces also includes four symmetrically arranged feed-throughs for the compensation electrodes (see fig. 3.4). The compensation electrodes consist of four symmetrically arranged pins in each Marcor layer. The distance of the pins to the center trap is  $d_1 = 25$  mm, the distance of all four pins to the membrane surface is  $d_2 = 15$  mm. If each of the four pins of one layer has the same potential, they can be interpreted as one virtual electrode, but they also provide the possibility to create more complex potentials, if required.

#### 3.1.3 Setup of the ultra-high vacuum system

The membrane ion trap is placed inside a vacuum chamber, with three viewports providing access for the necessary laser beams, two feed-throughs for the electrical wiring and two connections for the vacuum pumps and a valve. The vacuum chamber is made of unitary stainless steel.

One large viewport is placed at the front of the chamber and two smaller viewports are placed at an angle of  $45^\circ$  to the front viewport and  $90^\circ$  to each other at the backside of the chamber.

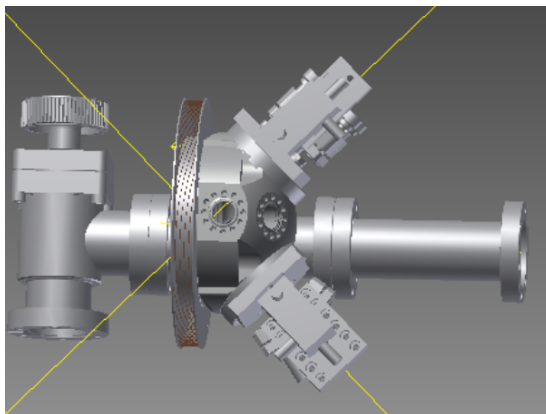


**Figure 3.5: Top view of the chamber** - The front viewport is framed by a coil, the small viewports are placed at an angle of  $45^\circ$  and have the mounts of the couplers attached. Also visible are the valve on the left side and on the right side a Titan sublimation pump can be inserted.

On top of the chamber an electrical feed-through for each of the compensation electrodes is installed, making it possible to control each of the eight compensation electrodes

### 3. EXPERIMENTAL SETUP

---

individually. Another electrical feed-through with an angle of  $45^\circ$  to the horizontal is installed at the bottom part of the chamber, used for the connection of the oven and the r.f.-voltage.

The r.f.-connection is wired to an helical resonator [Macalpine 1959] and an amplifier to provide the necessary high-voltages at the membrane trap. A frequency generator provides the required radiofrequency at  $f_{rf} = 30$  MHz with an amplitude of  $U_{rf} = 300 V_{zp}$ .

The oven for vaporizing the Calcium is resistively heated and directed towards the membrane at an angle of  $45^\circ$ . The Calcium atoms leave the oven as a thermal atomic beam towards all five trap holes of the membrane.

Additionally, there is a piezo actuator mounted to the top of the vacuum chamber, used to excite vibrations of the membrane.

The vacuum inside the chamber is maintained by a combination of an ion getter pump and a Titan sublimation pump.

#### 3.1.4 The laser system of the membrane ion trap

The three viewports of the vacuum chamber give complete access to the necessary laser beams required for trapping and controlling the ion. As we learned in section 2.1, four laser beams with different wavelenghts are required for trapping and cooling the ions.

The so called photo ionization lasers at 423 nm and at 375 nm, ionize the neutral Calcium atoms at the center of the trapping region [Gulde 2001]. This beam enters through one of the small viewports, therefore reaching the trap in an angle of  $45^\circ$ .

For Doppler cooling the ion and driving the fluorescence transition a laser beam at 397 nm is required. It enters the chamber through the second small viewport,  $90^\circ$  turned to the photo ionization beam.

Via the same viewport the combined beam of lasers at 854 nm and 866 nm enters the chamber. It is required to control the shelving of the ion in the metastable states.

The front viewport gives access to the beam of the interferometer, in our case we use a laser at 729 nm, and the detection apparatus, which will be described in the next section.

In figure 3.6 a schematic drawing of the previously described laser setup is displayed.

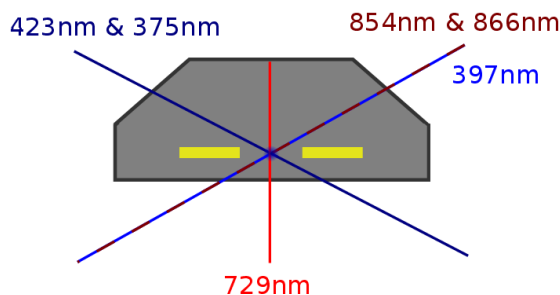


**Figure 3.6: Schematic drawing of the laser setup** - The photo ionization beam enters the chamber through the smaller left viewport, while the lasers with wavelengths 397 nm, 854 nm and 866 nm enter through the right viewport. The interferometer beam with a wavelength of 729 nm, which is also required for the sideband spectroscopy, accesses the chamber via the front viewport.

All the previously mentioned lasers are diode lasers, that are commercially available<sup>1</sup>. For the laser with wavelength 397 nm, a red laser diode in combination with a frequency doubling cavity produces the required ultraviolet light. For switching the lasers on and off, on a very small time base, we use acousto optical modulators (AOM), which can be controlled by the experimental control system.

A more detailed description of a similar laser system can be found in ref. [Poschinger 2010b, Ziesel 2008].

### 3.1.5 Apparatus for the detection of an ion

The detection apparatus primarily consists of an EMCCD-camera<sup>2</sup> for detecting the fluorescence of the trapped ions. For achieving the required focus at the position of the ion, a lens is mounted to an stage, that is adjustable in all three directions (i.e. x-y-z-direction). Via a construction of dove tail bars, the EMCCD-camera is connected to the system of lens and stage, attaching it to their movement. Hence, the focus of the detection system can be moved to each of the five holes or any other desired position on the membrane. This option is not only ideal for changing the point of view of the camera, but also allows the movement of the measuring point of the interferometer, which was specially implemented in this setup (see sec. 3.2). A schematic drawing of the detection apparatus is shown in figure 3.7.

<sup>1</sup>Firma TOPTICA-Photonics

<sup>2</sup>www.andor.com

### 3. EXPERIMENTAL SETUP

---

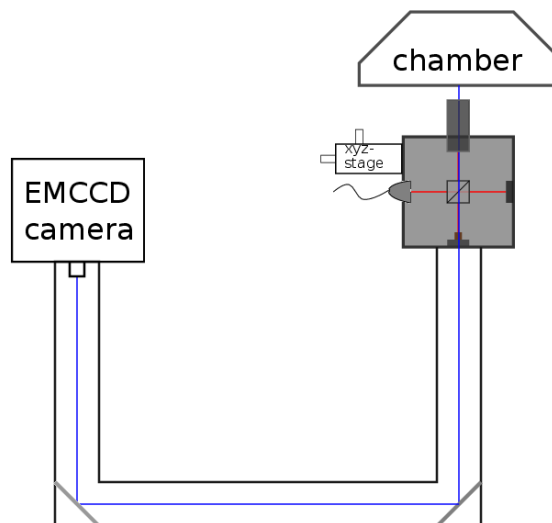


**Figure 3.7: Schematics of the detection apparatus** - The EMCCD camera is connected via dove tail bars to the stage and the lens. The interferometer is installed directly behind the lens.

#### 3.1.6 The complete setup of the oscillating ion trap

In figure 3.8 a picture of the whole setup is depicted. From top to bottom, we see the front view of the vacuum chamber with the membrane trap in the center of the front viewport, followed by the two stage interferometer including the imaging lens. Not in the picture is the EMCCD-camera, which is installed at the end of the imaging optics.

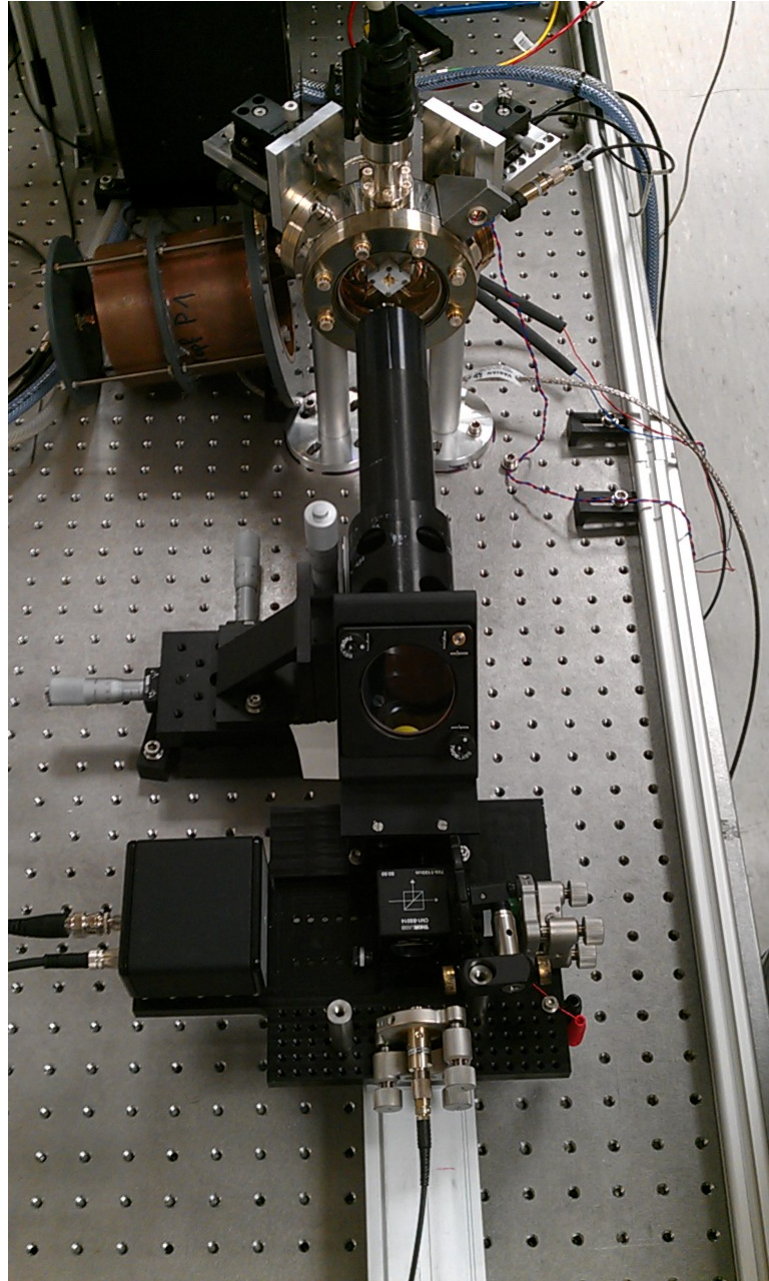


**Figure 3.8: Setup of the membrane trap including the interferometer** - The whole setup of the membrane trap is displayed here. At the top we see the center piece, the vacuum chamber, including the membrane trap in the middle of the front view port. Also visible are the helical resonator on the left side of the vacuum chamber and the interferometer at the bottom.

### 3. EXPERIMENTAL SETUP

---

## 3.2 The interferometer for vibration measurement

---

In this section the special design of the interferometer, developed to combine the detection apparatus and the Michelson interferometer, is introduced and the stabilization circuit, implemented to reduce noise and increase stability of the interferometer, is described.

### 3.2.1 The setup of the interferometer

The interferometer described here is a Michelson interferometer with a special design, making it possible to control the measurement point of the interferometer according to the point of view of the imaging optics.

A basic scheme of the interferometer is displayed in figure 3.9.

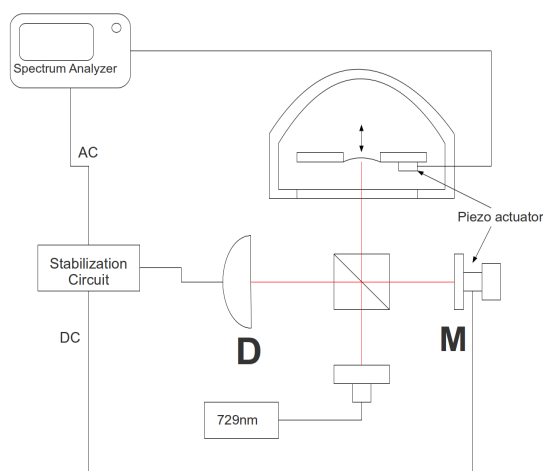


**Figure 3.9: Schematic drawing of the Michelson interferometer** - A laser beam with a wavelength of 729 nm is split at a beam splitter cube, one path leading towards a reference and compensation mirror, the other path towards the vibrating membrane. The reference and compensation mirror is connected to a piezo actuator, which is controlled by a stabilization circuit. After reflection at the reference mirror and the membrane, the beams interfere at the beam splitter and the signal is detected with a photo diode and an spectrum analyzer, which is also used to excite the piezo actuator mounted on the vacuum chamber.

The incoming laser beam is split at a beam splitter cube towards the vibrating mem-

### 3.2 The interferometer for vibration measurement

---

brane and a reference mirror. The reference mirror is mounted to a piezo actuator, which is controlled by the stabilization circuit (see sec. 3.2.2). After reflection at the mirror and the membrane, the two beams interfere at the beam splitter cube and the interference signal is detected with a photo diode. The output of the photo diode is then fed into an oscilloscope or a spectrum analyzer for further analysis and into the stabilization circuit for compensation feedback.

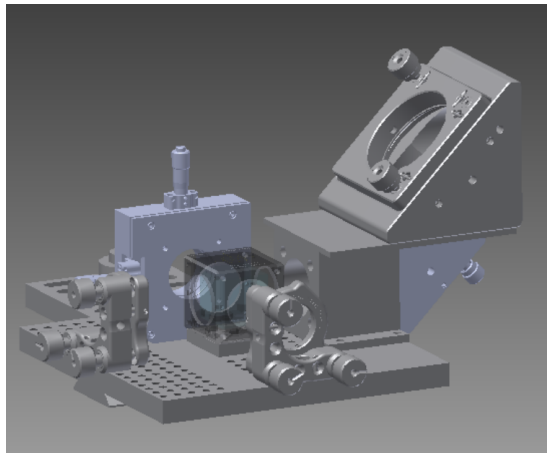


**Figure 3.10: The interferometer design** - This drawing of the interferometer shows the breadboard with the Michelson interferometer setup. The left mount is used for the output coupler of the laser beam, the right mount holds the reference mirror. In the center of the breadboard the beam splitter cube is mounted and on the left side we see the beam “lift”. Additionally, there is a lense mount for focusing the interfering beams on the photo diode, which can be fastened to the mount.

As mentioned above, the interferometer was designed to be integrated in the detection apparatus. A “two stage” design was developed to accomplish this. The setup of the interferometer is placed on a breadboard with a dove tail connection fitting perfectly into the detection apparatuses dove tail bars. The optical plane of the interferometer lies below the plane of the imaging optics, therefore we need to combine the measuring beam of the interferometer with the path of the imaging optics. This is achieved by a specially designed beam “lift”, consisting primarily of two mirrors. One mirror, high-reflective for 729 nm is tilted  $45^\circ$  to the interferometer plane, giving the measuring beam a vertical direction. Aligned on top of this mirror, tilted to  $-45^\circ$ , the second mirror couples the beam into the plane of the imaging optics, where it propagates through the lens towards the membrane. The second mirror is coated to be high-reflective for

### 3. EXPERIMENTAL SETUP

---

red light, but transmissive for blue light. This allows the so called imaging beam at 397nm to pass the “lift” to the EMCCD camera, while the interferometer beam at 729nm is reflected and propagates through the lift to the lower interferometer plane. For the interferometer beam and the imaging beam the same lens is used to focus on the membrane. The interferometer beam is adjusted ideally if it overlaps with the imaging path, combining measurement point of the interferometer and point of view of the camera. A drawing of the interferometer design is shown in figure 3.10.

#### 3.2.2 Implementing a stabilization circuit

For noise reduction of the interferometer, a stabilization circuit was implemented. It takes the feedback from the photo diode, filters and amplifies the slow drifting frequencies and controls the piezo actuator of the compensation mirror.

In figure 3.11 a schematic drawing of the stabilization circuit is depicted.

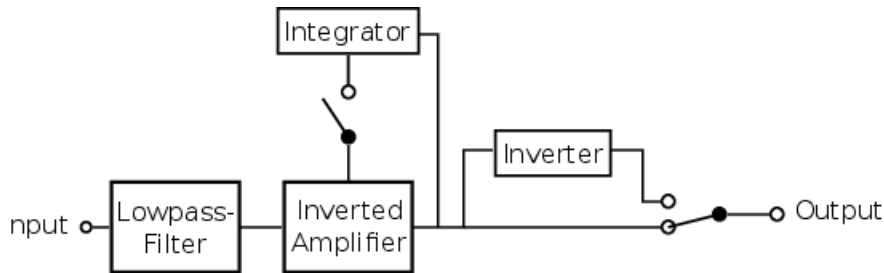


**Figure 3.11: Schematic drawing of the stabilization circuit** - The stabilization circuit is a combination of a lowpass filter and an tunable, inverted amplifier. Additionally, an integrating circuit can be turned on or off via a switch, as well as the inverting of the output. The circuit diagram can be found in the appendix A.1.

The stabilization circuit is a combination of different electrical elements. At first, there is a lowpass filter with a cut-off frequency of  $f_{cut} = \frac{1}{2\pi RC} = 10 \text{ kHz}$ . Next, there is an inverting amplification circuit, whose gain and offset are tunable via the two potentiometers. An integrating circuit can be additionally activated via a switch. At the output of the circuit an inverter is implemented, which can be switched on or off, as required. So if the signal of the photo diode is connected to the input, the low frequencies of the signal are filtered, phase shifted and amplified, if necessary also inverted. This

### **3.2 The interferometer for vibration measurement**

output is fed to the piezo actuator of the compensation mirror, hence stabilizing the interferometer.

### 3. EXPERIMENTAL SETUP

---

# 4

## Numerical Simulations and Experimental Results

### Contents

---

<b>4.1</b>	<b>Simulating the membrane ion trap . . . . .</b>	<b>52</b>
4.1.1	Simulations of the ponderomotive potential . . . . .	53
4.1.2	Simulations of the trajectory of the ion . . . . .	56
<b>4.2</b>	<b>Preliminary measurements to test the interferometer . . . . .</b>	<b>64</b>
<b>4.3</b>	<b>Measurements of vibrational modes of the membrane . . . . .</b>	<b>65</b>
4.3.1	First attempts with a damaged membrane . . . . .	65
4.3.2	The hypertensive version of the final membrane . . . . .	67
4.3.3	The final version of the membrane . . . . .	69
<b>4.4</b>	<b>Reference measurements in a cryogenic ion trap . . . . .</b>	<b>74</b>
<b>4.5</b>	<b>Current state of the membrane ion trap and future measurements . . . . .</b>	<b>76</b>
4.5.1	Beyond the Lamb Dicke regime . . . . .	79
4.5.2	Alternative detection methods . . . . .	82

---

In this chapter numerical simulations, as well as the experimental results are discussed. At first we study the results of the simulations of the potentials and the trajectories for the membrane trap. Then the results of the vibrations measurements with the interferometer are presented and we discuss a sideband spectrum, taken in a different trap as a reference for the membrane trap. At last, the current state of the membrane trap is described and we give an outlook on future measurements.

## 4. NUMERICAL SIMULATIONS AND EXPERIMENTAL RESULTS

### 4.1 Simulating the membrane ion trap

The membrane ion trap is essentially a ring Paul trap. The discussion of the Paul trap (see sec. 2.2.1) gave us the theoretical foundation to understand the principal of operation of the general ion trap. The simulations of the membrane ion trap are based on these foundations, allowing us to analyze the behavior of the ion in the membrane trap. By simulating potentials and trajectories it is possible to study the stability regions and calculate trap frequencies. For the simulations of the experiment a numerical method based on the boundary element method is used [Singer 2010]. In other experiments the simulations have proven to agree with the experiment on a high level. The model of the membrane trap including the dc electrodes, which is used for the simulations is depicted in 4.1.

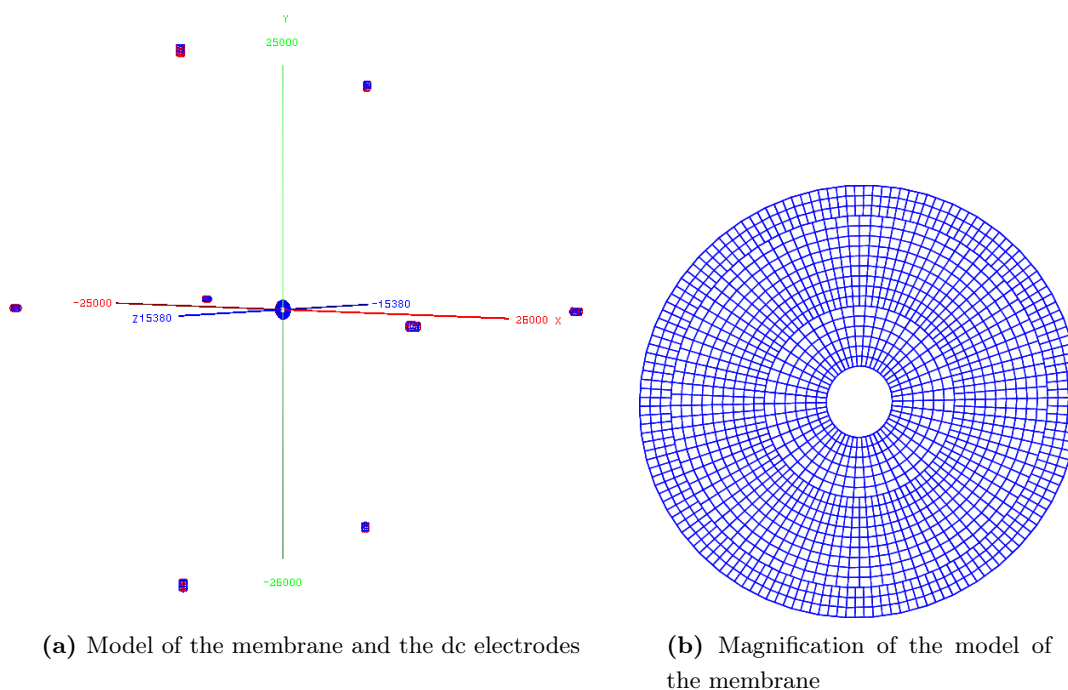


**Figure 4.1: Simulation model for the membrane trap** - For the simulation a model based on the geometrical attributes of the membrane is generated and segmented into a refined mesh. (a) shows the complete model structure used to simulate the membrane trap. The coordinate system shows the orientation of the membrane.  $x$  and  $y$  are the radial axes, and  $z$  is the axial axis. In (b) the magnified membrane model is depicted, showing the refined mesh in detail.

### 4.1.1 Simulations of the ponderomotive potential

At first we take a closer look at the pseudo potentials generated by the membrane trap. The ponderomotive potential can be calculated via the definition from equation (2.10):

$$\phi_{pond} = \frac{Z^2 e^2 |\vec{E}|^2}{4m\Omega_{rf}^2}$$

where the atomic number  $Z$ , the electrical charge  $e$ , the mass  $m$  are well known attributes of the ion. The angular oscillation frequency of the r.f.-field  $\Omega_{rf}$  is chosen to represent the experimental value, leaving the electric field to be calculated by the simulation. The simulation allows to calculate the electric potential  $V_E$  and its numerical derivatives, hence the required electric field is given by  $\vec{E} = -\nabla \cdot V_E$ . In figure 4.2 are the typical radial and axial potentials of the membrane ion trap depicted.

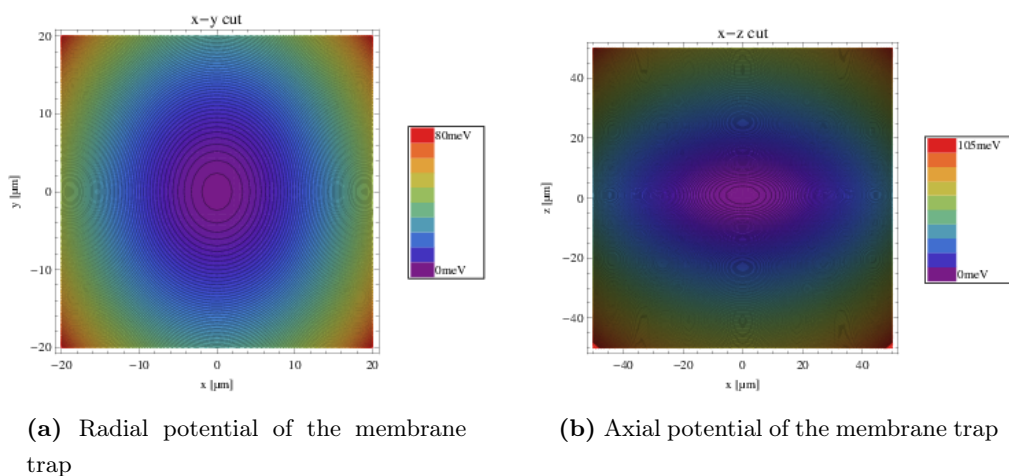


**Figure 4.2: Simulated potentials of the membrane trap** - The general structure of the potentials is similar for all relevant voltages and frequencies.

The potentials were calculated for  $U_{rf} = 400V_{zp}$ ,  $U_{dc} = 0$  and  $\omega_{rf}/2\pi = 30$  MHz. Alternating these parameters does not change the general structure of the potential, but influences the trap frequencies and stability regions, as we will see below. Figure 4.2 shows that it is possible to create a harmonic potential at the center of the trap only using a r.f.-voltage. Therefore, the dc electrodes can be used additionally for the compensation of the micromotion.

## 4. NUMERICAL SIMULATIONS AND EXPERIMENTAL RESULTS

As discussed before, the geometry of the holes of the membrane represents a ring Paul trap, although their shape was chosen to be slightly elliptical. The reason for this choice is illustrated in figure 4.3.

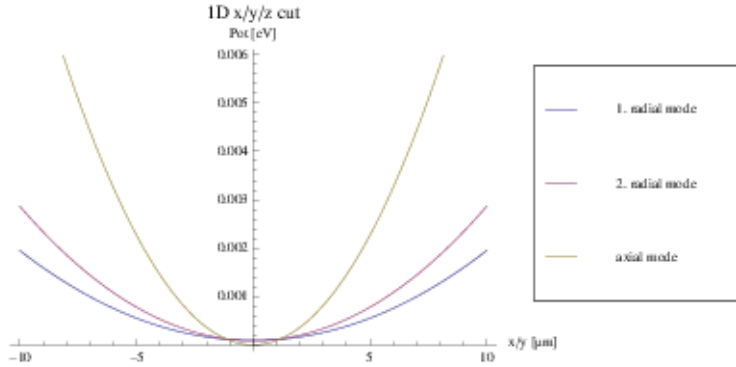


**Figure 4.3: Decoupling of the three modes of the ion** - The elliptical shape of the holes prevents the coupling of the radial modes of the ion. A circular shape would allow the coupling of the radial modes, hence inducing heating effects via energy exchange between the modes.

A circular shape of the holes would allow coupling of the radial modes, hence allowing the exchange of energy. The Doppler cooling efficiency would decrease, since the cooling of the first mode would simultaneously heat the second mode. The choice of the elliptical shape is an easy but effective way to decouple the radial modes.

The data obtained from the simulations of the potentials allows us to calculate the trap frequencies and stability parameters  $q_i$  and  $\beta_i$ . The trap is working without additional dc voltages, i.e., the stability parameter  $a_i$  vanishes from equation (2.15), i.e.,  $a_i = 0$ .

In table 4.1 the results for the trap frequencies and the stability parameters are listed for different trap settings. Stable trap conditions are indicated by  $\beta \ll 1$ . The calculated parameters show a clear trend towards higher r.f.-frequencies and the lower r.f.-voltages.

#### 4.1 Simulating the membrane ion trap

100× 110 μm	$U_{rf} = 300 \text{ V}_{\text{zp}}$ $\omega_{rf}/2\pi = 20 \text{ MHz}$	$U_{rf} = 300 \text{ V}_{\text{zp}}$ $\omega_{rf}/2\pi = 30 \text{ MHz}$	$U_{rf} = 400 \text{ V}_{\text{zp}}$ $\omega_{rf}/2\pi = 20 \text{ MHz}$	$U_{rf} = 400 \text{ V}_{\text{zp}}$ $\omega_{rf}/2\pi = 30 \text{ MHz}$
$f_x$	2.8	1.8	3.7	2.5
$f_y$	2.3	1.5	3.1	2.0
$f_z$	5.7	3.4	8.7	4.6
$q_x$	0.39	0.17	0.52	0.23
$q_y$	0.32	0.14	0.42	0.19
$q_z$	0.71	0.31	0.94	0.42
$\beta_x$	0.28	0.12	0.39	0.16
$\beta_y$	0.23	0.10	0.31	0.13
$\beta_z$	0.57	0.22	0.87	0.31

150× 165 μm	$U_{rf} = 300 \text{ V}_{\text{zp}}$ $\omega_{rf}/2\pi = 20 \text{ MHz}$	$U_{rf} = 300 \text{ V}_{\text{zp}}$ $\omega_{rf}/2\pi = 30 \text{ MHz}$	$U_{rf} = 400 \text{ V}_{\text{zp}}$ $\omega_{rf}/2\pi = 20 \text{ MHz}$	$U_{rf} = 400 \text{ V}_{\text{zp}}$ $\omega_{rf}/2\pi = 30 \text{ MHz}$
$f_x$	1.8	1.2	2.4	1.6
$f_y$	1.5	1.0	2.0	1.3
$f_z$	3.5	2.2	4.9	3.0
$q_x$	0.26	0.11	0.34	0.15
$q_y$	0.21	0.09	0.28	0.13
$q_z$	0.47	0.21	0.63	0.28
$\beta_x$	0.18	0.08	0.25	0.11
$\beta_y$	0.15	0.06	0.20	0.09
$\beta_z$	0.35	0.15	0.49	0.20

**Table 4.1: Trap parameters** - For both trap sizes the stability parameters indicate better stability for higher r.f.-frequencies. For the same r.f.-frequency a voltage of  $U_{rf} = 300 \text{ V}_{\text{zp}}$  shows smaller stability parameters.

## 4. NUMERICAL SIMULATIONS AND EXPERIMENTAL RESULTS

### 4.1.2 Simulations of the trajectory of the ion

Another approach is to use the field simulation to calculate the trajectory of the ion. The electrostatic potentials are used to simulate the trajectories of ions inside a dynamic trapping potential. One can choose from two methods to simulate the ion propagation, i.e. the Euler method or the Störmer-Verlet method. For the simulations presented here we used the Störmer-Verlet method, which proved to be the more accurate one for the ion simulation [Singer 2010]. The simulations of the ion trajectory provide an simple way to determine stability diagrams, as well as a second method to calculate the trap frequencies.

A stable trajectory is confined to a small region around the center of the trap, while an unstable trajectory leads out of the trap. An example of a stable trajectory and an unstable trajectory is plotted in figure 4.4.

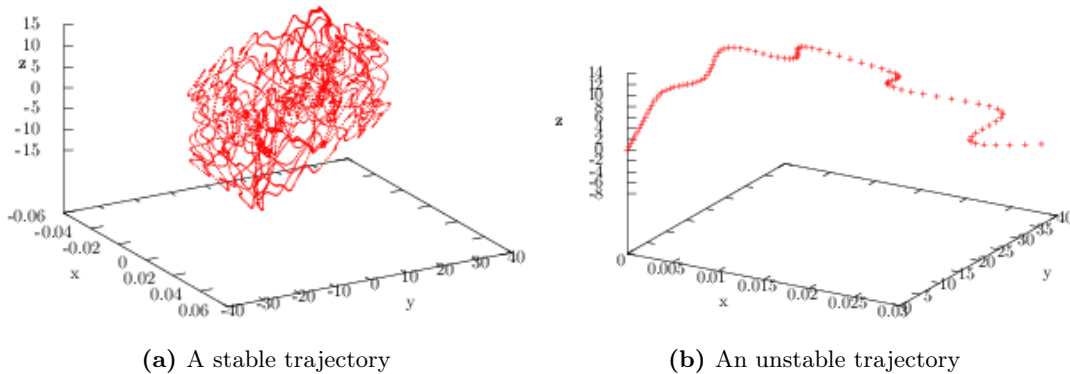


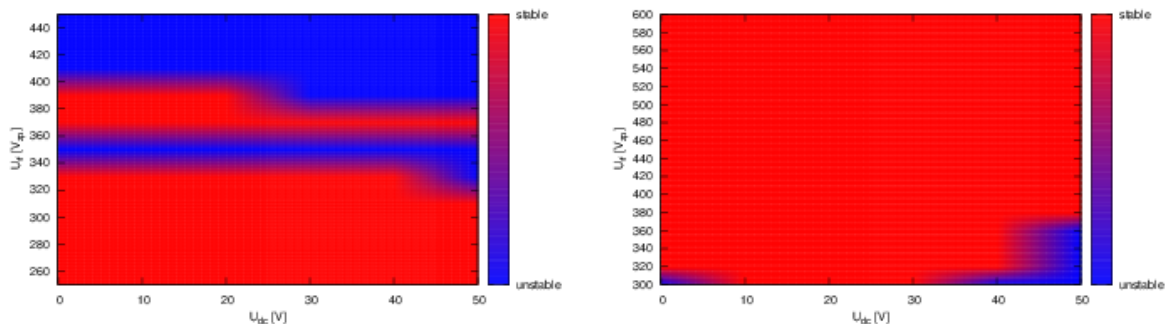
**Figure 4.4: Simulated trajectories of the ion** - The stable trajectory (a) is confined to a region around the trap center, while the unstable trajectory (b) leaves the trapping region after a short period of time. All values are expressed in  $\mu\text{m}$ .

The trajectory of the ion starts at the origin of the trap ( $x = y = z = 0$ ). The initial velocity was calculated for a thermal atom beam by assuming the oven is directed in  $y$ - and  $z$ -direction and perpendicular to the  $x$ -axis, hence the initial velocity has no  $x$ -component. In figure 4.4a the trajectory is confined to the trap region, while the trajectory in figure 4.4b leaves the trap region, after a short period of time. In this example the ion escapes in the  $y$ -direction, which indicates unstable trapping parameters.

By iterating the parameters of  $U_{rf}$  and  $U_{dc}$ , as well as registering the stability of the

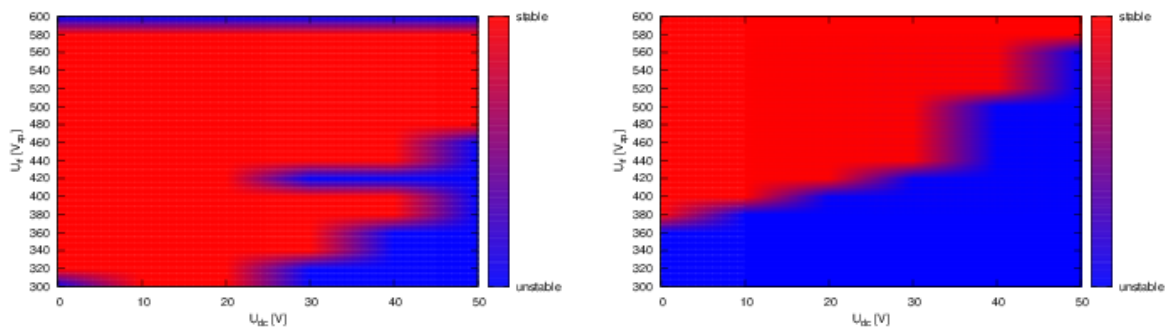
## 4.1 Simulating the membrane ion trap

trajectory, it is possible to derive the stability diagrams for different frequencies and trap sizes. For the analysis of the membrane trap we calculated the stability diagrams for both hole sizes ( $100 \times 110 \mu\text{m}$  and  $150 \times 165 \mu\text{m}$ ), for r.f-frequencies of 20 MHz and 30 MHz iterating  $U_{rf}$  and  $U_{dc}$  in a range that can be realized in the experiment.



(a) Stability diagram for the  $100 \mu\text{m}$  hole and  $\omega_{rf}/2\pi = 20 \text{ MHz}$

(b) Stability diagram for the  $100 \mu\text{m}$  hole and  $\omega_{rf}/2\pi = 30 \text{ MHz}$



(c) Stability diagram for the  $150 \mu\text{m}$  hole and  $\omega_{rf}/2\pi = 20 \text{ MHz}$

(d) Stability diagram for the  $150 \mu\text{m}$  hole and  $\omega_{rf}/2\pi = 30 \text{ MHz}$

**Figure 4.5: Stability diagrams of the membrane trap** - The stability diagrams show stable plateaus for high r.f.-voltages and low dc voltages. In (a) lower voltages were required to display the stability region.

The resulting diagrams are depicted in figure 4.5. The stable regions occur for high values of  $U_{rf}$  and low values of  $U_{dc}$ . Note that only in the case of the  $100 \mu\text{m}$  hole and

#### 4. NUMERICAL SIMULATIONS AND EXPERIMENTAL RESULTS

for a r.f.-frequency of 20 MHz the stability region was found for the lower r.f.-voltages. As mentioned above, for stable trapping conditions no dc voltage is required, but it can prove as a tool to lower the required r.f.-voltage.

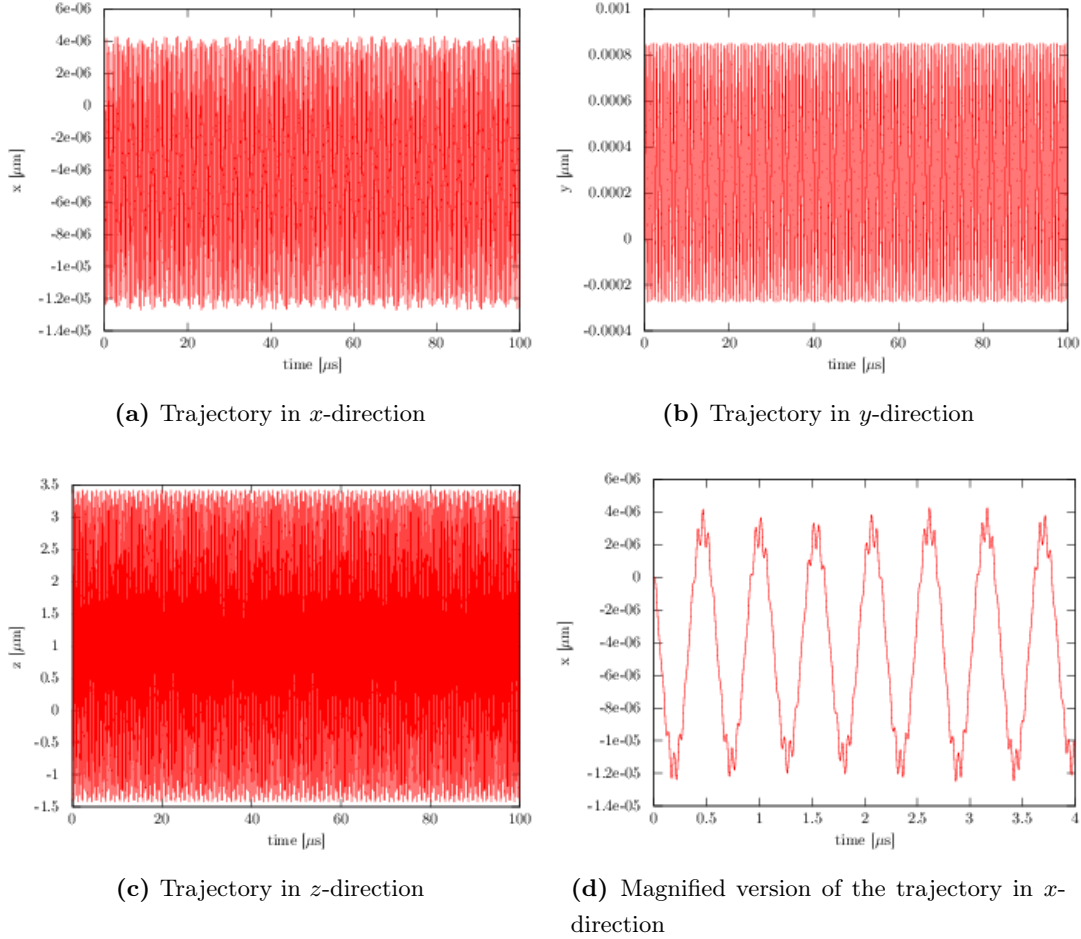


**Figure 4.6: Trajectories for each dimension plotted against time** - The ion oscillates along each axis with the respective trap frequency. The parameters for these example trajectories were  $U_{rf} = 300 V_{zP}$ ,  $U_{dc} = 0 V$ , and  $\omega_{rf}/2\pi = 20 \text{ MHz}$  for a hole size of  $100 \times 110 \mu\text{m}$ . (d) shows a smaller range of the trajectory in  $x$ -direction, making the fast micromotion superimposed on the slower secular motion visible.

## 4.1 Simulating the membrane ion trap

Additionally, it is possible to calculate the trap frequencies using the obtained trajectories using a *Fast Fourier Transformation* (FFT)<sup>1</sup>. Analyzing the trajectory for each dimension ( $x, y, z$ ) transformed to the frequency space via FFT gives us the respective trap frequencies. Figure 4.6 displays the trajectories in  $x$ -,  $y$ -, and  $z$ -direction plotted against the time.

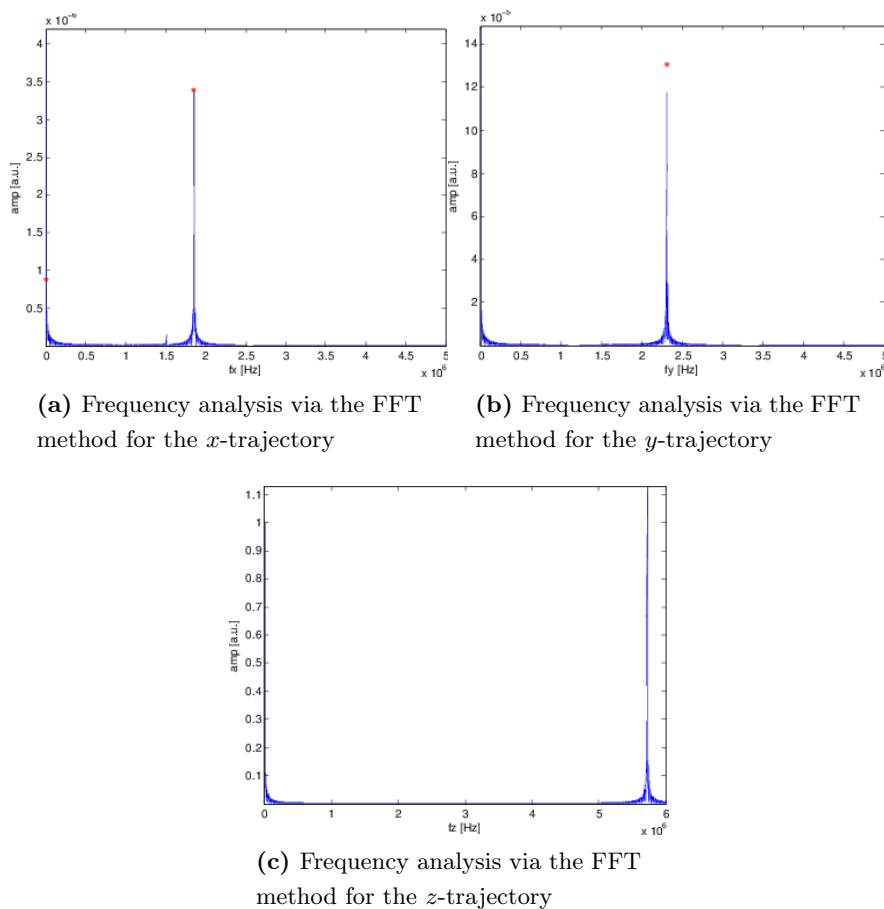


**Figure 4.7: Frequency analysis of the trajectories** - The frequency spectrum for each of the the three dimensions. The resulting frequencies agree perfectly with the ponderomotive potential method.

The FFT is executed using Matlab. An example for the FFT method is depicted in figure 4.7. In each figure the first plot shows the analyzed trajectory, the second plot displays the whole frequency spectrum, and the third plot is a magnified version of the

<sup>1</sup>This method was first implemented by Konstantin Ott.

## 4. NUMERICAL SIMULATIONS AND EXPERIMENTAL RESULTS

---

relevant range of the frequency spectrum.

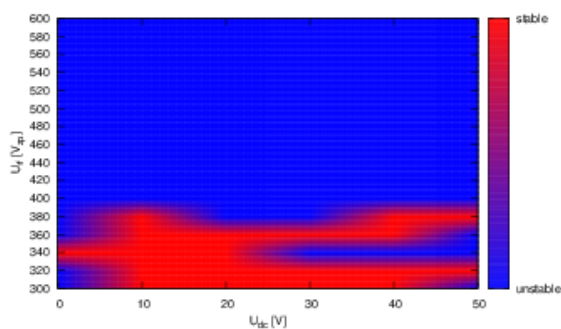
The obtained trap frequencies are listed in table 4.2 and compared to the ones from the potential simulation. We see that the radial and axial trap frequencies agree perfectly for both methods.

Method	Ponderomotive potential	Trajectory
$100\times$	$U_{rf} = 300 V_{zp}$	$U_{rf} = 300 V_{zp}$
$110 \mu\text{m}$	$\omega_{rf}/2\pi = 20 \text{ MHz}$	$\omega_{rf}/2\pi = 20 \text{ MHz}$
$f_x$	2.8	2.8
$f_y$	2.3	2.3
$f_z$	5.7	5.7

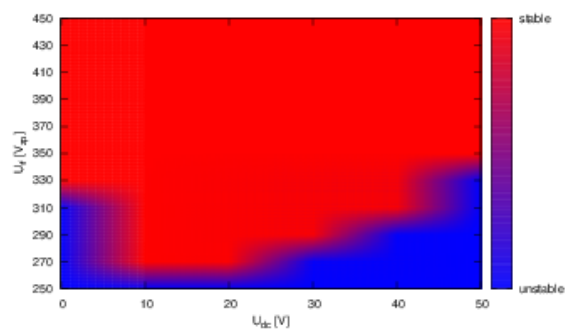
**Table 4.2: Comparison of trap frequencies** - The trap frequencies determined via the potential method and the trajectory method agree well. All frequencies are in MHz

Up to this point, the trajectories were calculated for a non-vibrating membrane. Now we add vibrations with a frequency of  $f_{mem} = 20 \text{ kHz}$  to the simulations and evaluate the stability diagrams and trap frequencies as before. The stability diagrams are displayed in figure 4.8. Overall, the stability regions occur for the same parameters as for the non-vibrating case. Only the simulation of the small hole shows a stability region at the lower r.f.-voltages for the lower r.f.-frequency, while the other stability diagrams indicate stable trapping conditions for the higher r.f.-voltages. In figure 4.8a we increase the range of  $U_{rf}$  to verify that there are no more stable regions found. The comparison with the stability diagrams of the non-vibrating membrane shows that the vibration of the membrane has almost no influence on the stability of the ion trap.

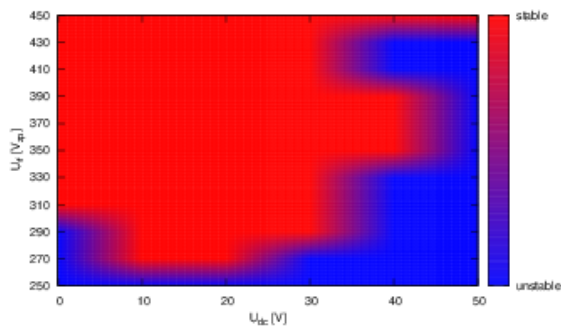
## 4.1 Simulating the membrane ion trap



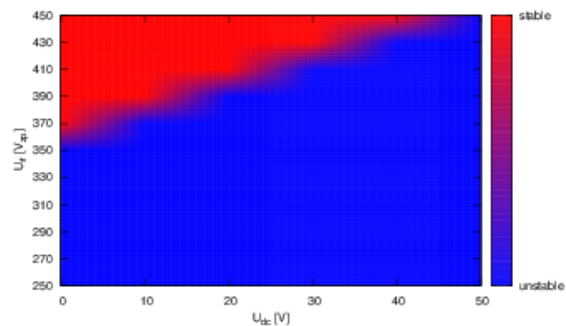
(a) Stability diagram for the 100  $\mu\text{m}$  hole,  $\omega_{rf}/2\pi = 20$  MHz, and  $f_{mem} = 20$  kHz



(b) Stability diagram for the 100  $\mu\text{m}$  hole,  $\omega_{rf}/2\pi = 30$  MHz, and  $f_{mem} = 20$  kHz



(c) Stability diagram for the 150  $\mu\text{m}$  hole,  $\omega_{rf}/2\pi = 20$  MHz, and  $f_{mem} = 20$  kHz



(d) Stability diagram for the 150  $\mu\text{m}$  hole,  $\omega_{rf}/2\pi = 30$  MHz, and  $f_{mem} = 20$  kHz

**Figure 4.8: Stability diagrams of the vibrating membrane trap** - The stability diagrams show similar stable plateaus for high r.f.-voltages and low dc voltages as the ones without vibrations. (a) shows the same behavior as described above. The stability region occurs at the lower r.f.-voltages for the small hole at a r.f.-frequency of 20 MHz. The amplitude for the simulations was set to 10  $\mu\text{m}$ .

## 4. NUMERICAL SIMULATIONS AND EXPERIMENTAL RESULTS

---

The vibration frequencies can be determined in the same way as the trap frequencies, using the FFT method. In figure 4.10 an example is illustrated for the  $z$ -trajectory shown in fig4.9. Since the membrane is vibrating in axial direction, the vibration frequency should show up in the frequency spectrum of the  $z$ -trajectory.

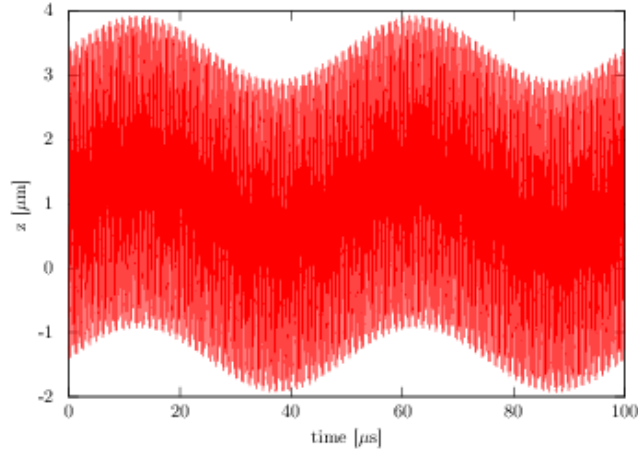
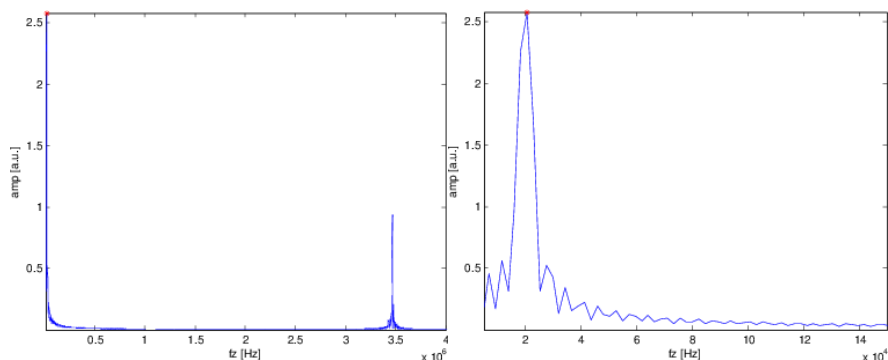


**Figure 4.9: Trajectory in  $z$ -direction for a vibrating membrane** - The trajectory shows a modulation of the  $z$ -trajectory with the membrane oscillation.

On the first look the results of the FFT method show no difference to the results of the non-vibrating membrane. But if we zoom in to the kHz range, the peak of the vibration frequency becomes visible (see fig. 4.10b).

Summarized, the analysis of the potentials showed that it is possible to create a trapping potential only using the r.f.-electrode. The stability diagrams generated via the simulation of the trajectories are showing a tendency towards low dc voltages, which agrees with the result of the potential method, and towards high r.f.-voltages. While it is possible to find stable conditions without dc voltage, the trajectories show that small dc voltages tend to improve the stability, especially for lower r.f.-voltages. Comparing the stability diagrams for a non-vibrating and a vibrating membrane, they show the same tendencies but the stable region of the vibrating membrane decreases slightly. Finally, we have introduced the FFT method, which allows to determine the trap frequencies frequencies from the trajectories. The results are in perfect agreement with the ponderomotive potential method but, additionally, allow to analyze the effect of the vibration on the frequency spectrum. As we have seen, the vibration frequency of

## 4.1 Simulating the membrane ion trap



(a) Frequency analysis via the FFT method for the  $z$ -trajectory of the ion in a vibrating membrane

(b) Zoomed in to the kHz range of the frequency spectrum

**Figure 4.10: Frequency analysis of the trajectory of the ion in a vibrating membrane** - The vibration frequencies appear in the frequency spectrum of the axial direction and can be obtained via the FFT analysis. The parameters for these example trajectories were  $U_{rf} = 300 \text{ V}_{zp}$ ,  $U_{dc} = 0 \text{ V}$ , and  $\omega_{rf}/2\pi = 20 \text{ MHz}$  for a hole size of  $150 \times 165 \mu\text{m}$ .

the membrane oscillating in  $z$ -direction, as well as the effect from additional dc fields, appears in the frequency spectrum of the trajectory in  $z$ -direction.

## 4. NUMERICAL SIMULATIONS AND EXPERIMENTAL RESULTS

### 4.2 Preliminary measurements to test the interferometer

Before we discuss the measurements to determine the vibrational modes of the membrane, we take a closer look at some preliminary measurements. At first, we study a setup with a static mirror instead of the membrane to check if the interferometer is working probably. Instead of a vibrating membrane, we use the compensation piezo actuator to simulate controlled vibrations. In figure 4.11 the interferometer signal, detected via the photo diode, and the excitation signal are displayed. When the piezo actuator is expanding, i.e., during the slope of the excitation sine wave, the displacement of the mirror corresponding to the distance between two adjacent fringes of the same kind is given by  $l = \lambda/2$ . Therefore, the number of fringes  $N$  of the same kind during one vibration cycle is given by

$$N = \frac{4d}{\lambda} \quad (4.1)$$

where  $d$  is the amplitude of the mirror and  $\lambda = 729 \text{ nm}$  is the wavelength of the laser. By counting the fringes, we are able to derive an approximation of the amplitude of the mirror  $d \approx 1.64 \mu\text{m}$  for an excitation frequency  $f = 10 \text{ Hz}$  (see fig. 4.11).

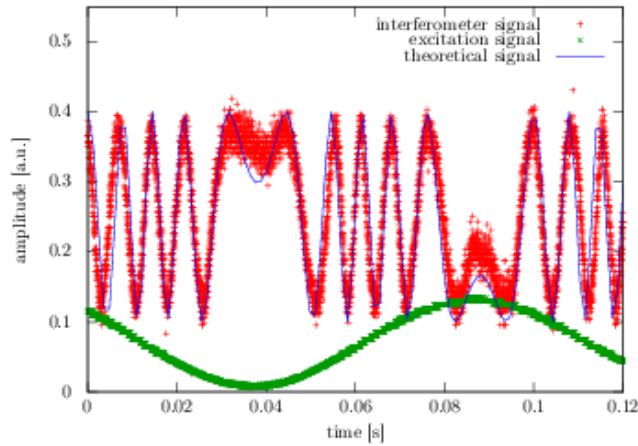


**Figure 4.11: Measurement of the amplitude of a vibrating mirror** - Theoretical photo detector output for a vibration frequency  $f = 10 \text{ Hz}$  fitted to the experiment output signal. The vibration amplitude obtained from the fit results is  $d = 1.76 \mu\text{m}$ .

A theoretical interferometer output, derived from equation 2.69:

$$V(t) = V \cos(\phi_0 + \phi_m \cos(\omega t + \phi_s))$$

### 4.3 Measurements of vibrational modes of the membrane

---

is fitted to the obtained output signal (see fig. 4.11) and agrees well with the experimental results. For the fit only the values of  $\phi_0$ ,  $\phi_m$ , and  $\phi_s$  were varied. Using the fit result for  $\phi_m = 2\pi d/\lambda$ , we can derive a new value for the amplitude of the mirror  $d = 1.76 \mu\text{m}$ , which agrees with the approximated value from before.

Further measurements characterizing the dynamic behavior of the piezo amplifier and the stabilization circuit can be found in the appendix (see sec. A.3 and sec. A.2).

### 4.3 Measurements of vibrational modes of the membrane

---

In this section the measurement results of the vibrational modes of three different versions of the membrane are compared to the respective theoretical values and to each other.

#### 4.3.1 First attempts with a damaged membrane

The first tests of the interferometer and the first measurements of resonance frequencies and quality factors were carried out with a damaged membrane.

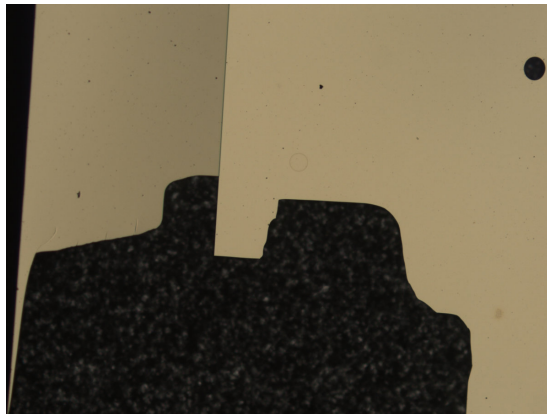


**Figure 4.12: Magnification of the damaged membrane** - In this magnification of the damaged membrane the hole and the start of the fissure are visible. In the upper right corner the unharmed trap hole can be seen.

This damaged version had a hole at one edge of the membrane and some minor fissures. The connection to the r.f.-wire was still intact and the actual trapping hole was un-

## 4. NUMERICAL SIMULATIONS AND EXPERIMENTAL RESULTS

---

harmed. It was used for testing purposes until we replaced it with a new version of the membrane.

In this first setup, the measurements taken have a more qualitative value and should be regarded as test measurements, but are still interesting in comparison to the final version of the membrane.

For the damaged membrane we found only one resonance frequency at  $f_{res} = 21.207$  kHz. In figure 4.13 the resonance peak is displayed. We fitted a Lorentzian function to determine the quality factor of  $Q = 1756$ . For the damaged membrane a low quality factor is reasonable.

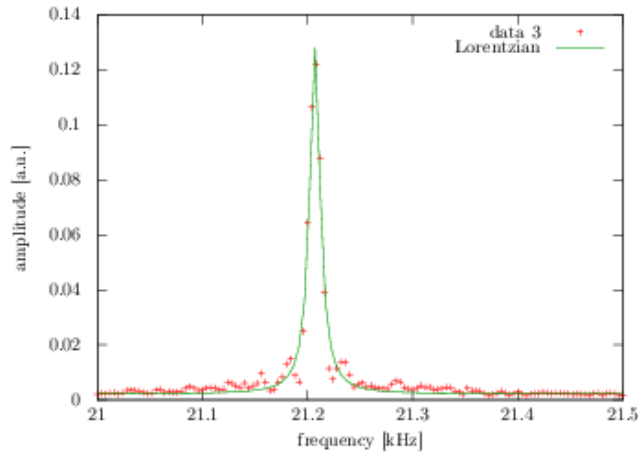


**Figure 4.13: Resonance frequency of the damaged membrane** - The resonance frequency of the damaged membrane was obtained using a spectrum analyzer connected to the interferometer setup. The Lorentzian fit gives us the FWHM  $\sigma$  and via  $Q = \frac{f_{res}}{\sigma}$  the quality factor  $Q = 1756$  was determined.

Another approach to determine the quality factor of the damaged membrane via a ring-down measurement showed the expected behavior of the membrane signal, but gave no quantitative results. In figure 4.14 the data taken from this measurement is shown. After the excitation pulse the amplitude of the interferometer signal decreases over time. It was not possible to determine a quality factor from this signal without sufficient stabilization.

### 4.3 Measurements of vibrational modes of the membrane

---

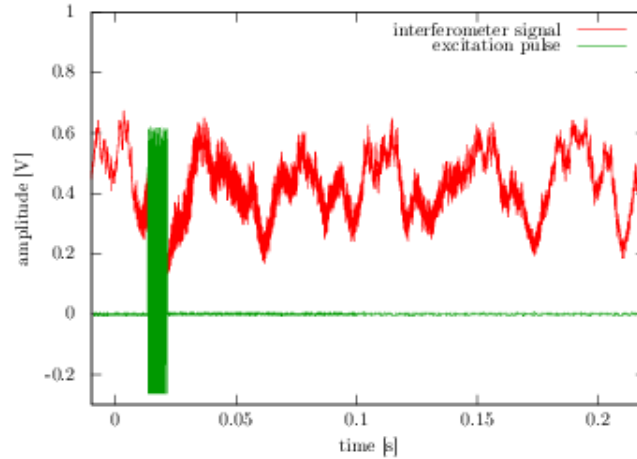


**Figure 4.14: Ring-down measurement of the damaged membrane** - The amplitude of the interferometer signal decreases after the excitation pulse as expected in a ring-down measurement, but without stabilization of the interferometer signal it is not possible to determine the decay time.

#### 4.3.2 The hypertensive version of the final membrane

The final version of the membrane got overstretched during the heat up process. While mounted between the two Marcor pieces, the membrane was stretched, due to thermal expansion, from top to bottom more than from left to right, probably because of differently tight screws. After the heat up process some slight convolutions were visible and suggested an unsymmetrical tension on the membrane. During a second heat up we slightly loosened the screws of the Marcor mount and the membrane returned to its original state. Before restoring the membrane to its original state, we measured the resonance frequencies of the hypertensive version.

For the hypertensive version of the membrane, we used a spectrum analyzer to scan a frequency range and determine the resonance frequencies. In figure 4.15 the resonance spectrum with labeled resonance peaks is displayed. Contrary to the damaged membrane, we found a number of resonance peaks in the range of 50 kHz-100 kHz.

As before, we tried fitting the peaks with Lorentzian functions to determine the quality factor, but because of the interfering of the different peaks with each other no fitting routine seemed to quantify the peaks well enough. So the quality factors for the hyper-

## 4. NUMERICAL SIMULATIONS AND EXPERIMENTAL RESULTS

---

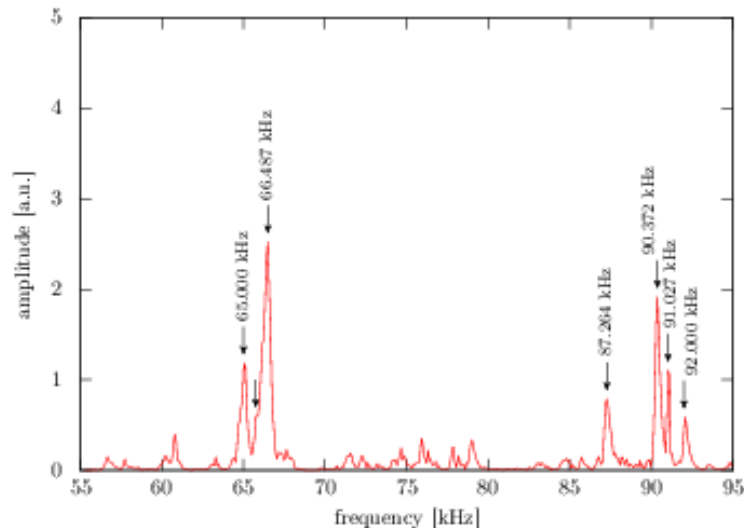


**Figure 4.15: Resonance frequency spectrum of the hypertensive membrane -** The different resonance frequencies are labeled in the plot. We see two regions where resonance peaks occur, one around 65 kHz and one around 90 kHz. The resonance peaks are close enough to interfere with each other.

tensive membrane can only be approximated to be in the range of  $Q \approx 1000-2000$ .

To improve the resonance spectrum, we changed the point of measurement of the interferometer and we compared the measurements of different positions on the membrane. The resonance spectrum changed only in amplitude with the position, but the general distribution of the peaks stayed the same. Moving the measurement point of the membrane always requires a realignment of the interferometer, which most likely caused the different amplitudes. In figure 4.16 the resonance spectra taken in the bottom-left region of the membrane and in the center region are compared. We see that there is no relevant change in the peak distribution.

### 4.3 Measurements of vibrational modes of the membrane

---

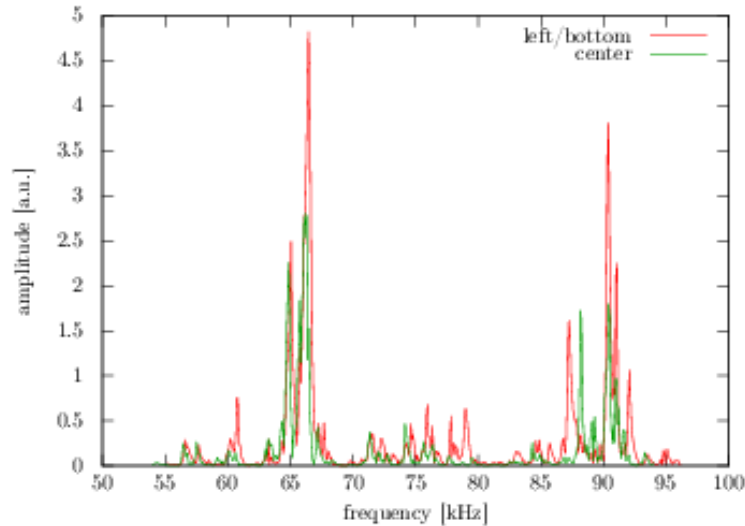


**Figure 4.16: Resonance spectra from two different positions on the membrane -** The distribution of the resonance peaks stayed the same, when changing the measurement point of the interferometer. The amplitude of the peaks changed with the position, probably due to variation of the alignment of the interferometer.

#### 4.3.3 The final version of the membrane

After loosening the screws of the mount, the membrane returned to its original state and the resonance spectrum changed slightly compared to the hypertensive membrane. While we found the same regions of resonance as before, some new resonance peaks occurred at lower frequencies. The range of the resonance spectrum increased to 10 kHz-100 kHz. In figure 4.17 the resonance spectrum is displayed.

Compared to the resonance spectrum of the hypertensive membrane, new resonance frequencies were detected at the lower kHz-range, while for the resonance peaks in the 60 kHz to 90 kHz the spectrum has changed only slightly. It was not possible to verify if the peaks of the hypertensive membrane shifted or disappeared. In figure 4.18 both resonance spectra are plotted.

For the determination of the quality factors of the final version of the membrane, we implemented a new detection scheme for ring-down measurements. Contrary to the detection via oscilloscope, as seen for the damaged membrane, we used the spectrum

#### 4. NUMERICAL SIMULATIONS AND EXPERIMENTAL RESULTS

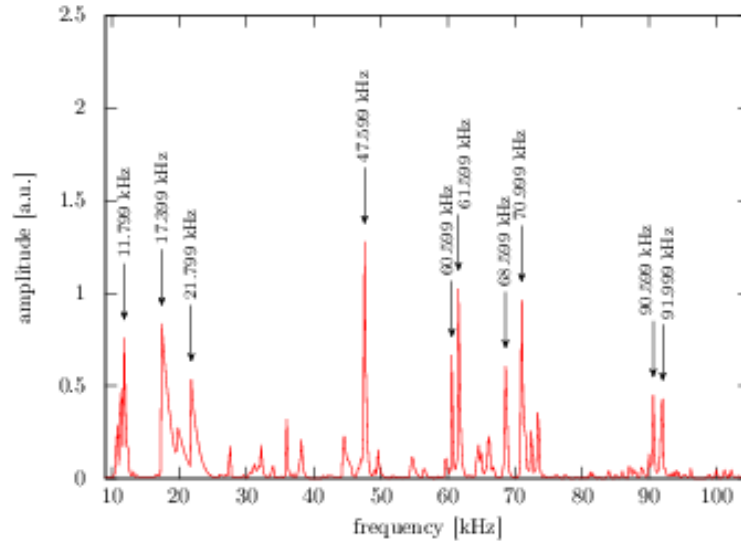


**Figure 4.17: Resonance spectrum of the final version of the membrane** - The resonance spectrum of the membrane was scanned using a spectrum analyzer. This allows to establish an overview of the resonance spectrum. The observed resonance peaks are labeled in the plot.

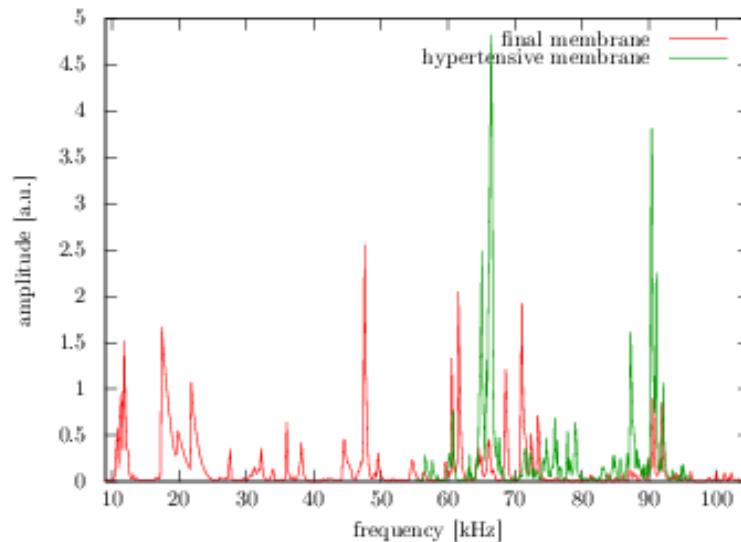


**Figure 4.18: Resonance spectra of the final version and the hypertensive version of the membrane** - In addition to the resonance frequencies of the hypertensive membrane, new resonance peaks were detected for the final membrane around 20 kHz.

### 4.3 Measurements of vibrational modes of the membrane

---

analyzer to detect the ring-down of a specific resonance frequency. This approach allowed an accurate detection of the quality factors, and a benefit of this method is the precise verification of the known resonance frequencies. In table 4.3 the resonance frequencies of the final version of the membrane are listed with their respective quality factors.

$f_{res}$ [kHz]	$\tau$ [s]	$Q$
11.868	0.048	1793
17.424	0.329	18003
19.743	0.377	23369
21.888	0.216	14860
36.005	0.044	4994
47.576	0.039	5864
60.595	0.029	5493
61.646	0.038	7318
68.597	0.036	7681
71.094	0.009	1906
73.463	0.022	5181
90.572	0.018	5140
91.855	0.013	3829

**Table 4.3: Quality factors of the final version of the membrane** - The quality factors for the intact membrane for all resonance frequencies derived via ring-down measurements

An example of a ring-down measurement is depicted in figure 4.19. The amplitude of the vibration decays exponentially. The quality factor is determined using an exponential fit

$$A(t) = A_0 e^{-t/\tau} \tag{4.2}$$

where  $A_0$  is the maximal amplitude and the quality factor is given by  $Q = \pi f_{res} \tau$ .

Comparing the obtained quality factors, leads to the conclusion, that the three frequencies with high  $Q$  values are resonance frequencies low modes of the membrane, while the rest of the frequencies are resonances of higher modes or the frame. To verify this explanation, we calculated the theoretical values of the resonance frequencies of different

## 4. NUMERICAL SIMULATIONS AND EXPERIMENTAL RESULTS

---

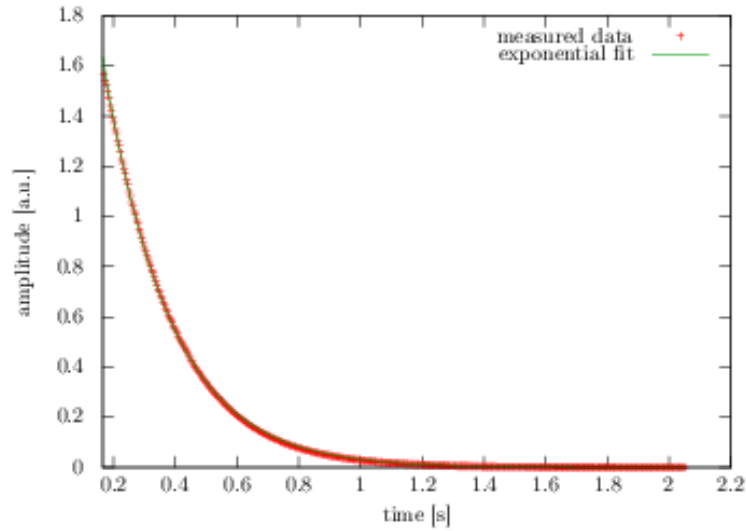


**Figure 4.19: A ring-down measurement at  $f_{res} = 21.888$  kHz** - The ring-down measurement of the vibration amplitude at  $f_{res} = 21.888$  kHz. The quality factor is determined via an exponential fit.

vibrational modes using the formula found in sec. 2.4.1:

$$f(m, n) = \frac{1}{2\pi} \sqrt{\frac{S\pi^2}{\rho h} \left( \frac{m^2}{a^2} + \frac{n^2}{b^2} \right)} \quad (4.3)$$

The results are listed in table 4.4.

### 4.3 Measurements of vibrational modes of the membrane

---

mode	$f_{theo}$ [kHz]	$f_{theo}$ [kHz]	$f_{theo}$ [kHz]
(1,1)	21.888	17.424	19.743
(2,1)	34.608	27.550	31.216
(2,2)	43.776	34.848	39.486
(3,1)	48.943	38.961	44.147
(3,2)	55.804	44.423	50.335
(3,3)	65.664	52.272	59.229
(4,1)	63.814	50.799	57.560
(4,2)	69.216	55.100	62.433
(4,3)	77.386	61.603	69.802
(4,4)	87.552	69.696	78.972
(5,1)	78.918	62.823	71.184
(5,2)	83.347	66.349	75.179
(5,3)	90.247	71.841	81.403
(5,4)	99.102	78.891	89.390
(5,5)	109.440	87.120	98.715

**Table 4.4: Theoretical vibration frequencies** - For the calculation of the resonance frequencies, we used the following values:  $a = b = 4.8$  mm,  $h = 2.0$   $\mu$ m,  $\rho = 3909$  kg/m<sup>3</sup>, while varying  $S$  to adjust the resonance frequency of the (1,1) mode (see eq.4.3).

Each of the three resonance frequencies with high  $Q$  value were set to be the (1,1) vibrational mode via adjusting the stress  $S$ . Compared with the results obtained via the ring-down measurement (see tab. 4.3) we can find matching results for each of the three possibilities, but neither of them can be consider to match for all vibrational modes. A more complex theoretical simulation of the membrane might be necessary to explain these results. Interference effects should be considered as well. Note that the resonance at  $f_{res} = 19.743$  kHz is only visible as a small peak, which was not considered a resonance peak in the first general analysis. The lowest frequency found, i.e.,  $f_{res} = 11.868$  kHz, might be a resonance of the frame.

## 4. NUMERICAL SIMULATIONS AND EXPERIMENTAL RESULTS

### 4.4 Reference measurements in a cryogenic ion trap

The observable spectrum of the motional sidebands depends, among other aspects, on the experimental setup. While the motional frequencies are primarily defined by the ion, used for the experiment, and the trapping potential, the observable frequencies depend on the spectroscopy laser alignment. Using the same ion and assuming similar trapping potentials, the observed sideband spectrum may vary according to the direction of the laser beam, compared to the magnetic field, and its polarization. As described before, only the Zeeman subtransitions with a projection to the lasers  $k$ -vector will be seen by the laser, hence can be observed depending on the alignment.

For comparison with the membrane trap, we chose a cryogenic ion trap as reference trap. The cryogenic ion trap is a micro ion trap (see ref. [Poschinger 2010b]) in a cryogenic setup. The reasons to use this trap for reference measurements were mainly the similar axial and radial trap frequencies.

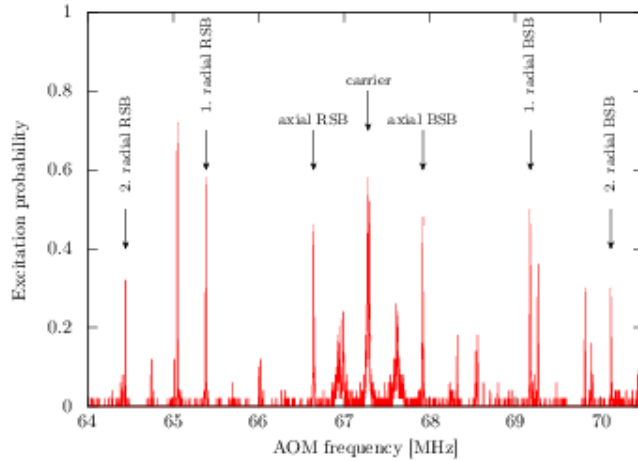


**Figure 4.20: Sideband spectrum of the cryogenic microtrap** - Around the centered carrier frequency, the axial and radial motional sidebands are evenly distributed. In the experiment, it is useful to measure the easy accessible AOM frequency and calculating the motional frequencies in relation to the carrier frequency. The axial frequency is  $f_{ax} = 1.28$  MHz, the first radial frequency is  $f_{rad1} = 1.90$  MHz and the second radial frequency is  $f_{rad2} = 2.84$  MHz

The sideband spectrum in figure 4.20 was measured at a Temperature  $T = 220$  K. Due

#### 4.4 Reference measurements in a cryogenic ion trap

to a different vacuum chamber, the laser beams access the trapping region from different directions. In the cryogenic ion trap the trap axis is tilted  $45^\circ$  to the spectroscopy laser and has projection to all motional modes, i.e. the axial and both radial modes are visible in the spectrum. The obtained sideband spectrum shows the carrier frequency in the center with the highest excitation probability. Around the carrier frequency the red and blue sidebands are equidistantly distributed. In the experiment, it is reasonable to measure the well known AOM frequency and calculate the motional frequencies relative to the carrier frequency.

For studying the dynamic behavior of the sideband transitions, we measure the excitation probability while varying the pulse length. Depending on the time the laser beam is applied to the ion, the probability for the ion being in the excited or in the ground state oscillates with the Rabi frequency. As shown in figure 4.21, on the carrier transition the probability oscillates between 0 and 1, decreasing over time due to heating and other interfering effects. The red and blue sidebands saturate at a probability of 0.5 and have different Rabi frequencies for a thermal harmonic oscillator state [Poschinger 2010b].

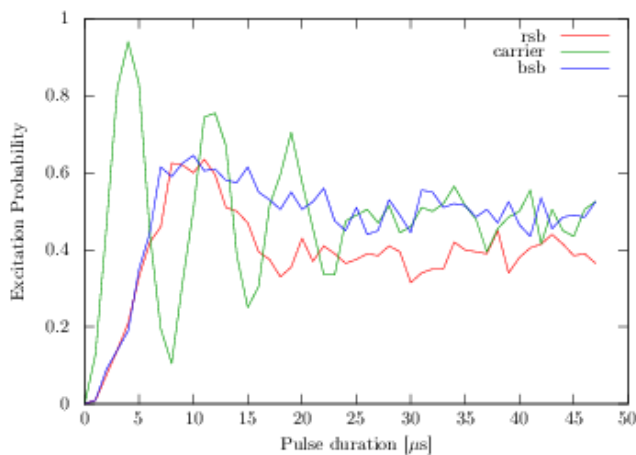


**Figure 4.21: Rabi oscillations in the cryogenic microtrap** - For different pulse lengths, the probability of the transitions varies. While the carrier transition oscillates with a Rabi frequency of  $\Omega \approx 110$  kHz, the red and blue sideband saturate at probability of 0.5.

### 4.5 Current state of the membrane ion trap and future measurements

---

In the last year, the project *membrane ion trap* developed constantly to reach its current state. The basic idea of an oscillating ion trap started with an empty table and became a set up experiment. Unfortunately, up to this point there are no ions in the membrane trap, but we are confident to solve all remaining minor issues in the near future. Here we present the current state of the membrane trap and given an outlook on future measurements.

Up to this point, all preliminary steps to trap an ion were successful and almost all required conditions are fulfilled. In a first approach, the pressure in the vacuum chamber was a limiting factor. With the additional Titan sublimation pump we solved this issue and reached a pressure in the range of  $10^{-9}$  -  $10^{-10}$  mbar, which is typical for most ion traps. The vaporizing oven is producing a neutral atom beam, which was observed with two detection methods.

Firstly, we aligned the photo ionization laser in front of the tip of the oven and detected the neutral atom fluorescence with an infrared camera. The fluorescing atoms along the laser beam are shown in figure 4.22.

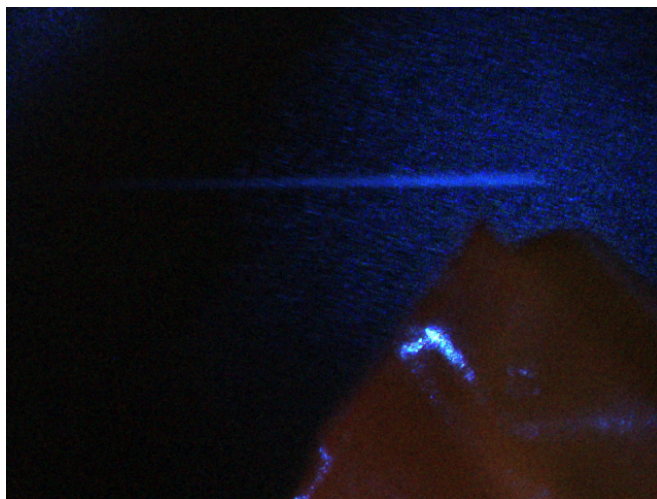


**Figure 4.22: Fluorescence of the neutral atom beam detected via an infrared camera** - In front of the magnified oven tip the fluorescence of the neutral atoms along the laser beam stands out clearly against the background.

## 4.5 Current state of the membrane ion trap and future measurements

Secondly, we verified that the neutral atom beam reaches the trapping region. Therefore, we aligned the photo ionization laser through one of the  $150\ \mu\text{m}$  holes of the membrane and detected the fluorescence of the neutral atoms with the detection apparatus, i.e., the EMCCD camera. This method also provides the precise wavelength of the photo ionization laser to ionize at the trapping region. In figure 4.23 the signal of the EMCCD camera is displayed. By scanning the wavelength of the photo ionization laser in an so called symmetrical saw tooth shape, the camera signal shows fluorescence peaks on every rising and falling slope if the wavelength matches.

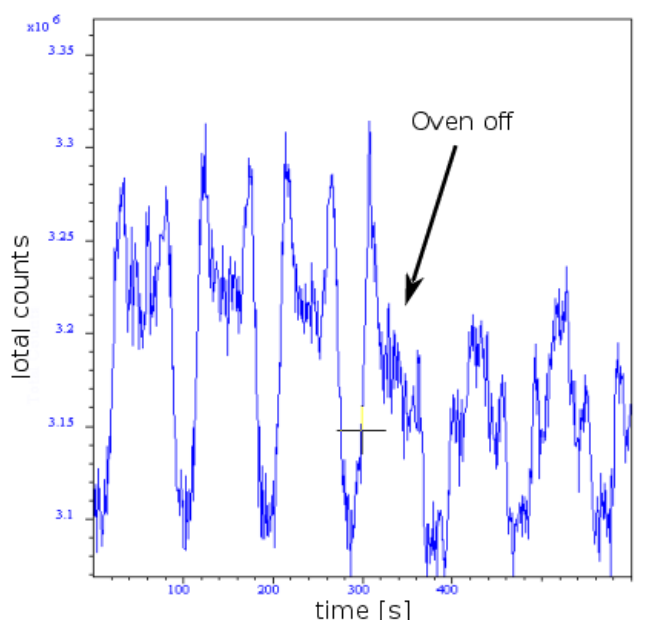


**Figure 4.23: Fluorescence of the neutral atom beam detected at the trapping region via the EMCCD camera** - At the center peak the oven was turned off to verify that the peaks are actually from the atom beam. While the oven is turned on two equidistant fluorescence peaks, one on the rising and one on the falling slope, are clearly visible. After turning off the oven the fluorescence peaks decrease while the oven cools down, until they disappear. The fluctuations of the signal are intensity fluctuations, which arise from the modulation of the laser.

At this point, almost all necessary conditions for trapping ions are fulfilled. There are ions at the trapping region and the ultra-high vacuum minimizes possible scattering at background atoms, which can result in unstable conditions. After aligning all necessary laser beams through the trapping hole, therefore verifying that all beams are aligned

## 4. NUMERICAL SIMULATIONS AND EXPERIMENTAL RESULTS

---

at the trapping region, the final step is to find the right r.f.- and dc voltages to create a trapping potential. From the simulations we know that rather high r.f.-voltages in combination with low compensation dc voltages provide the optimal conditions in theory, but the high r.f.-voltages are rather challenging in the experiment. We had to improve the shielding of the helical resonator to minimize interference with other electrical components in the lab, especially the electrical stabilization components of the laser system. This is still the main issue that needs improvement. A new helical resonator design is currently developed to provide better stability of the r.f.-frequency and it will be integrated in an improved shielding construction.

Another minor issue is stray light of the laser at 397 nm which is diffracted from the trap hole and leads to an interference pattern on the EMCCD-camera. The detection scheme is based on the detection of fluorescence at 397 nm, hence the stray light of the respective laser beam needs to be minimized. This can be achieved via a tight focus and an accurate alignment of the laser beam through the trapping hole. The current state should allow the detection of a trapped ion, but for further improvement of the detection process, a background free detection scheme can easily be implemented in a future setup. A further discussion of the background free detection schemes can be found in section 4.5.2.

For the analysis of future measurements, we simulated a possible sideband spectrum. In the membrane trap the ion acts as a probe for the vibrations of the membrane. We want to observe the vibrational modes of the membrane via sideband spectroscopy. The resonance frequencies of the membrane are in the range of 20 kHz to 100 kHz, while we calculated trap frequencies of a few MHz. This should allow a good discrimination of the different frequencies in the sideband spectrum.

To simulate a possible sideband spectrum, we calculated the Lamb Dicke parameters for the motional frequencies of the ion and the membrane (see table 4.5).

$\eta_x$	$\eta_y$	$\eta_z$	$\eta_{mem20kHz}$	$\eta_{mem100kHz}$
0.21	0.19	0.14	1.72	0.77

**Table 4.5: Lamb Dicke parameters for the trap and membrane frequencies -**

The Lamb Dicke parameters of the radial frequency are given by  $\eta_x$  and  $\eta_y$ ,  $\eta_z$  is the Lamb Dicke parameter of the axial frequency. The Lamb Dicke parameters of the resonance frequencies of the membrane are in the range of  $\eta_{mem20kHz}$  to  $\eta_{mem100kHz}$ .

## 4.5 Current state of the membrane ion trap and future measurements

---

A resolved sideband spectrum is only given in the Lamb Dicke regime, where  $\eta \cdot \sqrt{n} \ll 1$ . Regarding the calculated Lamb Dicke parameters, it is obvious that the vibration of the membrane are outside the Lamb Dicke regime, especially for a thermal distribution of the membrane modes. Hence, it is possible to resolve the motional frequencies of a sufficiently cooled ion ( $n_{th} \approx 20$ ) but we have to discuss the consequence for frequencies outside the Lamb Dicke regime, i.e., for the membrane frequencies.

### 4.5.1 Beyond the Lamb Dicke regime

Assuming a thermal distribution of the membrane modes, we simulate the theoretical sideband spectrum of the membrane frequencies. The thermal probability distribution for finding the ion in the Fock state  $|n\rangle$  is described by

$$p(n) := \frac{(n_{th})^n}{(n_{th} + 1)^{(n+1)}} \quad \text{with} \quad n_{th} = \frac{k_B T}{\hbar \omega} \quad (4.4)$$

where  $n_{th}$  is the mean vibrational quantum number,  $k_B$  the Boltzmann constant and  $\omega$  the respective frequency. Outside the Lamb Dicke regime the excitation probability takes the following form (see sec. 2.3.1)

$$p_e(t) = \sum_n p(n) \sin^2 \left( \frac{1}{2} \Omega_{n,n+s} t \right) \quad (4.5)$$

where the effective Rabi frequencies  $\Omega_{n,n+s}$  are given by

$$\Omega_{n,n+s} = \Omega_0 \cdot M_{n,n+s} \quad (4.6)$$

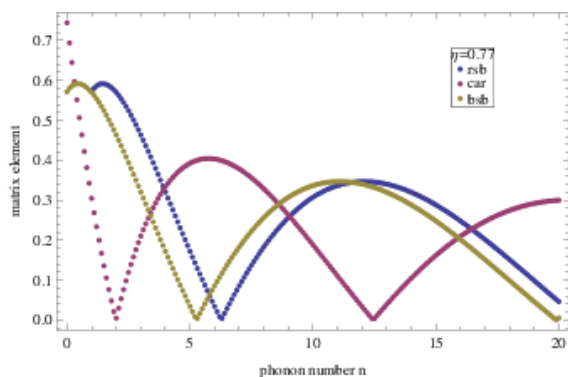
where  $M_{n,n+s}$  are the matrix elements defined in equation 2.36. The matrix elements for carrier, red sideband, blue sideband and membrane frequencies<sup>1</sup> are depicted in figure 4.24.

Finally, for the simulation of a sideband spectrum outside the Lamb Dicke regime we have to plot the sum of the excitation probabilities for all transitions in dependence of the frequency. The results are depicted in figure 4.25.

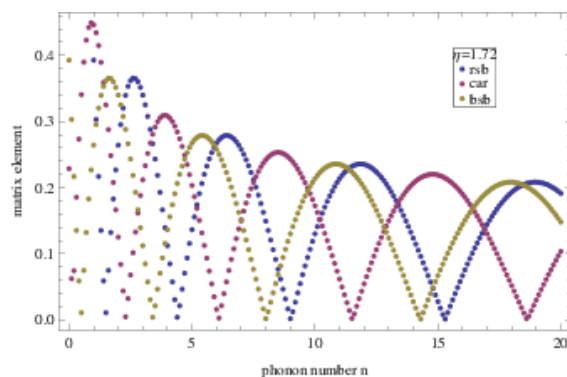
---

<sup>1</sup>We inherit the terminology of the sideband transitions, i.e., carrier, red and blue sideband, for the membrane transitions.

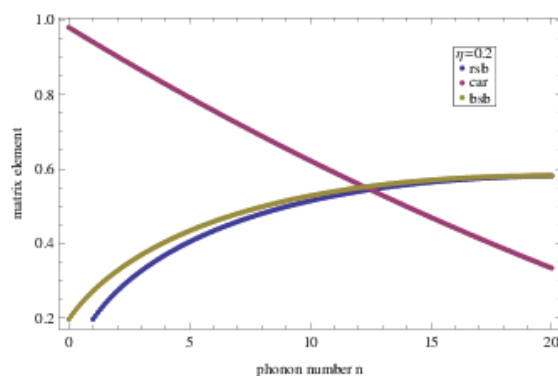
#### 4. NUMERICAL SIMULATIONS AND EXPERIMENTAL RESULTS



(a) Matrix elements for the Lamb Dicke parameter of the upper limit of the membrane resonance frequency



(b) Matrix elements for the Lamb Dicke parameter of the lower limit of the membrane resonance frequency



(c) Matrix elements for a typical Lamb Dicke parameter of the ion

**Figure 4.24: Matrix elements for different Lamb Dicke parameters  $\eta$**  - (a) and (b) shows the matrix elements for high Lamb Dicke parameters as calculated for the membrane. Compared with the matrix elements for typical Lamb Dicke parameters of the ion (c) the oscillation of the matrix elements in (a) and (b) are faster, hence the regions, where the carrier transition is stronger than the sidebands, are smaller.

## 4.5 Current state of the membrane ion trap and future measurements

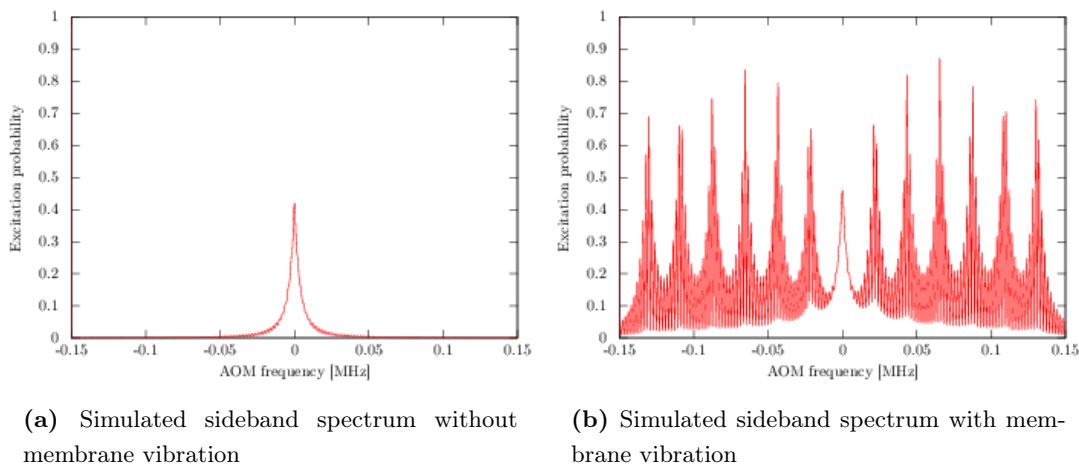


**Figure 4.25: Simulation of sideband spectra** - Simulation of the sideband spectrum for a motional trap frequency of 3 MHz and a membrane resonance frequency of 21.8 kHz compared to a sideband spectrum without membrane vibration.

For simplicities sake only one ion transition and only one membrane frequency are depicted in figure 4.25. In figure 4.25a the sideband spectrum without membrane vibration is depicted, and figure 4.25b shows the sideband spectrum with membrane vibration. A similar spectrum is expected for each of the motional sideband peaks of the ion.

Furthermore, we calculated the Rabi oscillations for a thermal distribution. The excitation probability as given by equation (4.5) plotted against the time is illustrated in figure 4.26. For  $n_{th} = 1$  the matrix element of the carrier transition is greater than the one of the sideband transitions, but for  $n_{th} = 20$  the sideband transitions are the preferred transition (see fig. 4.24c).

After trapping ions the first task will be to prepare the experiment for measuring a sideband spectrum. At first it is reasonable to start without excitation of the membrane and to accurately determine the trap frequencies. Afterwards, it will be interesting to observe the sideband spectrum when the membrane vibrations are excited. For the excitation we can use the piezo actuator mounted on the vacuum chamber or light forces by using a pulsed laser beam directed on the membrane surface. The obtained results for the resonance frequencies compared with the data collected by the interferometer will give a value for the accurateness of the ion as a probe. Furthermore, the sideband

## 4. NUMERICAL SIMULATIONS AND EXPERIMENTAL RESULTS

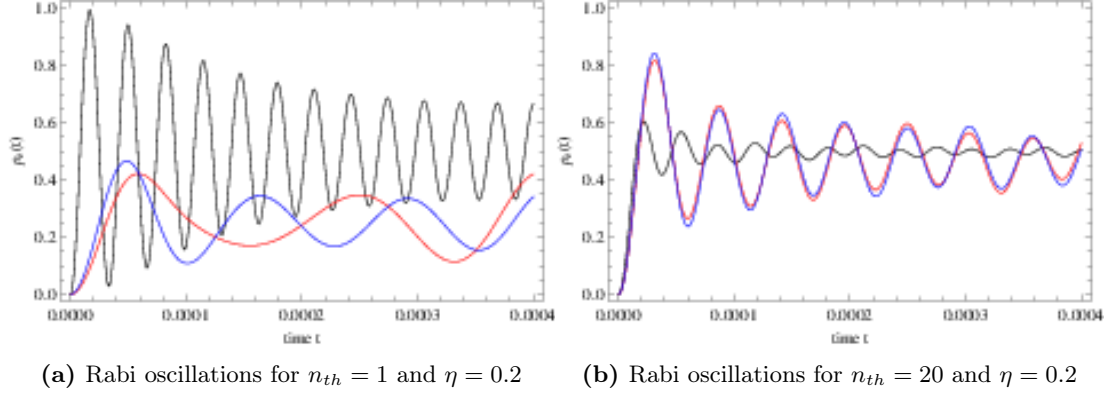


**Figure 4.26: Simulations of Rabi oscillations for a thermal probability distribution** - The red and blue curves represent the red and blue sideband, respectively, the black curve shows the carrier oscillations. For low mean phonon numbers  $n_{th}$  the carrier oscillates between 0 and 1 while the sidebands oscillate around 0.5. For higher mean phonon numbers the behavior of carrier and sidebands is inverted.

spectrum observed after a short excitation pulse can provide the possibility to measure the quality factor using the ion. Analogue to the ring-down measurements detected with the interferometer, a ring-down measurement with the ion as probe is possible. These are some of the possible examples for measurements using the ion as a probe, which all can be verified and compared with the well understood interferometry technique.

### 4.5.2 Alternative detection methods

Instead of using the transition  $S_{1/2}-P_{1/2}$  at 397 nm it is possible to include the transition  $S_{1/2}-P_{3/2}$  at 393 nm into the detection process. Utilizing a filter, which cuts off only one of the wavelengths, a background free detection scheme can be accomplished. This first possibility uses the laser at 397 nm to excite the ion to the  $P_{1/2}$  state, then using lasers at 866 nm and 850 nm to end up in the  $P_{3/2}$  state via the  $D_{3/2}$  state. The ion decays to the ground state via emitting light at 393 nm, which we can detect (see fig. 4.27a). Since we currently use a filter with transmission at 397 nm, for this detection scheme an exchange of the filter would be necessary.

Fortunately, the second possibility is mainly the reversed way and hence possible with our current filter. We can use the laser at 393 nm to excite the ion to the  $P_{3/2}$  state

## 4.5 Current state of the membrane ion trap and future measurements

and by shining in lasers at 850 nm and 866 nm the ion ends up in the  $P_{1/2}$  state, which decays to the ground state. The fluorescence at 397 nm can then be detected using our current filter (see fig. 4.27a). Since we have a laser at 393 nm at our disposal, this background free detection scheme can be set up simply by coupling this laser into the fiber currently used for the laser beam at 397 nm.

A completely different approach for a background free detection scheme, is to use the quadrupole transition at 729 nm and a laser at 854 nm to excite the ion to the  $P_{3/2}$ . This allows the detection of the ion via fluorescence at 393 nm, but makes the  $D_{5/2}$  state unavailable for using it as the dark state (see fig. 4.27b).

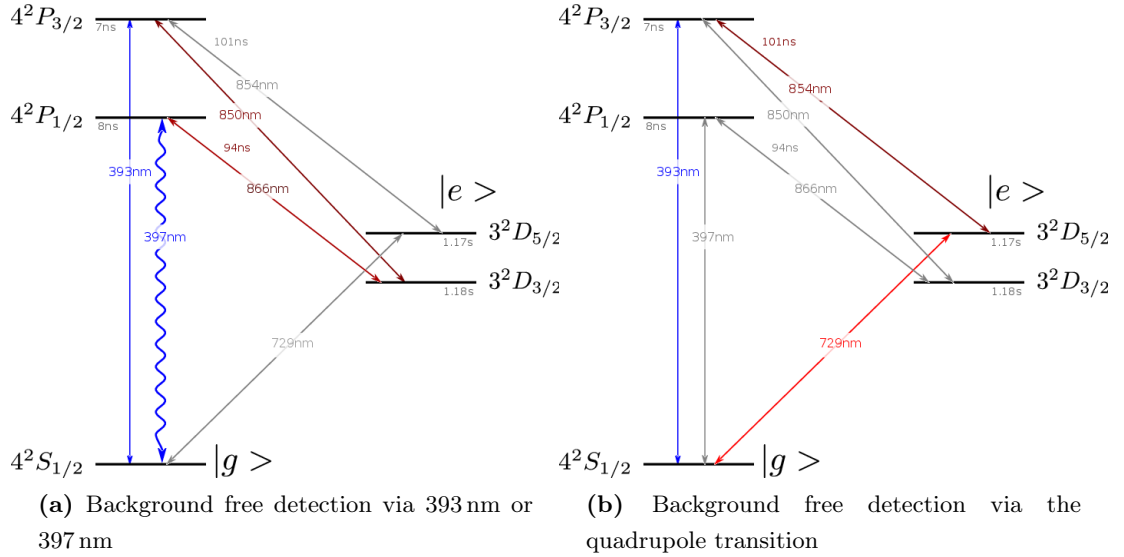


**Figure 4.27: Background free detection schemes** - (a) illustrates the second possibility of a background free detection, but the opposite way is also possible, and (b) illustrates the third method via the quadrupole transition.

## **4. NUMERICAL SIMULATIONS AND EXPERIMENTAL RESULTS**

# 5

## Discussion

In this thesis, we have laid the theoretical foundations for empirical work with oscillating ion traps. We have described the preparation of a membrane as an ion trap which combines the properties of a mechanical oscillator with a reliable quantum mechanical system. We have provided the necessary steps to achieve the trapping of an ion. These include the development and the setup process of the membrane trap and the characterization of the mechanical properties of the membrane. We have performed a numerical analysis of the membrane ion trap and given a theoretical outlook on future measurements. Overall, the project *membrane trap* is on an encouraging way and we are confident to accomplish the trapping of ions in the near future.

The current state of the membrane trap provides the starting point for a promising long-term research project on the coupling of an ion and a membrane. First, it constitutes the basis to investigate the mechanical properties of the trap using the ion as a probe and to gather further experience in our understanding of the coupling of an atomic particle and a micro oscillator. Once the current system is sufficiently understood and its properties well determined, the next step will be analyzing possible coupling schemes and finding appropriate implementations. For instance, one may imagine a cryogenic setup for the membrane trap, exploiting our experience made in the experiment for the reference spectroscopy: the cooling of a membrane to low temperatures allows to reach the strong-coupling regime where the coherent exchange of energy between the ion and the membrane can be observed. Overall, many avenues of future research have the potential to bear inspiring discoveries in our understanding of the boundary between classical and quantum mechanical physics – what’s sure for now is that the future of

## 5. DISCUSSION

---

the membrane ion trap promises to be exciting.

# A

## Appendix

### **A.1 The Stabilization circuit**

---

The stabilization circuit is described in section [3.2.2](#). On the next page, we present a large version of the stabilization circuit diagram for better viewing.

## A. APPENDIX

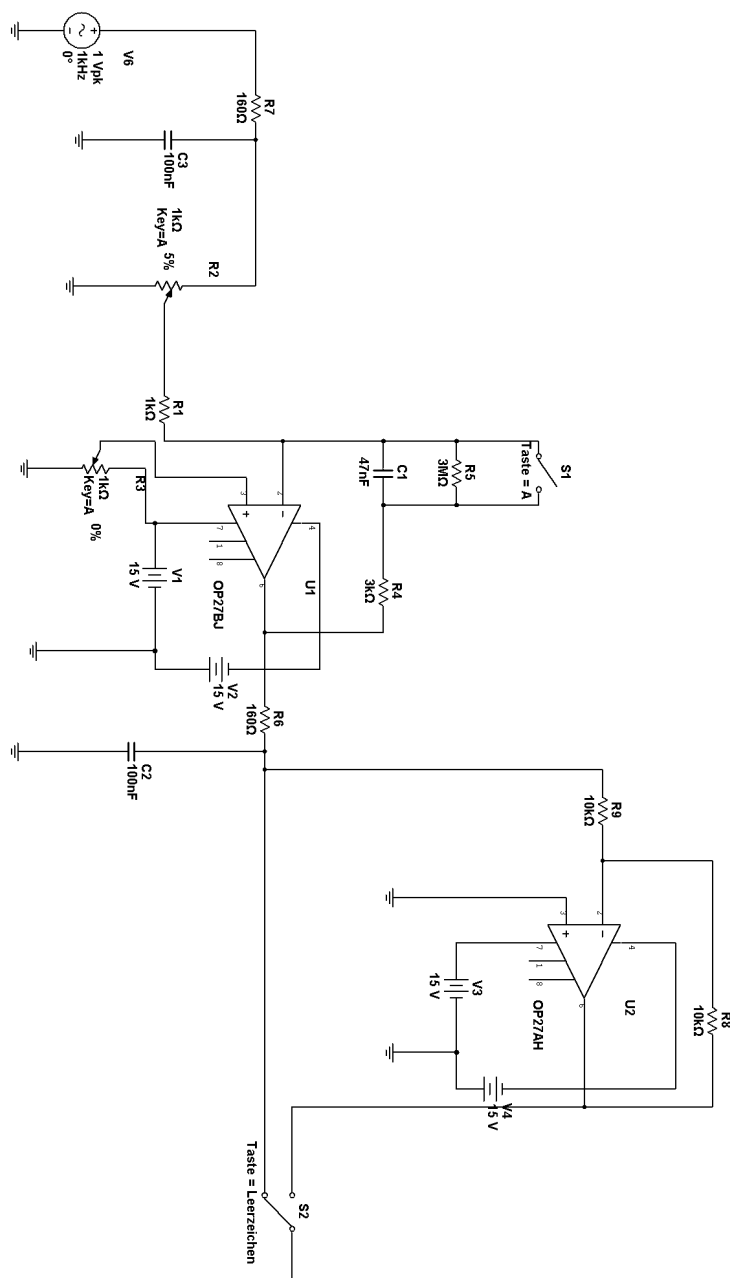
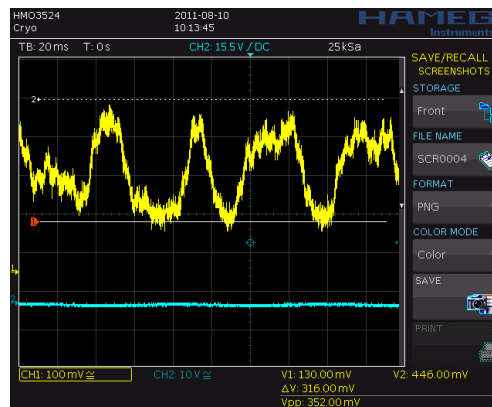


Figure A.1: The stabilization circuit diagram

## A.2 Characterization of the stabilization circuit

The stabilization circuit is implemented to reduce the slow drifts of the interferometer. In figure A.2 is the photo diode signal without the stabilization circuit, and in figure A.3 we see the signal with stabilization turned on.



**Figure A.2: Photo diode signal without stabilization** - Signal of the photo diode observed with an oscilloscope. Stabilization is turned off.  $\Delta V_{pp} = 316 \text{ mV}$

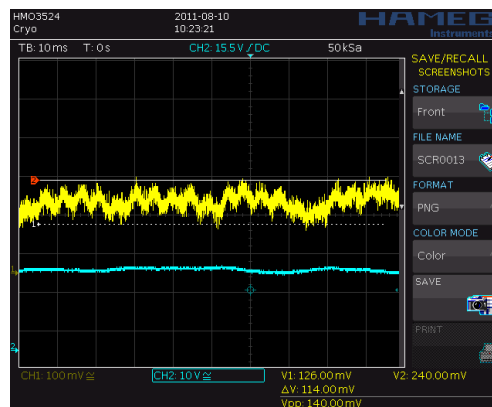


**Figure A.3: Photo diode signal with stabilization** - Signal of the photo diode observed with an oscilloscope. Stabilization is turned on.  $\Delta V_{pp} = 114 \text{ mV}$

The effect of the stabilization circuit is hard to quantify. It is obvious that the minimization of drifts in the signal improves the overall results. In the final resonance spectra the background is minimized, but a quantifiable change in the precision of the resonance frequency is hard to recognize.

### A.3 Characterization of the dynamic behavior of an amplifier

For the characterization of the dynamic behavior of the piezo amplifier<sup>1</sup> we tuned the input frequency at a constant amplitude of  $0.1 V_{pp}$  and recorded the output with an oscilloscope. Then we plotted the output amplitude versus the respective frequency and used an exponential fit to determine the amplification rate  $\gamma_{amp}$

$$f(x) = Ae^{-\gamma_{amp} \cdot t} \quad (\text{A.1})$$

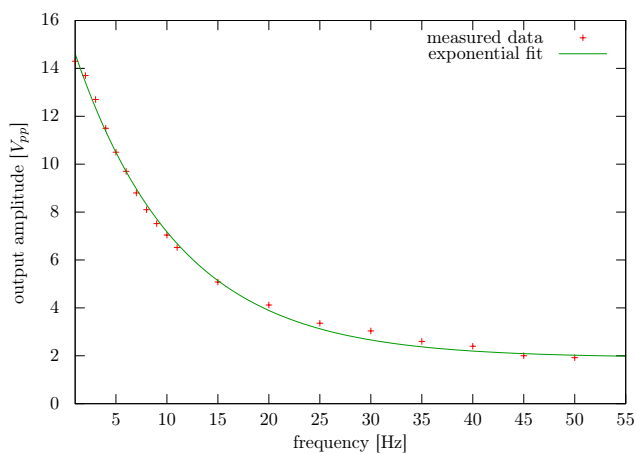


**Figure A.4: Amplification of the piezo amplifier** - The relation between frequency and amplification is determined via an exponential fit. The resulting amplification rate is  $\gamma_{amp} \approx 0.1$  .

<sup>1</sup><http://www.piezomechanik.com>

## References

- [Anetsberger 2009] G. Anetsberger, O. Arcizet, Q. P. Unterreithmeier, R. Riviere, A. Schliesser, E. M. Weig, J. P. Kotthaus and T. J. Kippenberg. *Near-field cavity optomechanics with nanomechanical oscillators*. Nat Phys, vol. 5, no. 12, pages 909–914, December 2009. (Cited on page 2.)
- [Bose 1999] S. Bose, K. Jacobs and P. L. Knight. *Scheme to probe the decoherence of a macroscopic object*. Phys. Rev. A, vol. 59, pages 3204–3210, May 1999. (Cited on page 1.)
- [Brown 2010] K. R. Brown, C. Ospelkaus, Y. Colombe, A. C. Wilson, D. Leibfried and D. J. Wineland. *Coupled quantized mechanical oscillators*, November 2010. (Cited on pages 3 and 33.)
- [Cohen-Tannoudji 2007] Claude Cohen-Tannoudji, Bernard Diu and Franck Laloë. *Quantenmechanik (quantum mechanics), volume 1*. Walter de Gruyter, Berlin, New York, 3 édition, 2007. (Cited on page 29.)
- [Craighead 2000] H. G. Craighead. *Nanoelectromechanical Systems*. Science, vol. 290, no. 5496, pages 1532–1535, November 2000. (Cited on page 2.)
- [Dehmelt 1967] H.G. Dehmelt. *Radiofrequency spectroscopy of stored ions I: Storage*. Adv. At. Mol. Phys., vol. 3, page 53, 1967. (Cited on page 11.)
- [Dehmelt 1968] H. G. Dehmelt and F. L. Walls. *"Bolometric" Technique for the rf Spectroscopy of Stored Ions*. Phys. Rev. Lett., vol. 21, pages 127–131, Jul 1968. (Cited on page 11.)
- [Dobosz 1998] Marek Dobosz, Takashi Usuda and Tomizo Kurosawa. *Methods for the calibration of vibration pick-ups by laser interferometry: I. Theoretical analysis*. Measurement Science and Technology, vol. 9, no. 2, page 232, 1998. (Cited on page 30.)
- [Genes 2008] C. Genes, D. Vitali and P. Tombesi. *Emergence of atom-light-mirror entanglement inside an optical cavity*. Phys. Rev. A, vol. 77, page 050307, May 2008. (Cited on page 1.)
- [Ghosh 1995] Pradip K. Ghosh. *Ion traps*. Clarendon Press, Oxford, 1995. (Cited on pages 14, 15 and 16.)
- [Gulde 2001] S. Gulde, D. Rotter, P. Barton, F. Schmidt-Kaler, R. Blatt and W. Hogervorst. *Simple and efficient photo-ionization loading of ions for precision ion-trapping experiments*. Applied Physics B: Lasers and Optics, vol. 73, pages 861–863, 2001. 10.1007/s003400100749. (Cited on pages 7 and 42.)
- [Hammerer 2009] K. Hammerer, M. Wallquist, C. Genes, M. Ludwig, F. Marquardt, P. Treutlein, P. Zoller, J. Ye and H. J. Kimble. *Strong Coupling of a Mechanical Oscillator and a Single Atom*. Phys. Rev. Lett., vol. 103, page 063005, Aug 2009. (Cited on pages 2 and 33.)
- [Hammerer 2010] K. Hammerer, K. Stannigel, C. Genes, P. Zoller, P. Treutlein, S. Camerer, D. Hunger and T. W. Hänsch. *Optical lattices with micromechanical mirrors*. Phys. Rev. A, vol. 82, page 021803, Aug 2010. (Cited on page 2.)

## REFERENCES

---

- [Hunger 2010] David Hunger, Stephan Camerer, Theodor W. Hänsch, Daniel König, Jörg P. Kotthaus, Jakob Reichel and Philipp Treutlein. *Resonant Coupling of a Bose-Einstein Condensate to a Micromechanical Oscillator*. Phys. Rev. Lett., vol. 104, page 143002, Apr 2010. (Cited on page 2.)
- [Hunger 2011] David Hunger, Stephan Camerer, Maria Korppi, Andreas Jockel, Theodor W. Hansch and Philipp Treutlein. *Coupling ultracold atoms to mechanical oscillators*, 2011. (Cited on page 2.)
- [Häffner 2008] H. Häffner, C.F. Roos and R. Blatt. *Quantum computing with trapped ions*. Physics Reports, vol. 469, no. 4, pages 155 – 203, 2008. (Cited on page 2.)
- [Hänsch 1975] T. W. Hänsch and A. L. Schawlow. *Cooling of gases with laser radiation*. Opt. Commun., vol. 13, page 68, 1975. (Cited on page 17.)
- [Ian 2008] H. Ian, Z. R. Gong, Yu-xi Liu, C. P. Sun and Franco Nori. *Cavity optomechanical coupling assisted by an atomic gas*. Phys. Rev. A, vol. 78, page 013824, Jul 2008. (Cited on page 1.)
- [Kippenberg 2008] T. J. Kippenberg and K. J. Vahala. *Cavity Optomechanics: Back-Action at the Mesoscale*. Science, vol. 321, no. 5893, pages 1172–1176, August 2008. (Cited on page 2.)
- [Law 1994] C. K. Law. *Effective Hamiltonian for the radiation in a cavity with a moving mirror and a time-varying dielectric medium*. Phys. Rev. A, vol. 49, pages 433–437, Jan 1994. (Cited on page 1.)
- [Law 1995] C. K. Law. *Interaction between a moving mirror and radiation pressure: A Hamiltonian formulation*. Phys. Rev. A, vol. 51, pages 2537–2541, Mar 1995. (Cited on page 1.)
- [Leibfried 2003] D. Leibfried, R. Blatt, C. Monroe and D. Wineland. *Quantum dynamics of single trapped ions*. Rev. Mod. Phys., vol. 75, pages 281–324, Mar 2003. (Cited on pages 2 and 20.)
- [Lett 1989] P. D. Lett, W. D. Phillips, S. L. Rolston, C. E. Tanner, R. N. Watts and C. I. Westbrook. *Optical molasses*. J. Opt. Soc. Am. B, vol. 6, no. 11, pages 2084–2107, Nov 1989. (Cited on page 18.)
- [Macalpine 1959] W. W. Macalpine and R. O. Schildknecht. *Coaxial Resonators with Helical Inner Conductor*. Proceedings of the IRE, vol. 47, pages 2099–2105, 1959. (Cited on page 42.)
- [Marquardt 2009] Florian Marquardt and Steven M. Girvin. *Optomechanics*. Physics, vol. 2, page 40, May 2009. (Cited on page 2.)
- [Meiser 2006] D. Meiser and P. Meystre. *Coupled dynamics of atoms and radiation-pressure-driven interferometers*. Phys. Rev. A, vol. 73, page 033417, Mar 2006. (Cited on page 1.)
- [Pain 2005] H.J. Pain. The physics of vibrations and waves. John Wiley & Sons, Ltd, sixth edition édition, 2005. (Cited on page 25.)
- [Paul 1953] W. Paul and H. Steinwedel. *Ein neues Massenspektrometer Ohne Magnetfeld*. Zeitschrift für Naturforschung, vol. A 8(7), pages 448–450, 1953. (Cited on page 11.)

## REFERENCES

---

- [Paul 1990] Wolfgang Paul. *Electromagnetic traps for charged and neutral particles*. Rev. Mod. Phys., vol. 62, pages 531–540, Jul 1990. (Cited on page 11.)
- [Poschinger 2010a] U. Poschinger, A. Walther, K. Singer and F. Schmidt-Kaler. *Observing the Phase Space Trajectory of an Entangled Matter Wave Packet*. Phys. Rev. Lett., vol. 105, page 263602, Dec 2010. (Cited on page 2.)
- [Poschinger 2010b] Ulrich Poschinger. *Quantum Optics Experiments in a Microstructured Ion Trap*. PhD thesis, Universität Ulm, 2010. (Cited on pages 2, 43, 74 and 75.)
- [Regal 2011] C A Regal and K W Lehnert. *From cavity electromechanics to cavity optomechanics*. Journal of Physics: Conference Series, vol. 264, no. 1, page 012025, 2011. (Cited on page 2.)
- [Rivière 2011] R. Rivière, S. Deléglise, S. Weis, E. Gavartin, O. Arcizet, A. Schliesser and T. J. Kippenberg. *Optomechanical sideband cooling of a micromechanical oscillator close to the quantum ground state*. Phys. Rev. A, vol. 83, page 063835, Jun 2011. (Cited on page 2.)
- [Singer 2010] K. Singer, U. G. Poschinger, M. Murphy, P. A. Ivanov, F. Ziesel, T. Calarco and F. Schmidt-Kaler. *Colloquium: Trapped ions as quantum bits: Essential numerical tools*. Review of Modern Physics, vol. 82, page 2609, 2010. (Cited on pages 52 and 56.)
- [Teufel 2011a] J. D. Teufel, T. Donner, Dale Li, J. W. Harlow, M. S. Allman, K. Cicak, A. J. Sirois, J. D. Whittaker, K. W. Lehnert and R. W. Simmonds. *Sideband cooling of micromechanical motion to the quantum ground state*. Nature, vol. 475, no. 7356, pages 359–363, July 2011. (Cited on page 2.)
- [Teufel 2011b] J. D. Teufel, Dale Li, M. S. Allman, K. Cicak, A. J. Sirois, J. D. Whittaker and R. W. Simmonds. *Circuit cavity electromechanics in the strong-coupling regime*. Nature, vol. 471, no. 7337, pages 204–208, March 2011. (Cited on page 2.)
- [Tian 2004] L. Tian and P. Zoller. *Coupled Ion-Nanomechanical Systems*. Phys. Rev. Lett., vol. 93, page 266403, Dec 2004. (Cited on page 31.)
- [Treutlein 2007] Philipp Treutlein, David Hunger, Stephan Camerer, Theodor W. Hänsch and Jakob Reichel. *Bose-Einstein Condensate Coupled to a Nanomechanical Resonator on an Atom Chip*. Phys. Rev. Lett., vol. 99, page 140403, Oct 2007. (Cited on page 2.)
- [Turchette 2000] Q. A. Turchette, Kielpinski, B. E. King, D. Leibfried, D. M. Meekhof, C. J. Myatt, M. A. Rowe, C. A. Sackett, C. S. Wood, W. M. Itano, C. Monroe and D. J. Wineland. *Heating of trapped ions from the quantum ground state*. Phys. Rev. A, vol. 61, page 063418, May 2000. (Cited on page 35.)
- [Vuletić 2000] Vladan Vuletić and Steven Chu. *Laser Cooling of Atoms, Ions, or Molecules by Coherent Scattering*. Phys. Rev. Lett., vol. 84, pages 3787–3790, Apr 2000. (Cited on page 17.)
- [Wallquist 2010] M. Wallquist, K. Hammerer, P. Zoller, C. Genes, M. Ludwig, F. Marquardt, P. Treutlein, J. Ye and H. J. Kimble. *Single-atom cavity QED and optomechanics*. Phys. Rev. A, vol. 81, page 023816, Feb 2010. (Cited on page 2.)

## REFERENCES

---

- [Wineland 1978] D. J. Wineland, R. E. Drullinger and F. L. Walls. *Radiation-Pressure Cooling of Bound Resonant Absorbers*. Phys. Rev. Lett., vol. 40, pages 1639–1642, Jun 1978. (Cited on page [17](#).)
- [Wineland 1979] D. J. Wineland and Wayne M. Itano. *Laser cooling of atoms*. Phys. Rev. A, vol. 20, pages 1521–1540, Oct 1979. (Cited on pages [17](#) and [21](#).)
- [Wineland 1997] D. J. Wineland, C. Monroe, W. M. Itano, D. Leibfried, B. E. King and D. M. Meekhof. *Experimental issues in coherent quantum-state manipulation of trapped atomic ions*, October 1997. (Cited on page [16](#).)
- [Ziesel 2008] Frank Ziesel. *Spektroskopie und transport von ionen in einer mikrofalle*. Master’s thesis, Universität Ulm, 2008. (Cited on page [43](#).)

## Declaration

I herewith declare that I have produced this paper without the prohibited assistance of third parties and without making use of aids other than those specified; notions taken over directly or indirectly from other sources have been identified as such. This paper has not previously been presented in identical or similar form to any other German or foreign examination board.

The thesis work was conducted from 26. October 2010 to 26. October 2011 under the supervision of Prof. Dr. Ferdinand Schmidt-Kaler at Johannes Gutenberg-Universität Mainz.

Tim Lindner